Fluid transport by aggregations of small swimming organisms

Thesis by

Mónica Paola Martínez Ortíz

In Partial Fulfillment of the Requirements

for the Degree of

Doctor of Philosophy

Caltech

California Institute of Technology

Pasadena, California

2016

(Defended November 13, 2015)

To my parents, who never let me skip a day of school and from whom I learned that nothing comes without extraordinary effort.

To my husband Jakob, who understands more fluid dynamics than he ever wished for and who, from now on, will have to call me doctor every morning. I love you.

...and to those who I admire and will never read this.

Acknowledgements

My most sincere gratitude goes to my advisor Prof. John Dabiri. I cannot imagine my life at Caltech without his guidance, encouragement, kindness, and sense of humor. I am grateful for his support throughout these years, and for providing me with the necessary tools to be successful hereafter. I will always remember all the personal and academic advice he provided me with and I hope he continues to be an academic big brother to me.

I would also like to thank Prof. Andrew Thompson for always keeping an open door. His enthusiasm and readiness to discuss many aspects of my research have been key to the completion of this work. His passion for ocean dynamics has been truly contagious and I thank him for his time and patience. I am very grateful to Prof. Melany Hunt for her support and advice throughout my graduate studies. I thank her for believing in me and always being there for me. I feel very honored to have had Prof. Tim Colonius in my graduate committee. I have always admired his work, ever since I was an undergraduate student, and will always appreciate his encouragement and, most of all, his honest opinion and suggestions. I am deeply thankful to Prof. Roberto Zenit, who was my undergraduate advisor and also served in my graduate committee. He was the one who introduced me to the exciting world of fluid dynamics and has always incited me to go beyond what I think are my limits.

I would also like to acknowledge Prof. Mory Gharib, Prof. Beverly McKeon, and Prof. Tony Leonard for their insightful suggestions, and interest in my research. I am profoundly thankful to my post-doctoral advisors, Prof. Jess Adkins and Dr. Dimitris Menemelis, for allowing me to complete this work and at the same start doing research in their group. I am deeply indebted to several members of the sci-

entific community, who have enriched my scientific abilities and from whom I have learned so much: Prof. Heidi Fuchs, Prof. Mimi Koehl, Prof. Roman Stocker, Prof. Alex Leshanksy, Prof. Manooch Koochesfahani, Prof. Eckart Meiburg, and Prof. Dana Dabiri.

I consider myself very lucky to have been part of an interdisciplinary research group. I thank all the past and present members of the Dabiri lab for their help, advice, and all the good times we had together: Janna Nawroth, Matthias Kinzel, Robert Whitlessey, Ian Brownstein, Kristy Schlueter, and Nicole Xu. I specially thank Clara O′Farrell as well as Daniel Araya and his lovely wife Carolina Restrepo, with whom I shared most of the ups-and-downs. I also want to thank my sweet summer student Samantha Collins, who has never ceased to amaze me. I look forward to finding out what her future beholds. I profoundly thank the Collins family for being a family away from home. I really cherish all the time we have spent together.

I am blessed to end this stage of my life and take an amazing group of friends with me. I thank Esperanza Linares for her love and unconditional support, but above all, for reminding me that I should not take myself too seriously. I am deeply grateful to Chengyun Chua for always cheering me up despite the weekends and long nights I made her work through codes and equations. I would also like to thank Namiko Saito for being my partner in crime and showing me a life outside Caltech.

Caltech is truly an unusual place. It is an academically stimulating environment where I have come to meet and interact with wonderful and incredibly smart people. I thank each and every one of them for making this an unforgettable and gratifying experience.

I would also like to thank Federico Hernandez and Ernesto Mancilla for their friendship and support over the years. I feel forever indebted with them for always being a skype call away regardless of the time zone. I am also very grateful to Ines Familiar and Alan Vidali for their incredible friendship. My life in the

States would not have been the same without your home-cooked meals and the reminder that work is not everything.

I consider myself extremely fortunate to have been able to pursue my dreams. It would not be possible to be where I am at without my family, who have supported and inspired me throughout the years. When I was little I hated pre-school and my mom bargained a deal with me: I could skip that year, but if I tried something remotely similar ever again I would be selling gum in the street for a living. I enjoyed Dumbo for a year and I have been hitting the books ever since. I grew up to believe I could be anything I wanted as long as I worked hard, and that would not have been possible without the love and support of my parents, who have always pushed me outside of my comfort zone. *Mamá y papá: gracias por su amor y apoyo todos estos años. Este logro no hubiera sido possible sin ustedes. Paco y Gaby gracias por siempre hacerme reir y venir a visitarme tan seguido, los extraño.* I would also like to thank my extended family. Michael, Ute, and Jonas Wilhelmus: *Ich bin sehr dankbar für eure Liebe und Ünterstützung.*

Finally, I would like to thank my husband Jakob Wilhelmus for travelling the world so that I can do what I love to do. He has been holding my back these past five years and I will be eternally grateful for his love, support, and understanding. *Gracias por ser mi mejor amigo y mi alma gemela. Gracias por enseñarme lo bello de la vida, no lo hubiera logrado sin ti. Este título y todo lo que viene es por ti.*

This work was supported by the US-Israel Binational Science Foundation, the Office of Naval Research, and the National Science Foundation.

Abstract

Diel vertical migration of zooplankton has been proposed to affect global ocean circulation to a degree comparable to physical phenomena. Almost a decade after shipboard measurements showed high kinetic energy dissipation rates in the vicinity of migrating krill swarms, the hypothesis that biogenic mixing is relevant to ocean dynamics and local fluid transport has remained controversial due to the inability to directly measure the efficiency of this biological process. In situ field measurements of individual swimming jellyfish have demonstrated large-scale fluid transport via Darwinian drift, but it has remained an open question of how this transport mechanism is manifested in smaller species of vertically-migrating zooplankton that are sufficient in number to be accountable in the dynamics. The goals of the present study are, first, to devise and implement experimental instruments and develop methodologies to investigate this biological process in a laboratory setting and, second, to determine whether efficient fluid transport mechanisms become available during vertical collective motion and, if so, analyze how energy is distributed within the flow. By leveraging the phototactic abilities of zooplankton, a multi-laser guidance system was developed to achieve controllable vertical migrations of *A. salina* concurrently with laser velocimetry of the surrounding flow. Measurements show that the hydrodynamic interactions between neighboring swimmers during vertical migration result in the development of a pronounced jet opposite to animal motion. In non-stratified fluid, this hydrodynamic feature is shown to trigger a Kelvin-Helmholtz instability that results in the generation of eddy-like structures with characteristic length scales much larger than the individual size of the organisms. Experiments in a thermally stratified water column also display the presence of a downward jet despite the strong stable stratification. Furthermore, overturning regions larger than the size of an individual organism are observed adjacent to the migrating aggregation, suggest-

ing an alternate energy transfer route from the small scale of individual swimmers to significantly larger scales, at which mixing can be efficient via a Rayleigh-Taylor instability. The computed velocity spectrum is consistent with these findings and displays energy input at scales larger than the body length of a single swimmer. The mixing efficiency, inferred from the spectral energy distribution with and without stratification, matches experimentally achieved mixing efficiencies via a Rayleigh-Taylor instability within a stable stratification. According to our findings, biogenic mixing does have the potential to redistribute temperature, salinity, and nutrients effectively. We propose the employment of laser control to examine additional species as well as alternative oceanic environments and interrogate its effect on the efficiency of biogenic mixing.

Contents

List of Figures

List of Tables

Chapter 1

Introduction

1.1 Dissertation Overview

The context in which biogenic mixing was initially proposed as a potential source for vertical ocean mixing is discussed in the following section. In addition to its global impact, much interest exists in gauging the local impact that vertical migrations of zooplankton aggregations have on nutrient and carbon transport across the water column. There has been extensive research on these topics, and the aim of the first half of Chapter 1 is to delineate the framework of research in biogenic mixing, followed by an overview of the state of the art in biogenic mixing studies and the scope and aim of the current research effort. Chapter 2 introduces the test organism and the developed experimental techniques used to study diel vertical migrations (DVM) in the laboratory. The experimental apparatus and laboratory procedures were tailored to induce and control animal motion via phototaxis —a directional response to changes in light properties. Chapter 3 focuses on characterizing animal-fluid interactions during vertical collective motion. Velocimetry data in a non-stratified fluid is presented and the energy distribution during vertical migration is discussed and compared to flow visualizations in a larger domain. These results are followed by similar experiments in stratified flow conditions and further analysis of the expected efficiencies in Chapter 4. In an effort to bypass the inherent difficulty of including the near-field flow of swimming organisms in numerical models, a hybrid numerical-experimental model was developed to study fluid transport by vertical migrations of simulated animal aggregations. Chapter 5 provides insight into the design principle and results from the numerical

experiments. This dissertation is concluded in Chapter 6, which includes a final discussion on the results of the previous chapters and recommendations for future investigations in this field.

1.2 Background

1.2.1 Missing Mixing Problem

The distribution of heat around the Earth occurs through the circulation of the ocean and the atmosphere. In the ocean, this process is governed by a wide range of fluid motions, spanning from meters to thousands of kilometers [98]. The complexity of capturing these multi-scale interactions marks the main challenge of climate modeling and has been the focus of research studies for over a century. Taking this into account, the main focus of this introductory section is to describe important aspects of the dynamics that occur on a global average.

The most distinctive feature of the ocean is its stable density stratification, which impedes vertical transport of nutrients and fluid properties across isopycnals, i.e., surfaces of constant density. The vertical density profile divides the water column into three main horizontal regions: the upper mixed layer, the pycnocline and the deep ocean. Each of these zones has very distinct dynamical and biochemical properties and their vertical extent depends on diurnal as well as seasonal and latitudinal variations. On average, however, the mixed layer spans the region immediately below the ocean surface up to a depth of 100 m or less [93]. This region is characterized for being fairly well mixed, although small temperature variations are still detectable. The region spanned by the pycnocline is often referred to as the thermocline, given that density variations in the ocean are mostly due to temperature changes and it typically extends to a depth ranging from 500 to 1000 m below the surface [93]. The steep density gradient within this zone is what impedes the exchange of nutrients and properties between the mixed layer and the ocean interior. The deep ocean is the zone below the pycnocline and comprehends most of the oceanic water mass. In this region, density and temperature continue to decrease gradually with depth.

On a global scale, the stability of the density gradient along with the global ocean circulation dictates nutrient, carbon, and energy transport in the ocean. The global overturning circulation, also known as the Meridional Overturning Circulation (MOC), connects the ocean basins and transfers heat throughout the ocean. On a global average, the MOC transports warm water from tropical to polar regions, where convective processes lead to a decrease in the potential energy of the ocean by converting these warm water masses into colder, denser fluid that sinks deeper into the ocean. In order to complete the MOC, energy is needed to subsequently raise the potential energy of the system against the stable density stratification [59], [60].

Early studies have demonstrated that ocean circulation is in fact not convectively-driven, but rather sources for vertical mixing are essential to close the loop [106]. As illustrated by Ferrari [22], one can view the ocean as a water body with progressively changing properties, namely, with cold dense water masses at the bottom followed by subsequently warmer fluid layers with decreased density on top. Thus, exchange of fluid properties across the layers is only possible through overturns, which occur when internal waves break. In this scenario, internal waves can be thought of as energy-containing oscillations of those layers that produce mixing across them once kinetic energy is transformed into potential energy, thereby raising the center of mass of the ocean.

Initially, winds and tides were identified as the primary drivers for vertical transport in the ocean, providing kinetic energy collectively at a rate of approximately 2 TW [59]. As described above, this influx of energy becomes available throughout the water column as a result of intermittent internal wave generation and breaking. An evident mismatch between vertical diffusivities deduced from field measurements and theoretical estimates of the values needed to account for the rate at which fluid sinks at the poles triggered a search for the sources of *missing mixing* in the oceanographic community [49], [59].

Field measurements recently showed that currents impinging on bottom topography release energy at a rate sufficient to close the mean ocean energy budget ($\sim$ 0.5 TW) [65]. However, the resulting vertical mixing is not uniformly distributed across the ocean depth due to the limit imposed by the density stratification on the vertical extent to which mixing is confined. As a consequence, bottom ocean mixing due to the roughness of ocean topography transports fluid up to mid-depth [22]. It is hypothesized that fluid is then transported to the Southern Ocean, where wind-driven processes allow further transport to the surface along outcropping isopycnals. This new ocean mixing scheme is currently being tested against in situ measurements, which have already shown a great variability in mixing efficiencies depending on the roughness and flow characteristics within a given location [74], [22].

Further research efforts have been made to better understand the return pathways of deep-ocean fluid properties to the surface. Some of these efforts, for example, have focused on processes occurring at the Southern Ocean, where large-scale motions driving vertical fluid transport have been identified. Additionally, the contribution of energetic turbulent features at the sub-mesoscale (horizontal span of $\leq$ 10 km) is being investigated [38].

So far, the results from recent investigations challenge the existence of a single additional source of missing mixing. One thing is certain, however, that vertical mixing is an intermittent process exhibiting a complex global distribution. Spatially mapping the intensity of vertical mixing and identifying the corresponding energy source will be the next milestone towards solving the *missing mixing* problem [22].

1.2.2 Local Ocean Nutrient Distribution

Global nutrient distribution in the ocean is intimately related to physical and biogeochemical processes. Locally, nutrients are unevenly distributed throughout the water column primarily due to the negative buoyancy of most particulate or-

ganic matter and remineralization by bacteria at depth [15]. In the near surface region, the concentration of nutrients is limited by biological consumption if the appropriate ratio of macromolecules such as carbon, nitrogen, and phosphorous is available [58]. On the other hand, light absorption limits biological activity at increasing depths, leading to an increase in nutrient concentration. In the oxygen-depleted regions of the deep ocean, bacteria transform inorganic matter into absorbable macromolecules, further increasing the concentration of essential elements at depth. Nutrient replenishment near the ocean surface occurs via terrestrial runoff and via transport from nutrient-rich regions at depth resulting from vertical mixing as well as upwelling [54].

The non-negligible effect of anthropogenic processes on nutrient availability in the ocean imposes continuously varying bounds on primary production. Much focus has been given on assessing the impact of ocean acidification on oceanic environments due to the rapid increase of carbon dioxide emissions to the atmosphere [58]. The role of swimming organisms in altering the biogeochemistry budget of local ecosystems is an emerging interest of the scientific community given its potential relationship to climate variability and ocean ecology [17]. DVM of zooplankton aggregations—introduced in the following section—are hypothesized to play an important part in both local and global ocean processes described above [31].

1.2.3 Diel Vertical Migrations of Zooplankton Aggregations

Many zooplankton species, such as krill and copepods for example, have been observed to aggregate in dense groups within the water column [60]. Mostly idle at depth, swarms migrate vertically towards shallower regions during the night and return to deeper regions during the day. The fraction of the marine zooplankton biomass that engages in these recurrent biological processes known as diel vertical migrations (DVM) has not been precisely determined. However, an upper and lower bound of 90% and 15% of total zooplankton biomass, respectively, have been proposed in the literature as the fraction of migratory marine zooplankton

species [105], [32], [17].

The reasons behind DVM are not well understood, and neither are the specific triggers for vertical motion [79]. From an ecological perspective, the energy expenditure of translating hundreds of meters across the water column must be justified by long-term benefits for the aggregation. The most evident explanation behind DVM is its use as a response against visual predation by larger organisms. Observations of the behavior of *Daphnia* (Cladocera; Crustacea) in Lake Maarsseveen, The Netherlands support this view [24]. It was found that DVM followed a seasonal pattern according to the development of the thermocline—the region of maximum temperature changes with depth—in the lake. The segregation of aquatic regions due to temperature variations across the lake resulted in nutrient depletion at the surface as well as abundance of larger fish in upper regions, which preferred higher temperatures. Under these conditions, DVM of *Daphnia* was reported in contrast to the periods of time when no evident density stratification was imposed by temperature variations in the lake.

In the ocean, DVM have been observed to occur most commonly within the upper 600 m [7], although observations have also registered events in deeper ocean regions ($\sim$ 1500 m below the surface) [45], [99]. Echosounder acoustic measurements show a correlation between the cues of sunrise and sunset and the migratory pattern by marine species [79]. However, no consensus has been reached over what triggers DVM in the ocean given that this factor alone does not explain migration patterns of pelagic species that remain within unilluminated regions of the ocean [99]. It has been suggested that in the upper ocean regions, different factors such as light properties, temperature, pressure, nutrient availability, and chemical signals from predators have a certain degree of influence in the observed patterns [79], [78]. In fact, recent numerical studies show a strong correlation between the depth reached during DVM and oxygen concentration in the water column [7]. In the case of pelagic organisms, laboratory experiments with zooplankton species suggest the development of circadian rhythms [20].

Zooplankton species that undergo DVM in upper ocean regions present a directional response to changes in light properties known as phototaxis [11]. This behavioral trait was the basis of the design process in this investigation to implement an apparatus and develop procedures that allow the study of the fluid dynamics of DVM in the laboratory. As will be explained in Chapter 2, it was found that *A. salina* (a species of brine shrimp) has maximum positive phototaxis in the blue-green range of the light spectrum (450-570 nm) and a neutral response towards red (620-750 nm). In nature, the distribution of light at the surface of a clear water body changes throughout the day and night. At midday, for example, all wavelengths are uniformly distributed, whereas at night transmission of intermediate wavelengths (550-650 nm) is at a minimum [57]. Furthermore, light absorption in a clear water body results in the suppression of longer wavelengths with depth [83]. Therefore, close to the ocean surface, DVM is likely to be triggered by a sudden change in light intensity, which occurs during sunrise and sunset, within regions that correspond to the blue-green range of the light spectrum.

It has been hypothesized that DVM can have a substantial impact on fluid and nutrient transport in the ocean [52], [9]. However, the resulting local and global effects of these collective motions have not been quantified. Specifically, it remains an open question whether DVM induce fluid transport mechanisms relevant to the physical and biogeochemical structure of the ocean. By swimming over large vertical distances, small organisms have the potential to impact naturally occurring nutrient and density gradients within their natural environment, and thereby enhance biological production.

Estimates based on net primary production in the ocean indicate that marine organisms have a reservoir of chemical energy supplied by phytoplankton near the surface at a rate of approximately 60 TW [17]. Swimming organisms that undergo DVM thus have enough power to be relevant in large-scale mixing processes. The question, however, is whether there exists an efficient hydrodynamic conversion to mechanical energy that contributes to raise the potential energy of the ocean.

Identifying the underlying fluid transport mechanisms during DVM of zooplankton aggregations is crucial to assessing the role of swimming animals in fluid dynamic processes in the ocean. The next section (§1.3) introduces the currently known fluid transport mechanisms by swimming organisms: turbulent wake mixing and induced fluid drift.

1.3 Biogenic Mixing Mechanisms

An extensive registry of DVM patterns around the globe has been obtained from sonar readings at various depths [7]. However, the inability of determining zooplankton taxa as well as the resulting flow kinematics using acoustic data has imposed a major challenge in estimating the impact of swimming organisms in biogeochemical and physical processes in the ocean. Currently, two main transport mechanisms have been demonstrated in situ: transport in the turbulent wake of migrating aggregations and the so-called Darwinian drift. These are illustrated in this section, along with proposed estimates of global efficiencies of biogenic mixing.

1.3.1 Turbulent Wake Mixing

In this mixing process, unsteady swimming by individual organisms sets fluid into motion by generating eddy-like structures at scales comparable to the organism appendages. This energy is expected to cascade to smaller scales until it is dissipated as heat by viscosity. During this direct energy cascade, fluid properties and nutrients can be transported on length scales commensurate with the size of the formed eddies.

Field measurements aiming to quantify biogenic mixing with respect to background ocean levels, showed elevated rates of turbulent kinetic energy (TKE) dissipation in the vicinity of a DVM of a densely-packed krill aggregation in Saanich Inlet, British Columbia [42]. Within a span of 10 to 15 minutes, TKE dissipation

rates increased by 3 to 4 orders of magnitude compared to background ocean turbulence, reaching values of 10^{-5} to 10^{-4} W kg^{-1}. Furthermore, unstable density overturns in the range of 1 to 10 m were reported during the DVM time-lapse, suggesting enhanced vertical mixing on the same level as winds and tides. These measurements agreed with theoretical estimates for the dissipation due to turbulent wake transport [31],[17]. However, a subsequent analysis noted that high TKE dissipation rates do not necessarily imply enhanced fluid mixing, and in order to estimate the contribution of DVM in global mixing processes, a quantitative link between the observed microscale dissipation rates and the energy distributed within the largest overturning structures in the flow needs to be provided [43]. Thus, an important metric to determine the impact of biogenic mixing is its efficiency, rather than the rate at which energy is dissipated.

As illustrated in §1.2.1, one can visualize a water column under stable density stratification as having denser water layers at the bottom with progressively lighter layers on top. Therefore, the center of mass of a stratified water body is lower than that of a non-stratified one, and vertical mixing resulting in the irreversible exchange of fluid properties between such layers will act to raise the potential energy of the system. The mixing efficiency of a biogenic process is commonly estimated via the flux Richardson number R_f, which is defined as the ratio of the amount of energy that contributes to change the potential energy of the water column via vertical mixing to the total amount of kinetic energy expended by a given mixing process, e.g., turbulent mixing by swimming organisms [36]:

$$R_f = \frac{\mid \Delta PE \mid}{\mid \Delta KE \mid} \quad , \tag{1.1}$$

where Δ refers to the change in energy between the initial and final state of the mixing process. The general expression in Equation 1.1 can be related to a ratio of length scales in order to determine the scales at which biomixing processes must introduce energy into the flow in order to achieve efficient mixing [100]. This is done by applying Richardson's four-thirds law to relate R_f to an eddy diffusivity coefficient K, where:

$$K \approx \varepsilon^{1/3} L^{4/3} \quad , \tag{1.2}$$

and

$$K = \underbrace{\frac{Rf}{(1-R_f)}}_{\Gamma} \frac{\varepsilon}{N^2} \quad , \tag{1.3}$$

where ε is the turbulent kinetic energy dissipation rate, L is the integral length scale and N is the Brunt-Väisälä buoyancy frequency, which is a measure of the stability of the stratification, defined as [69], [93]:

$$N = \sqrt{-\frac{g}{\rho}\frac{d\rho}{dz}} \quad . \tag{1.4}$$

By combining Equations 1.2 and 1.3, the mixing coefficient Γ may be expressed as:

$$\Gamma = \frac{R_f}{1-R_f} \approx L^{4/3} \left(\frac{N^2}{\varepsilon^{2/3}} \right) \quad , \tag{1.5}$$

where the last factor can be rewritten in terms of the Ozmidov buoyancy length scale, which characterizes the length scale over which density changes in the ocean [100]:

$$l_B = \sqrt{\frac{\varepsilon}{N^3}} \quad . \tag{1.6}$$

This leads to the four-thirds scaling of the mixing efficiency factor as

$$\begin{aligned} \Gamma &\approx \left(\frac{L}{l_B} \right)^{4/3} \qquad L < l_B \\ \Gamma &\approx \gamma_0 \qquad\qquad L \geq l_B \ , \end{aligned} \tag{1.7}$$

where γ_0 is the maximum value of the mixing coefficient. In oceanographic flows, γ_0 is often observed to be constant and reach a limit of 0.2 [100],[69],[68]. Recent experimental work has shown that although this value is observed for induced turbulence due to shear instabilities developing in stratified flows, enhanced mixing ($R_f = 0.75$ and $\gamma_0 = 3$) can result from Rayleigh-Taylor instabilities developing between regions of stable density stratification [48].

Here, it is important to highlight that the quantity that provides a measure of the mixing efficiency of a given physical process is given by the flux Richardson

number R_f, which by definition is constrained to the range $0 - 1$. The mixing coefficient Γ provides a means to relate the amount of energy used to raise the potential energy of the water column to a commonly measured quantity, the kinetic energy dissipated by fluid viscosity. In the literature, these two are often used interchangeably, mainly because for shear instability between stratified layers the critical value of R_f has been found to be between 0.15 - 0.2, which results in $\Gamma \approx 0.2$. However, for other instabilities such as Rayleigh-Taylor, these two vary and, in principle, Γ can attain values greater than unity [68],[87].

A consequence of Equation 1.7 is that the size of fluid structures generated by the motion of migrating organisms must approach the Ozmidov length scale in order for biogenic mixing to be efficient. In the ocean, the buoyancy frequency is typically within the range of 10^{-2} to 10^{-4} s^{-1} [106]. Therefore, if ε spans from 10^{-5} to 10^{-4} W kg^{-1}, as has been previously reported, the associated Ozmidov length scale ranges from 3 to 10,000 m. An early theoretical analysis, based on the assumption that fluid motions during DVM scale according to the size of the organisms within the aggregation, resulted in a low estimate of mixing efficiency. Thus, the biogenic contribution to ocean mixing was deemed negligible [100]. However, it was later found that an additional fluid transport mechanism is available during animal locomotion: Darwinian drift [37]. As illustrated below, large-scale fluid transport via drift could lead to higher mixing efficiencies during DVM.

1.3.2 Darwinian Drift

As outlined above, relevance of DVM as an agent for vertical mixing in the ocean comes down to the ability of vertically migrating aggregations to generate energetic large-scale fluid structures, with respect to the buoyancy length scale imposed by the stable density stratification. In situ field measurements of individual swimming jellyfish demonstrated the so-called Darwinian drift mechanism that enables organisms to transport fluid on length scales much larger than the appendage size, and thereby achieve efficient mixing [37] (Figure 1.1).

Figure 1.1: In situ observation of fluid transport via Darwinian drift. Flow visualizations with fluorescent dye demonstrated large-scale fluid transport in the wake of a swimming jellyfish (*Mastigias* sp.). This image is reproduced with permission from Katija and Dabiri [37].

This mechanism has its origins in studies of fluid transport in potential flow [14]. In this idealized case, the pressure field around a rigid object translating through non-viscous fluid sets the surrounding fluid into motion and allows it to propagate along with the object (see Figure 1.2). Considering a body translating across a material surface in an unbounded fluid, Darwin calculated the total volume of fluid being drifted to be proportional to the volume of the object itself through its added mass coefficient. In situ observations of fluid transport via drift by swimming organisms suggested an alternative path to efficient mixing without the requirement of generating rotation in the flow. Furthermore, it implied that the efficiency depends on organism shape rather than size.

Subsequent analysis in real fluid showed that the volume of fluid carried by an object via induced drift mechanism is enhanced by viscosity [37], [18]. This suggests that organisms swimming at low Reynolds number may transport fluid on scales larger than their characteristic body size and perhaps even greater than the Ozmidov scale, which would lead to efficient mixing. This excludes the Stokes

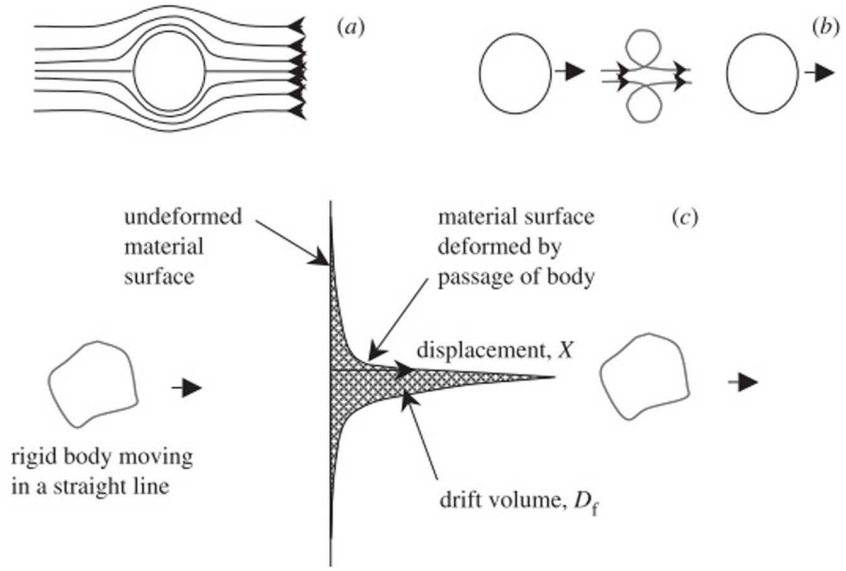

Figure 1.2: Illustration of the Darwinian drift mechanism in ideal fluid. Drawings (a) and (b) indicate fluid particle trajectories in the reference frames of the object and the fluid, respectively. The sketch shown in (c) illustrates the resulting drift volume behind an object translating in a straight line across a material surface. This image is reproduced with permission from Eames [18].

flow limit, i.e., large scale fluid transport may occur provided the organisms are sufficiently large to swim relative to the local flow [101].

Due to the intrinsic difficulty of experimentally investigating the flow generated by swimming organisms [108], [104], the concept of drift has been further studied via numerical and analytical modeling of the far-field flow due to individual swimming organisms. Initially, the first effort to estimate the relevance of the drift mechanism in global ocean processes modeled the flow due to a self-propelled organism as that of a steadily towed sphere via CFD [37]. However, further analysis, using fundamental solutions to the Stokes equations, clarified that the far-field flow generated by an active swimmer differs from that of a passively towed body [50],[86].

As illustrated in Figure 1.3, the former results in a momentumless wake due to the opposed effects of thrust and drag, whereas the latter is characterized by a momentum defect in the wake due to the unbalanced effect of drag on the body. This distinction has important consequences regarding fluid transport in that the volume of fluid being drifted along with the swimmer is finite and comparable

to the volume of the swimmer itself, indicating that the contribution of biogenic mixing is negligible to global ocean dynamics.

The apparent contradiction between the estimated fluid transport due to the far-field of an active swimmer and in situ observations of fluid transport by a swimming jellyfish suggests that in order to precisely estimate the drift volume generated by a real swimmer, both the near- and far-field flows need to be considered in the analysis. Furthermore, it has been hypothesized that the unsteady nature of real swimmers may also contribute to large scale fluid transport, an attribute that is not taken into account in models based on solutions to the Stokes equations [36].

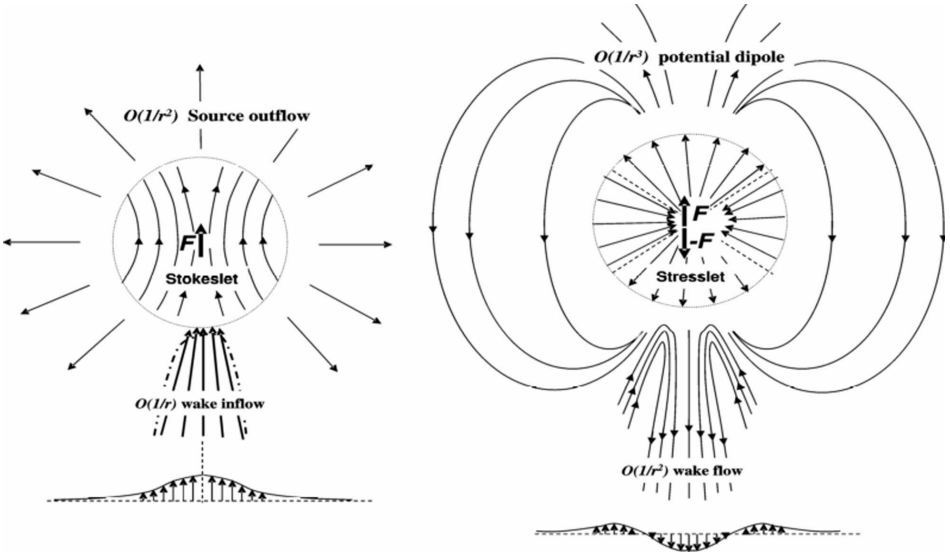

Figure 1.3: Far-field flows of passively towed objects and self-propelled swimmers in Stokes flow. The main difference between a passively towed object (left) and a self-propelled swimmer (right) is the net momentum flux at the wake. The outgoing radial force resulting from steadily translating an object through fluid is balanced by an inflow at the wake (left). In contrast, a steady self-propelled swimmer generates no net momentum flux at the wake due to the counter-balance of thrust and drag across any given cross-section within the wake. This image is reproduced with permission from Subramanian [86].

As a means to bypass the difficulty of exactly capturing the near- and far-field hydrodynamic signatures of swimming organisms numerically, recent efforts have implemented experimental velocimetry data of individual swimmers into numerical models of animal migration (see Chapter 5 and the simultaneously but independently developed tool by [35]). This approach takes full swimming cycles of

the measured velocity field due to an individual swimmer as building blocks to artificially simulate fluid transport due to vertical animal migration. Numerical experiments using jellyfish with and without oral arms indicated the non-negligible effect of animal morphology on the drift volume and its effect on the near-field flow of the swimming organism [35]. Use of this experimental-numerical tool emerges as an inexpensive numerical alternative to address the effects of animal morphology, unsteady propulsion, and swimming mode on fluid transport by individual swimming organisms.

1.3.3 Implications of Collective Animal Motion

The numerical studies mentioned in Section 1.3.2 have focused on estimating fluid transport induced by individual swimmers. It remains an open question of how turbulent wake transport and induced drift are affected by the presence of multiple swimming organisms migrating in close proximity, as occurs during DVM. It is possible that additional mixing mechanisms become relevant during vertical collective motion, as in bioconvection [29],[39].

The first study to integrate the effect of hydrodynamic interactions between multiple swimmers during DVM on studies of biogenic fluid transport, simulated vertical migrations of self-propelled swimmers by using potential flow solutions of translating rigid spheres resulting in a momentum-less wake [12]. This simplified model suggests that vertical transport in a stably stratified fluid depends on the arrangement of the swimmers within the group. Thus, even in the presence of restoring effects by buoyancy, the amount of fluid being drifted by an aggregation of self-propelled swimmers is larger than that of an individual organism. Other factors such as the organism swimming mode and the number density of animals within the aggregations are anticipated to affect fluid transport as well.

Further efforts have been made to obtain field measurements that encompass in situ animal behavior as well as ambient ocean conditions. However, direct shipboard measurements rely on the fortuitous presence of migrating zooplankton, and

such observations have proven difficult to repeat ([80], and see response by Rippeth *et al.* to [42]). Laboratory experiments are a potential alternative method to analyze biogenic mixing in controlled environments. In fact, experimental investigations involving aggregations of small swimmers have been reported in the past, but these efforts have been aimed at analyzing vital functions, such as swarming and feeding (see [24] ,[26] for example), rather than transport and mixing.

The present investigation constitutes one of the first attempts to quantify animal-fluid interactions during DVM in the laboratory within the context of biogenic mixing. Throughout the course of this investigation, a similar study was independently done by Lorke *et al.* ([66],[67]). The successful implementation of particle tracking, along with particle image velocimetry (PIV) and planar laser-induced fluorescence (PLIF) measurement techniques allowed tracking of the trajectory of individual swimmers, while simultaneously acquiring velocity data and concentration changes of fluorescent dye within a two-dimensional plane in the central region of a water tank. Yet, the difficulty of controlling animal motion in the laboratory setup challenged the study of collective motion as occurs during DVM. As a result, hydrodynamic effects due to collective motion were not observed and the estimated mixing efficiencies were low, yielding negligible estimated contributions of biogenic mixing to vertical ocean mixing.

1.3.4 Notes on Current Efficiency Estimates

At the most fundamental level, mixing can be understood as the progression of two main processes: dispersion and diffusion [93]. The former, also referred to as stirring, strains the fluid by driving initially neighboring fluid particles apart. This results in enhanced concentration gradients that are reduced and irreversibly eliminated by molecular diffusion. The lack of a general theory of mixing has resulted in application-specific measures to estimate the efficiency of any given process. In the case of biogenic mixing, this ambiguity has generated an ongoing discussion regarding the suitable assumptions to estimate the efficiency of a biogenic mixing process that incorporates the action of property advection as well as diffusion.

As discussed in Section 1.3.2, the in situ demonstration of large scale fluid transport via drift with respect to the Ozmidov buoyancy length scale suggests the non-negligible contribution of swimming organisms to vertical ocean mixing. This result was extrapolated to estimate the total mixing power produced via drift, based on momentum conservation alone [37]. The resulting estimate indicates that the contribution of biogenic mixing via drift to vertical ocean mixing is of the same order of magnitude as that of physical ocean drivers, such as winds and tides. Subsequent studies have questioned the validity of this approach, which relies on the assumption that the concentration gradients imposed by the achieved large scale fluid transport are ultimately diffused at small scales via molecular diffusion.

The first study on biogenic mixing to include the effect of molecular diffusion in the analysis, claimed that processes at the molecular level inhibit large scale fluid transport via drift during DVM [41]. By estimating the effective diffusivity due to biogenic mixing from a scaling analysis of momentum conservation as well as of the balance of advection-diffusion for a conserved property, it was shown that diffusion short-circuits large scale transport. However, the model was based on the assumption that vertical collective motion during DVM results in fluid structures comparable to the size of the individual swimmers within an aggregation. Thus, as expected, the resulting vertical diffusivity was much lower than previous estimates [41]. Furthermore, recent experimental studies support the notion that estimates of mixing efficiency need to include molecular diffusive properties of scalars in the analysis explicitly, rather than inferring the efficiency solely based on a momentum analysis of the flow field. The argument is that momentum-derived quantities only account for the first stage of mixing, i.e., dispersion, leaving out processes at the molecular level. However, it is not evident that the low values of mixing efficiency obtained using this mixing parameterization approach are fully attributable to the inclusion of molecular diffusivity, given that vertical collective motion appeared to be ineffective during the experiments [67].

Another point of contention was raised by the possibility that the fluid being

drifted during vertical migration would eventually restratify before irreversible mixing is achieved via molecular diffusion [36]. The inability to gather large data sets on the field has challenged direct evaluation of this scenario. However, recent numerical analysis of towed bodies in Stokes and potential flow (a lower and upper bound of fluid transport via drift, respectively) hint at the possibility that additional mixing mechanisms, that act to homogenize scalar gradients resulting from large-scale transport via drift, are necessary for irreversible mixing to occur [35].

These issues motivate future research efforts to study fluid transport and mixing due to vertical collective motion of small swimming organisms. It is hypothesized that the near-field flow interactions between neighboring swimmers within an aggregation will result in an increase in the amount of fluid being drifted, ultimately enhancing vertical fluid mixing. Moreover, additional parameters related to the environment in which DVM occur, such as the non-quiescent nature of background fluid motions in the ocean, must be included in the analysis in order to correctly evaluate the contribution of swimming organisms to vertical ocean mixing.

1.4 Research Objectives

The main goal of this investigation is to develop new experimental and analytical tools to study biogenic transport and induced mixing by the vertical collective motion of small swimming organisms. Extrapolation of field observations of Darwinian drift acting at the scale of individual swimmers to estimate the effect of neighboring organisms during collective motion is not evident, and direct evaluation of the flow during DVM is needed to appraise the contribution of this process to vertical ocean mixing. For this purpose, the first objective of this investigation is to develop an experimental system, laboratory protocols, and measurement techniques for achieving DVM on-demand in a controlled laboratory setup. The apparatus and laboratory methodologies are to be designed according to a common behavioral trait among zooplankton species that undergo DVM, known as

phototaxis. The aim is thus to trigger unidirectional group migration by leveraging this behavioral response to a specific range of wavelengths of light. The successful implementation of this technique will not only facilitate the present investigation, but will also provide a tool to explore the effect of different fluid regimes on biogenic mixing by DVM in future studies, such as background turbulence or double diffusion.

The scope of this investigation is to quantify the energetics of the flow during DVM in increasingly complex scenarios, from non-stratified to stratified media, to analyze fluid transport during DVM and to estimate the efficiency of the induced mixing. The former scenario of fluid transport in non-stratified fluid is addressed in an effort to identify the fundamental fluid transport mechanisms that occur during biogenic mixing due to DVM. The objective is to identify the fluid transport processes that emerge from collective vertical migrations of small zooplankton species and to determine the length scales at which the mechanical energy is input to the fluid during DVM. This activity will elucidate whether collective motion of small swimmers in fact results in larger scale fluid structures, a notion that has been demonstrated to be intimately related to biogenic mixing efficiency [100].

Further investigation of this biological process in stratified fluid is necessary to address the effect of buoyancy on vertical fluid advection. Theoretical studies of small swimming organisms in stratified flows within the low Reynolds number limit ($Re << 1$) have illustrated the suppression of vertical fluid transport by density stratification [4]. However, experimental studies analyzing the wake of individual organisms have demonstrated that even in the presence of a strong stable stratification, non-negligible vertical fluid transport is still achieved [104]. To study the effect of buoyancy on fluid transport and mixing due to DVM, additional laboratory procedures are to be designed and implemented, such that linear density stratification in the test tank is achieved. Given that the density stratification in the ocean is mostly due to temperature variations except in high latitude regions, a reasonable approach is to impose a linear temperature gradient while maintaining the salinity concentration constant. Comparison of the resulting energy

distribution in this case with that occurring under no stratification will allow the evaluation of the mixing efficiency due to DVM.

Finally, the last objective of this investigation is to evaluate the effect of additional parameters that are inherently difficult to isolate in experimental studies via a numerical analysis. Given the disagreement of numerical studies neglecting the near-field flow of swimming organisms with experimental observations, the approach is to form virtual aggregations from experimental velocimetry data of a single swimmer. In this sense, the effect of animal configuration within an aggregation on fluid transport, for example, can be directly evaluated. Recent independent efforts by Katija ([35]) analyze fluid drift under a similar approach. The extent of her analysis agrees with the premise of this investigation that use of this numero-experimental tool provides new means to analyze fluid transport during vertical migration in a non-expensive manner.

Chapter 2

Experimental Methods

2.1 Introduction

The key element to consider in order to induce collective animal motion in a laboratory setting is how organisms react to specific stimuli underwater. In the wild, various zooplankton species acquire information regarding changes of light and relate it to their vertical position with respect to the ocean surface. This cue is thought to trigger animal migration to regions tagged with a specific wavelength whenever a dramatic change in intensity occurs, i.e., at sunrise and sunset ([57]). As described in this chapter, an experimental setup was designed and implemented that stimulates this reaction—known as phototaxis—and induces vertical collective motion by using light sources that match this criteria. In §2.2, a description of the model organism and the behavioral tests done to characterize ranges of maximum response are presented. The experimental apparatus is illustrated in §2.3, and the laboratory methodologies used to perform the experiments are outlined in §2.4.

2.2 Test Organism

Artemia salina (Linnaeus, 1758) was used as a model organism for the experiments described in Chapters 2, 3, and 4. It should be noted that this arthropod, which is a species of brine shrimp, is commonly found in coastal and inland water bodies, such as salt lakes and lagoons, and although observations of these creatures have been reported in open sea, they are not prone to survive in oceanic

environments ([47], [21]). Nonetheless, use of this crustacean facilitates studies of collective motion of oceanic species in controlled laboratory environments, given its behavioral response to light and remarkable resilience.

As illustrated in Figure 2.1, the dormant cyst of *A. salina* hatches into a nauplius larva and grows to juvenile and adult stages reaching up to 15 mm in length. This cycle includes a series of 15 stages separated by molting periods in which the exoskeleton is replaced. The biggest transition, however, occurs between the larval and post-larval instars given the drastic variation in morphology as well as swimming and feeding mechanisms. At the initial developmental stages, organisms use their antennae for propulsion and feeding, whereas juveniles and adults employ their developed limbs, also known as thoracopods. *A. salina* feeds via non-selective filtering of particles through its thoracopods, with exception of the first larval stage ([97], [1]). Two-week old juveniles (Mariculture Tech. Intl.) with body length of approximately 5 mm were used in all experiments (bottom left part of the diagram on Figure 2.2). At this stage, organisms have developed 11 pairs of legs and swim by beating their appendages in a metachronal wave.

Similar to various species of small marine organisms, *A. salina* has evolved a directional response to light as a defense mechanism against predators ([26]). This behavioral reaction is known as phototaxis and, as explained in Chapter 1, it is one of the cues for diel vertical migrations of zooplankton in the ocean. By sensing gradients in light color and intensity, small organisms are able to migrate to greater depths during the day to avoid visual predation by larger fish, and return to shallower waters at night to graze ([24]). A description of the characterization of this photobehavior in *A. salina* is presented below.

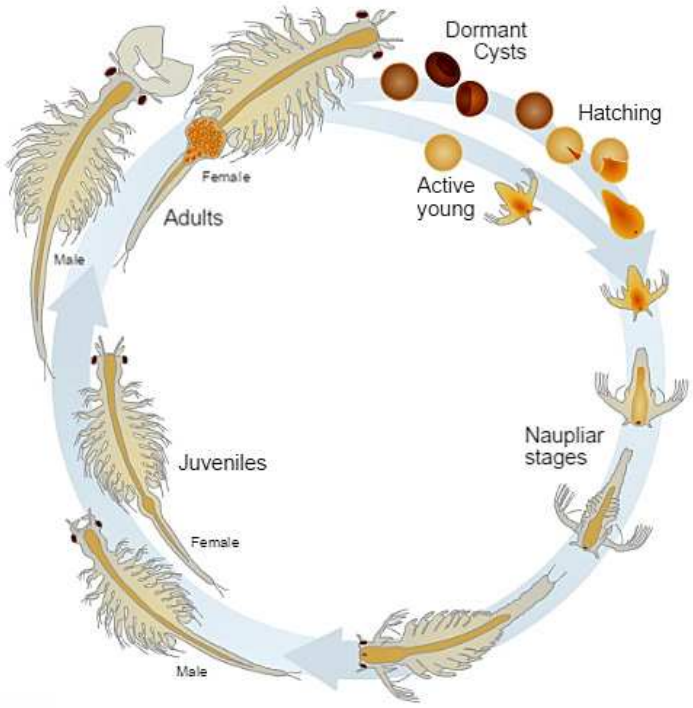

Figure 2.1: Life cycle of *A. salina*. Embryos are deposited inside cysts, where they can survive for many years during adverse environmental conditions. If temperature, salinity, and oxygen levels are favorable, the embryo starts developing and hatching occurs. Nauplii consist of a single eye, an undeveloped trunk, and a set of antennae, which they use for propulsion and feeding. Juveniles and adults have two compound eyes, a digestive tract, sensorial antennae and 11 pairs of functional limbs. This image was taken from [97].

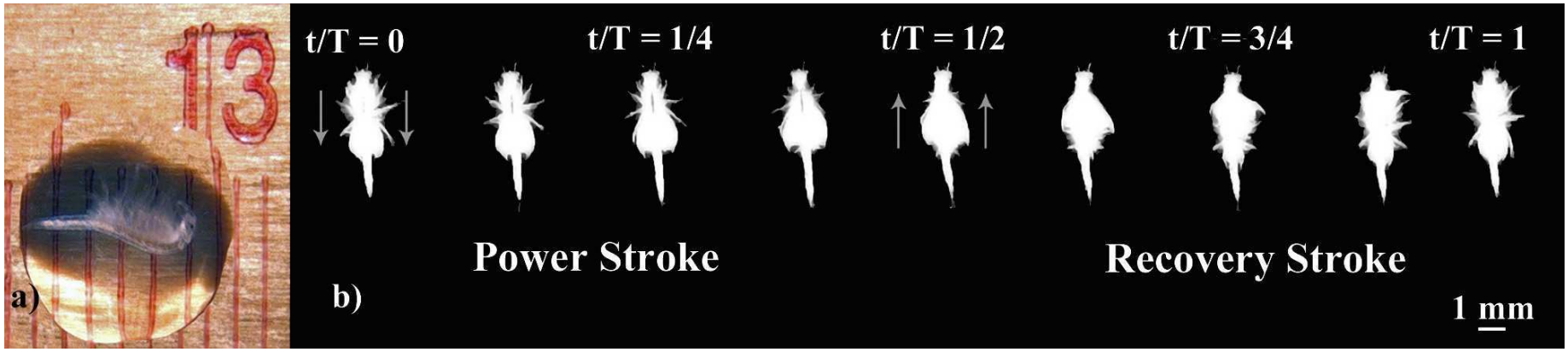

Figure 2.2: Snapshots of a two-week old juvenile *A. salina*. (a) The organism was seized using a pipette and positioned on top of a ruler (SI units) by releasing a droplet of the sampled water. (b) Time series showing the power and the recovery strokes that form the metachronal wave of a two-week old *A. salina*. The complete cycle ranges from $t/T = 0$ to $t/T = 1$, where time t is measured from the beginning of the swimming cycle and T is duration of the swimming cycle. The direction of appendage motion is indicated by the gray arrows at the beginning of each stroke.

2.2.1 Assessment of Phototactic Response

Following methods in the literature [70], the phototactic behavior of *A. salina* was evaluated by systematically testing different wavelengths of light to identify ranges of maximum positive response. For this purpose, decapsulated eggs (Cabrillo Marine Aquarium, San Pedro, CA) were hatched in the laboratory and raised to 48 hours old.

The photobehavioral tests were performed using a 7520 beam lm spotlight (Source Four 405-1). A series of gel filters mounted in front of the spotlight was used to span the visible light spectrum. The nauplii were observed to be positively phototactic to the blue-green portion of the color spectrum and neutral in their response to red. Furthermore, by comparing the nauplii distribution with respect to the light source position, it was observed that the strongest positive attraction occurred for wavelengths ranging from 420 nm to 500 nm. Past these maxima in directional behavior, the phototactic response was found to decrease along the green region up to the red portion of the visible light spectrum, where animals were found to be impartial to the stimulus. Further tests with lab-grown juveniles and adults showed that the strength of the directional response decreased as animals aged, but remained constant within the duration of each life cycle stage (one to three weeks for juveniles). Nonetheless, the range of wavelengths for which attraction occurred remained constant throughout the life cycle.

With the exception of the aforementioned tests, experiments were done using industrially harvested organisms (Mariculture Tech Intl). Constant phototactic response was ensured by performing the experiments within 48 hours of animal delivery.

2.3 Experimental Setup

Based on the results of §2.2.1, an experimental apparatus was developed to (1) induce and control the collective vertical motion of *A. salina* in the laboratory, and (2) quantify the generated flow field via a two-dimensional velocimetry technique. Experiments were performed in increasingly complex scenarios from non-stratifed to stably stratified environments, for which additional systems were incorporated in the apparatus. The core of the experimental setup is presented in §2.3.1, which is essential to achieve point (1) in a non-stratified fluid, whereas §2.3.2 details the additional systems to study this process under a stable density stratification.

2.3.1 Laser-guidance System

As shown in Figure 2.3, the experimental setup consists of a 1.2 m H $\times$ 0.53 m W $\times$ 0.53 m L acrylic tank and a newly developed three-laser guidance system that artificially stimulates animal migration while allowing for two-dimensional velocimetry measurements. The dimensions of the container were sufficiently large to avoid wall effects.

Collective animal motion was triggered and controlled by means of luminescent signals from a 2 W, 447 nm (blue) laser and a 1 W, 532 nm (green) laser. The blue laser beam functioned as a cue for vertical migration to the aggregation, given that its intensity and wavelength matched the range of maximum positive phototaxis. This laser was mounted on a custom vertical traverse (Parker Hannifin) that controlled the position and vertical speed of the beam via a software interface (ACR-View 6).

The introduction of a second light stimulus was needed to position the migrating aggregation within the central region of the tank as well as constrain animal motion within a two-dimensional plane, thus allowing two-dimensional PIV measurements. As the blue laser beam penetrated one of the side walls of the tank, the reflection of the light on the plexiglass produced a bright spot on the surface,

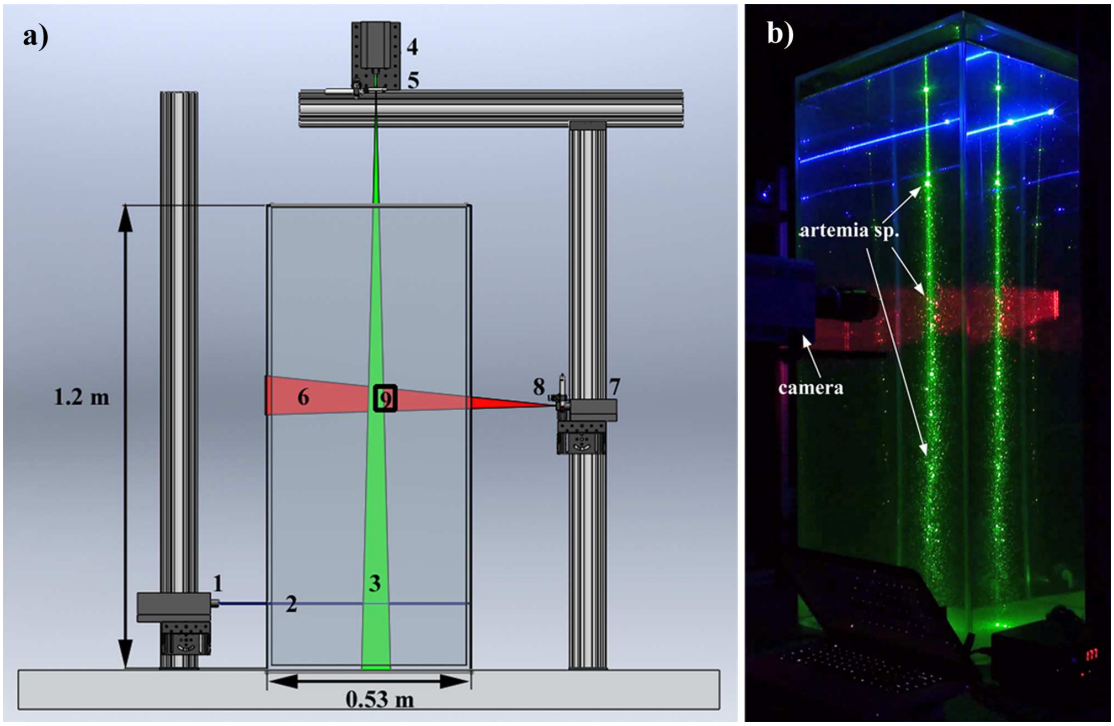

Figure 2.3: Laser guidance system for induction and control of vertical migrations of plankton aggregations. (a) The setup consists of a 447 nm laser (1) that generates a horizontal blue laser beam (2), which is aligned with a vertical green laser sheet (3), generated by a 532 nm laser (4) and a -25 mm focal length cylindrical lens (5), and introduced from above the tank. A vertical, red laser sheet (6) is introduced from the side of the tank and is produced using a 635 nm laser (7) and a -3.9 mm focal length cylindrical lens (8). PIV measurements are recorded within the overlap region (9). (b) Photo of the setup during a migration event, after the 447 nm laser has completed its vertical traverse of the tank. The image was captured at an angle, producing duplicate reflections of the lasers in the two visible sides of the tank.

which resulted in animal aggregation directly by the wall. Thus, even though the blue light stimulus resulted in vertical collective motion by itself, a second signal was needed to center the position of the organisms during vertical migration. The introduction of a vertical green laser sheet from above created a brighter region at the center of the column, resulting from the alignment of the green laser sheet with the blue laser beam. This combination of light signals ensured that the organisms swam vertically in the center of the tank. Moreover, the width of the green laser sheet (i.e., its horizontal span) determined the inter-organism spacing due to the behavioral preference of the organisms to swim within regions illuminated by stimuli triggering positive phototaxis. In this way, the organisms aggregated within the planar section inscribed by the green laser sheet and migrated following

the steady vertical motion of the blue laser beam. Furthermore, minimal sheet divergence resulted in constant animal spacing with height.

The resulting three-dimensional flow was measured within the two-dimensional plane shown in Figure 2.3 via particle image velocimetry (PIV). For this purpose, a horizontal laser sheet was generated by a 1 W, 635 nm (red) laser and aligned with the green laser sheet. The neutral behavior of the organisms toward the red portion of the light spectrum allowed for non-intrusive measurements of the velocity field during animal migration.

2.3.2 Stratification and Temperature Profiling Systems

In the ocean, vertical nutrient transport and mixing are restricted by the presence of a stable density stratification. Therefore, to evaluate the effect of buoyancy on the observed fluid transport due to the vertically migrating aggregation was of interest to this investigation. For this purpose, additional systems were designed and implemented to thermally stratify the water column within the laser-guidance setup described in §2.3, and track the imposed temperature gradient over time.

The thermal stratification system consists of a total of eight electronic titanium water heaters with integrated temperature control (Azoo, 500 W), which are positioned with suction cups in two of the walls of the water tank as shown in Figure 2.4. On the back side of the tank, five heaters are arranged with a distance of 22.86 cm (9 in) in between them and set to progressively decreasing temperatures from top to bottom of the tank (Table 2.1). On the opposite side, only three heaters are placed within matching vertical positions of the back wall array in order not to block the field of view of the camera.

As detailed in §2.4, the developed methodology to set up a stable density stratification involves the continuous tracking of the generated temperature gradient. Inspired by field measurements using optical fiber cable to characterize the density profile of an oceanic cross-section, a temperature profiler was designed and assembled. The instrument consists of an array of ten waterproof digital temperature

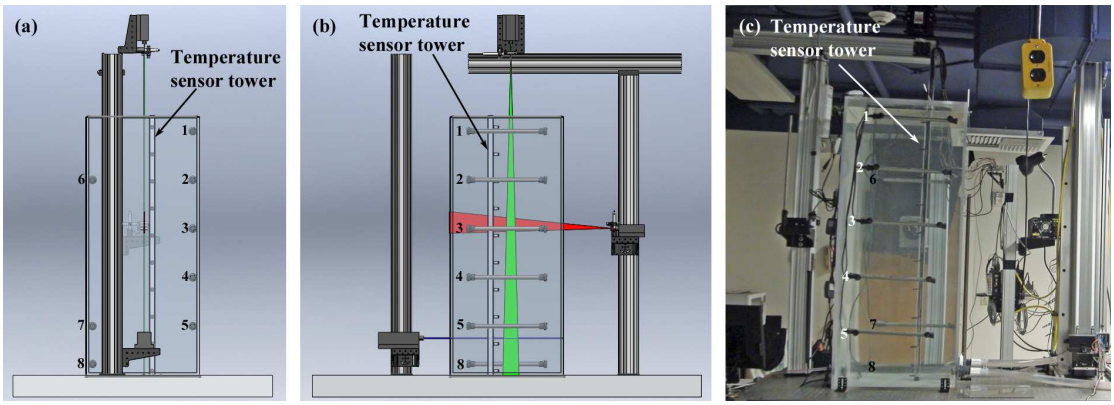

Figure 2.4: Fluid stratification and temperature profiling systems. The thermal stratification system consists of an array of equidistant water heaters set to progressively decreasing temperatures (1-8). The temperature at the center of the water column is continuously tracked via a temperature profiler consisting of 10 temperature sensors vertically spanning the water column. The side (a), front (b), and back (c) views of the integrated setup are shown, where unlabeled components can be identified in Figure 2.3.

probes (Dallas DS18B20) mounted on a rigid plastic rod and a computer interface, thus allowing pointwise temperature measurements every 12.5 mm along the vertical axis. As shown in Figure 2.4, the device was offset by 2.54 cm (1 in) from the center of the tank to avoid overlap with the laser-illuminated regions of the water column.

Heater Number	Temperature (°F)	Temperature (°C)
1	78	25.5
2, 6	76	24.4
3	74	23.3
4	72	22.2
5, 7	70	21.1
8	68	20.0

Table 2.1: Temperature setting of fluid stratification system. An equidistant array of eight heaters was set to progressively decreasing temperatures from top to bottom of the water column as shown in Figure 2.4. The temperature in each heater was set in degrees Fahrenheit as specified.

Temperature Profiler Description

The temperature profiler consists of an array of ten digital thermometers (Dallas DS18B20) installed along one side of a hollow rectangular acrylic rod (2.54 cm

by side), and an open-source electronics platform (Arduino Uno), which is linked to the computer. The benefit of using this customized instrument rather than a vertically translating probe is the ability to acquire measurements across various vertical positions simultaneously without disturbing the flow field.

The device was designed to use the transistor DS18B20 because each sensor has a unique serial number encoded, making it a simple task to identify the data sent from each digital probe in a given array. Each probe comprises a 7 mm in diameter and 26 mm long sealed capsule, containing the transistor, attached to a 1.3 m cable. The sensor has an operational temperature range between -55 °C and 125 °C, with an accuracy of ±0.5°C from -10 °C to 85 °C, and a configurable resolution from 9 to 12 bits with a maximum response time of 750 ms.

The digital address of each sensor was identified prior to assembly and each sensor was positioned accordingly along the plastic shaft, which was drilled on one side to hold each sensor in place. The set of probes were then connected to a single digital signal bus of the microprocessor through a simple electronic circuit. The Arduino board and software, combined with the serial board terminal application CoolTerm, were used as an interface to acquire temperature data from the electronic thermometers at any given time. The wiring diagram used to read the individual sensor addresses and gather data from the temperature sensors is provided in Appendix A.

Validation of Sensor Calibration

The factory calibration of each sensor in the temperature profiler was validated by setting the water column to a constant temperature and comparing the acquired measurements with that of an alcohol thermometer. Two submersible water pumps (Taam Rio) were introduced inside the tank before and during data acquisition to ensure a uniform temperature distribution throughout the water column.

Four verification tests were performed with a total of five temperature measurements, recorded in five minute intervals. As expected, all sensors featured a narrow standard deviation for the range of temperatures tested. Yet, as shown in Figure 2.5, a systematic error exceeding measurement precision in the temperature measurements of two sensors was revealed (sensors 4 and 7, counting from the bottom).

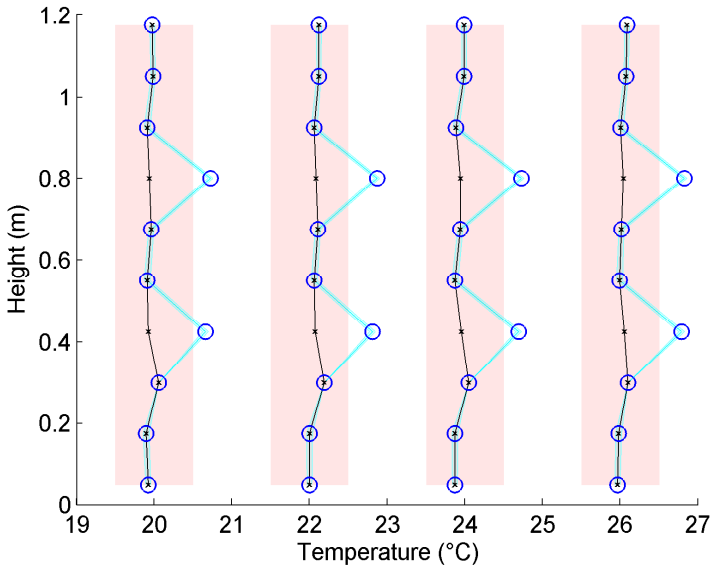

Figure 2.5: Validation Measurements of Temperature Sensor Calibration. Four validation tests with the water column at temperatures 20°C, 22°C, 24°C, and 26°C are presented. The blue circles indicate the mean temperature measurement resulting from 5 acquisitions at that temperature and the light blue shaded region shows the standard deviation. The black dots connected with the black line indicate the corrected temperature values. The red shaded regions mark sensor measurement accuracy.

To correct for this measurement error, a correction constant (α) was calculated for each sensor according to:

$$\begin{aligned} \alpha_4 &= < \bar{T}_4 - T_{th} > \\ \alpha_7 &= < \bar{T}_7 - T_{th} > \ , \end{aligned} \tag{2.1}$$

where α_4 and α_7 are the correction constants for sensors at heights 0.4 m and 0.8 m, respectively, $\bar{T}_4$ and $\bar{T}_7$ correspond to the temporal mean value acquired at a specific temperature for the corresponding sensor, T_{th} corresponds to the temperature reading from the alcohol thermometer and the angle brackets refer

to an ensemble average, i.e., the average over the four tested temperatures. By using the estimated correction constants, the temperature readings lay within the permissible accuracy of the transistor (Figure 2.5). The temperature measurements presented in future chapters were corrected applying this procedure after acquisition:

$$\begin{aligned} Tc_4 &= T_4 - \alpha_4 \\ Tc_7 &= T_7 - \alpha_7 \ , \end{aligned} \tag{2.2}$$

where Tc_4 and Tc_7 indicate the corrected temperature values, and T_4 and T_7 stand for the acquired temperature measurements of sensors 4 and 7.

2.3.3 Implementation of Particle Image Velocimetry Technique

Two-dimensional particle image velocimetry (PIV) was used to obtain instantaneous velocity field measurements during vertical animal migration. Measurements were recorded at 250 fps within the 2.8×2.8 cm^2 field of view at the center of the water tank (Figure 2.3) to ensure sufficient temporal as well as spatial resolution to analyze animal-fluid interactions during vertical migration correctly. This standard velocimetry technique calculates the velocity of the flow from the displacement of particle tracers within an illuminated plane over time and consists of three main components:

- **Particle tracers:** The flow was seeded with 13 μm silver-coated hollow glass spheres (Potters Industries Inc.). Owing to their neutrally buoyant nature in the test fluid, their displacement within the illuminated region of the test tank allowed the measurement of the velocity in a non-intrusive manner.

- **Light source and optics:** A continuous red collimated diode laser (1 W, 635 nm) and a plano-concave cylindrical lens (-3.9 mm focal length) were used to illuminate a plane at the center of the tank. The wavelength of the laser was chosen to match the range of neutral animal behavior.

- **Digital camera:** A high-speed digital camera (Photron Ultima APX-RS) was used to acquire high definition images during animal migration. High spatial resolution measurements were attained by using a telephoto micro-focus lens (Nikkor 105mm f/2.8) and an extension tube (PK-13 27.5mm). The scattered light from the particle tracers was isolated from the laser-guidance system light sources by using a narrow bandpass filter (660 nm CWL, 10 nm bandpass).

2.3.4 Data Preparation Process

Raw PIV images were processed using a commercial code (DaVis 9, LaVision GmbH). The algorithm is based on dividing each image into smaller interrogation areas and cross-correlating each one of these sub-regions, pixel by pixel, over two consecutive frames to estimate the velocity at that position. The correlation of each interrogation area yields a signal peak, which corresponds to the mean particle displacement. Dividing the calculated displacement by the time between frames results in a velocity vector map over the entire image. A time series of velocity field maps is obtained by repeating this process over the entire set of acquired images.

In all experimental sets, the velocity fields were computed by cross-correlating image pairs separated by $\Delta t = 0.06$ s. Image interrogation was conducted by iterating twice with a multi-pass method of decreasing window size from 64×64 to 32×32 with a 50% overlap. This resulted in a 65×64 velocity field with a spatial separation of 0.4 mm between velocity vectors. Post-processing was accomplished by applying a universal outlier detection test at the end of the routine. No filters were applied to mask the shape of the organisms, under the assumption of a no-slip boundary condition at the body.

2.4 Laboratory Procedures

The methodology employed to induce and control animal migration in the water tank is introduced in §2.4.1. This procedure was used independent of the properties of the fluid inside the tank, i.e., regardless of whether its density was constant or linearly stratified. In §2.4.2, the process to thermally stratify the water column is described.

All experiments were conducted in 15 ppt artificial seawater, pre-mixed with PIV tracers. Each batch of half-sized *A. salina* was shipped in a single plastic bag (Mariculture Tech Intl). Prior to each test, the organisms were equally distributed in two aerated glass beakers (2 L total volume) with a low flow rate and water salinity to match the conditions in the test tank. After this acclimatization process, test organisms (6500 ± 4800) were drained from one of the glass beakers and introduced at the top of the tank using a fine mesh fish net. The number of organisms used in a given experimental test was determined by drawing five samples of 25 ml of solution from the beaker and counting the number of organisms within the sample. According to our provider, each batch of half-sized brine shrimp contains $\sim 15,500$ organisms, which would result in ~ 7750 used organisms in each test, which is within the obtained organism range.

2.4.1 Procedures for Experiments in a Non-stratified Fluid

Once the organisms were transferred into the tank with the laboratory lights turned off, the blue laser was positioned at the bottom of the water tank and subsequently activated. The organisms swam downward in phototactic response, gathering around the blue laser beam (Figure 2.6a). Reflection of the incoming blue laser beam at the edge of the water tank resulted in greater animal concentration at the wall. Once the organisms were distributed around the blue laser beam, the green laser was activated, generating a narrow vertical green laser sheet. Simultaneously, the blue laser beam was momentarily deactivated, in order to induce horizontal animal motion towards the green laser sheet in the center

of the tank (i.e., away from the brightest portion of the blue beam at the wall). As the organisms were evenly distributed at the center of the water column, the blue laser beam was reactivated and set to translate upward at 1 cm/s (Figure 2.6b). A microcontroller (Acrobotic Industries) mounted on the vertical traverse and located at the initial position of the blue laser triggered a high-speed camera (Photron Ultima APX-RS), which was oriented perpendicular to the plane to be illuminated by the red laser sheet. The red laser was then turned on to generate a continuous red laser sheet.

Following this scheme, three sets of measurements were obtained by triggering the camera according to three time delays ($\tau_1 = 0$ s, $\tau_2 = 47$ s, and $\tau_3 = 67$ s), corresponding to different stages of the migration. The first delay captured measurements of the flow conditions in the tank prior to vertical migration, as the organisms gathered within the blue beam at the bottom of the container (Figure 2.6a). Once this control data set was gathered, measurements were collected for either the second or third time delay, corresponding to the beginning or middle of the migration, respectively. The beginning and middle of the migration were defined to start when the first organisms in the aggregation reached approximately 1/2 and 3/4 of the height of the tank, respectively (Figures 2.6c & 2.6d). A total of 10 vertical migrations were measured: five recorded for the second delay and five for the third delay, each with a corresponding control measurement at the first time delay.

2.4.2 Procedures for Experiments in a Linearly Stratified Fluid

For this series of experiments, thermal stratification of the water column is set prior to transferring the organisms inside the water tank, mainly due to the long time span of this process. Even though the animals survive inside the tank for over 24 hours, such a drastic reduction in oxygen levels might alter swimming performance.

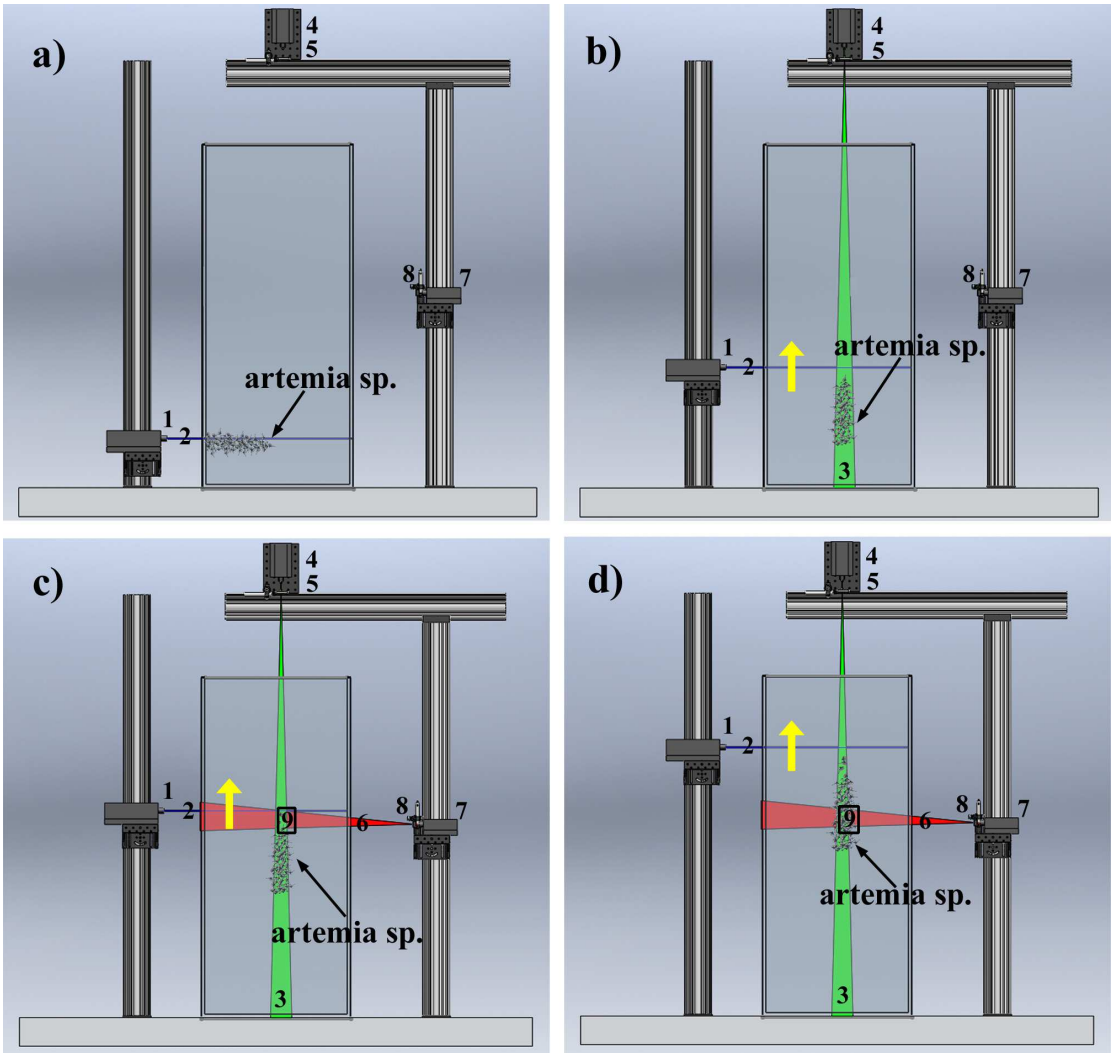

Figure 2.6: Experimental procedure. Prior to triggering vertical motion, measurements were taken with the aggregation distributed around the blue beam at the bottom of the tank (a). Subsequently, vertical motion was triggered by activating the green laser sheet and translating the blue beam upwards (b). Measurements were taken for two different stages in the migration: the stage referred to as the *beginning of the migration* occurred when the first organisms in the aggregation reached 1/2 of the height of the tank (c), whereas the *middle of the migration* was determined to occur when the first migrating organisms reached 3/4 of the height of the tank (d). Labeled components correspond to the ones introduced in Figure 2.3.

Prior to switching on the heaters inside the water tank, the temperature profiler is activated and set to gather temperature measurements every 5 minutes. Fluid properties inside the tank are corroborated to match room temperature and a salinity of 15 ppt by using the temperature profiler and a hydrometer. Each heater is then sequentially activated from top to bottom, as shown in Figures 2.7 and 2.8, according to the temperatures in Table 2.1.

Simultaneous activation of the water heaters, regardless of the temperature setting, generates convection-driven flow inside the tank, resulting in a non-linear temperature gradient. This is avoided by increasing the water temperature slowly from top to bottom. By acquiring temperature measurements continuously across the water column, the temperature gradient can be resolved at any given time. Once the temperature in the top region of the heater that is to be triggered has reached a higher value than the lower region, the element is activated. Momentary deactivation of each unit is automatically set off by the automatic temperature control within each heating device.

The serial process described above lasts an average of 6 hours. Once the stratification is within the permissible range, which is determined by the accuracy of the temperature sensors of ± 0.5 °C, the animals are introduced into the tank and the experiments are performed according to the procedures described in Section 2.3.1. All heating units are switched off after the animals have gathered at the bottom of the column around the blue laser beam and before starting the experiment.

Similarly to the non-stratified experimental set, measurements were obtained by triggering the camera to a given time delay. In this case, measurements were collected for the first and third time delay ($\tau_1 = 0$ s and $\tau_3 = 67$ s). This corresponds to the stages at which the organisms have gathered within the blue beam at the bottom of the container, and when the first organisms to migrate have reached approximately 3/4 of the height of the water column, respectively. A total of two vertical migrations were measured, each with its corresponding control measurement at the first time delay.

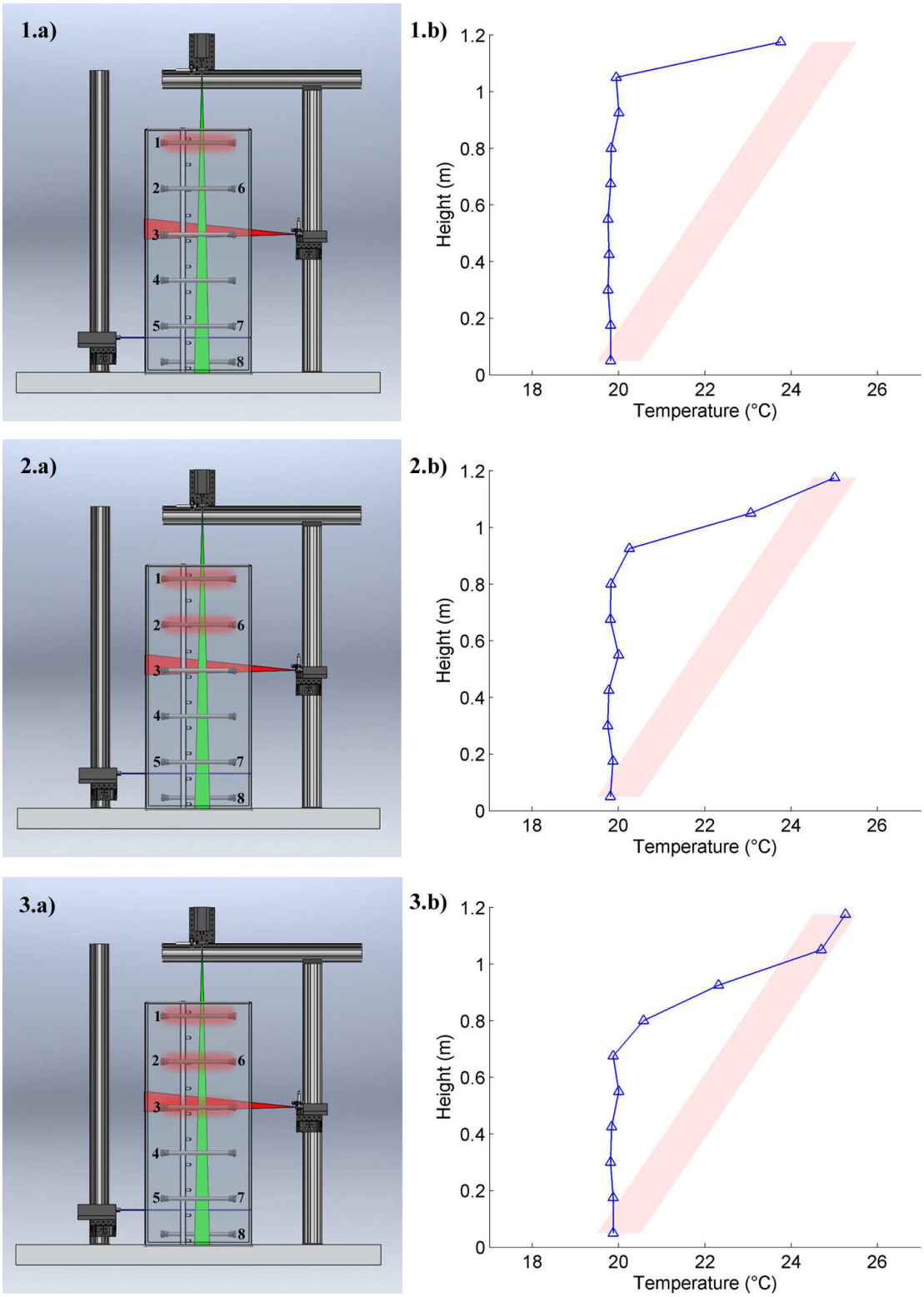

Figure 2.7: Thermal stratification of the water column: Part (a). Series of illustrations depicting the first-half of the thermal stratification process. Heaters labeled on the left-hand side of the water column are positioned at the back wall and those labeled on the right-hand side at the front wall of the tank. The red shadowed regions in all (b) parts indicate the final permissible temperature range. Heater 1 is the first to be activated (1a), which raises the temperature of the upper region of the water column (2a). Heaters 2 and 6 are subsequently triggered (2a), resulting in the temperature gradient shown in (2b). Heater 3 is turned on afterwards (3a), warming up the upper half of the water column (3b).

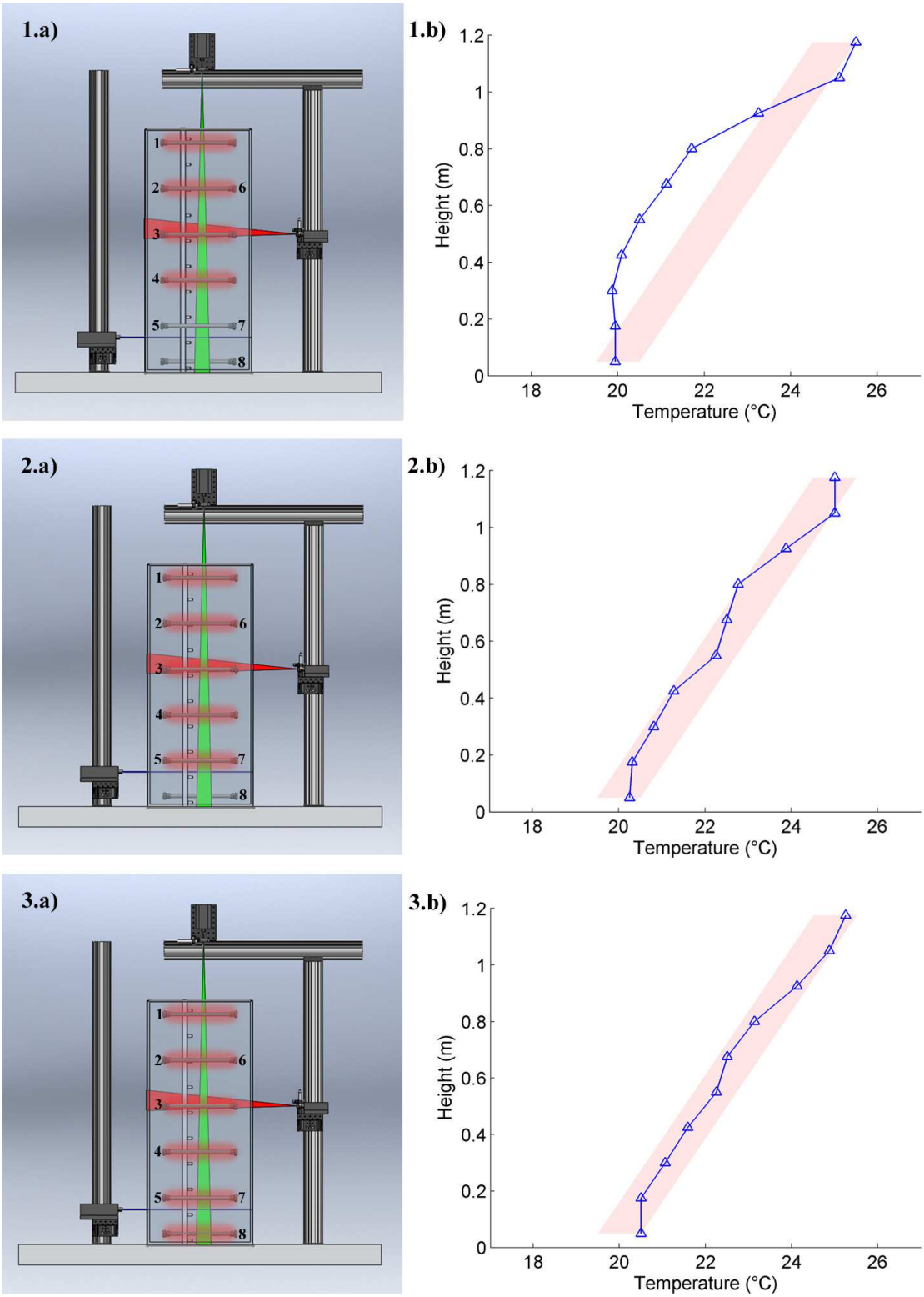

Figure 2.8: Thermal stratification of the water column: Part (b). Series of illustrations depicting the second-half of the thermal stratification process. Heaters labeled on the left-hand side of the water column are positioned at the back wall and those labeled on the right-hand side at the front wall of the tank. The red shadowed regions in all (b) parts indicate the final permissible temperature range. Once the temperature above heater 4 has shifted above room temperature, this unit is switched on (1a), producing the profile in (1b). Similarly, heaters 5 and 7 (2a) as well as 8 (3a) are activated, resulting in (2b) and (3b), respectively.

Chapter 3

Animal-fluid Interactions During Vertical Collective Motion

3.1 Introduction

As discussed in Chapter 1, transport by the turbulent wake of swimming organisms and Darwinian drift are the two known mechanisms for fluid transport relevant during DVM. Estimates of their mixing efficiency have been proposed based on microstructure data during vertical migration in the field as well as on in situ observations of single swimmers, yielding different conclusions (see [100] & [37], for example). This discrepancy results from assumptions based on two yet unanswered questions:

- can small self-propelled swimmers migrating collectively across the ocean stable stratification create fluid structures larger than the cut-off for vertical density overturns known as the Ozmidov buoyancy length scale? And
- how does the observed Darwinian drift develop within migrating groups of smaller species of zooplankton that undergo DVM?

Even though it has been argued that swimming organisms cannot generate fluid structures larger than their own body length [100], it has been experimentally demonstrated that small self-propelled marine organisms such as krill, for example, are able to generate hydrodynamic trails larger than themselves [108], [104]. Furthermore, reports indicating the existence of regions of large overturns ($1 - 10$ m) in the vicinity of a migrating dense krill swarm in Saanich Inlet, British Colom-

bia have received little to no attention [42], [43]. How it is that swarms of small organisms are able to form these large unstable regions has not been addressed. Furthermore, the disconnect between the energy distribution within these scales and the measured energy dissipation at the microscale has resulted in the subsequent disregard of this fact in the literature.

In this chapter, fluid transport due to the vertical migration of *A. salina* in a non-stratified medium is investigated in an effort to identify the fundamental fluid transport mechanisms that occur during DVM. The main objectives are to identify transport processes that emerge from the vertical migration of small zooplankton aggregations and to determine the length scales at which mechanical energy is introduced into the flow. At the beginning of the chapter, the resulting flow field is discussed in terms of local fluid transport in the near-field of swimming organisms (§3.2) as well as the far-field signature of the entire aggregation (§3.3). The energy distribution within resulting fluid structures is discussed in §3.4 followed by observations of large-scale coherent structures in the vicinity of the migrating aggregation in §3.5. Finally, a brief discussion is provided in §3.6.

3.2 Local Fluid Transport

As shown in §2.2, *A. salina* propels itself forward by rowing its eleven pairs of developed limbs. Similarly to many other species of crustaceans that undergo DVM, appendage coordination results in a metachronal wave-like motion. The simplest example of a metachronal wave is the Mexican wave that commonly takes place during a soccer match. Likewise, organisms beat their appendage pairs periodically such that the motion of a given pair during a stroke has a phase-lag with its neighboring limbs. Once the appendages in the anterior part of the body of the organism have completed the stroke, the legs at the posterior begin a new stroke. As a result, the organism is able to swim faster and efficiently compared to propulsion via synchronous motion of all appendage pairs [3]. Different gaits have been identified for a single species—such as cruising, hovering, and escape—depending

on the hydrodynamic requirement of the critters [61]. Here, it was observed that organisms swam quasi-steadily during upwards DVM, and hence only this swimming gait was analyzed.

PIV measurements were acquired as outlined in §2.4.1 during vertical migration of *A. salina*. Raw images were post-processed in Matlab to track the position of organisms within the focal plane and whose trajectory did not coincide with that of another swimmer. As shown in Figure 3.1, the swimming speed of an organism can then be estimated by dividing the distance between the position of its centroid at two frames to the time between those frames. Analysis of all experimental sets yielded an average swimming speed of 1 cm/s, which coincided with the translating speed of the blue laser beam that prompted upward animal motion. Taking the organism body length as characteristic length, the Reynolds number $Re = 50$ was within the range reported for krill and copepods [41], [108].

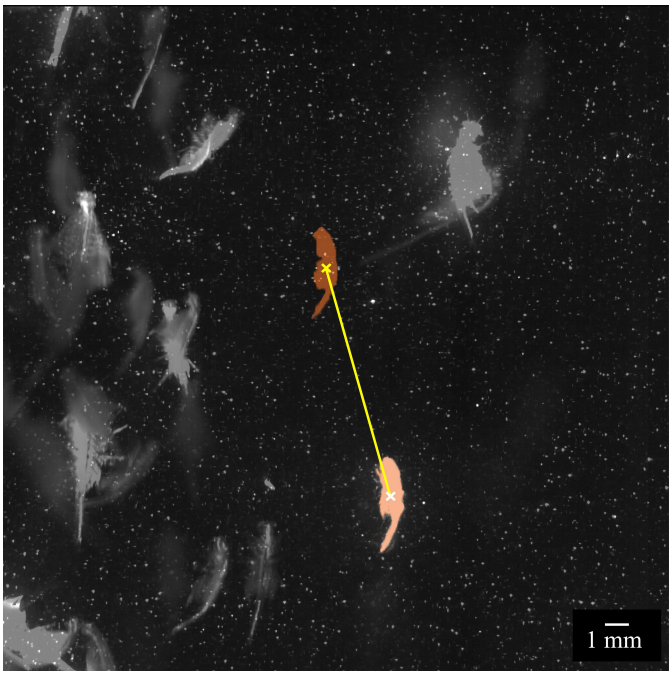

Figure 3.1: Organism centroid displacement calculation. An overlay of two raw PIV images of a representative experimental set is shown to illustrate the distance travelled by one organism. The lighter shadowed animal corresponds to the tracked organism at some time $t = t_1$, whereas the darker shadowed one corresponds to the same animal at time $t = t_1 + \Delta t$. The position of the centroid is marked by a yellow cross. The swimming speed of the organism is estimated as the distance between centroids (yellow line) divided by Δt.

Further analysis of the acquired PIV measurements allowed sporadic inspection of the near-field flow due to individual organisms. It was observed that the generated near flow of a single vertically-migrating *A. salina* varies between its ventral and dorsal sides. During the power stroke of the propulsive cycle, the metachronal motion of the organism appendages resulted in a quasi-steady downward jet, which persisted during the entire swimming cycle (see Figure 3.2a). In contrast, upward fluid motion was observed to be induced by the ventral side during the recovery stroke and by the dorsal side during upward animal motion (Figure 3.2b). The net direction of near-field fluid transport over the swimming cycle was found to be downward (i.e., opposite to the swimming direction), in contrast with previous observations of jellyfish [37]. However, both results are consistent with recent theoretical models [77] that predict a dependence of the net direction of induced drift on the swimming mode of the organism [50],[91],[86]. Moreover, this hydrodynamic feature has also been reported for marine crustaceans that undergo DVM, such as *Euphausia Pacifica* and *Daphnia* [108], [104].

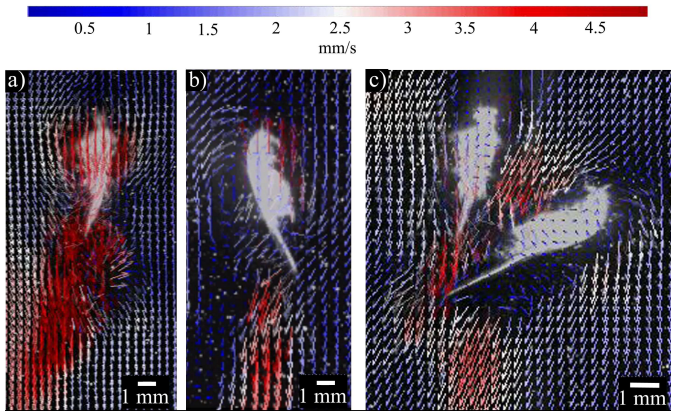

Figure 3.2: Near-field flows during DVM. Near-field flows generated by the metachronal motion of the appendages of an individual organism (a), by the dorsal side of an individual organism (b), and by two organisms in close proximity (c).

Additional experiments were performed with individual organisms in a smaller setup to better visualize these hydrodynamic features [1]. Variable inter-animal spacing during collective vertical motion facilitated the observation of individually-generated hydrodynamic trails but subsequent interaction with neighboring swim-

[1]Data was acquired by summer student Samantha Collins and the results presented here are reproduced under her permission.

mers inhibited further analysis (Figure 3.2c, for example). Following the developed laboratory guidelines to study vertical migration of zooplankton, a smaller version of the laboratory apparatus was implemented. A single organism was deposited in a plexiglass container filled with 15 ppt artificial seawater pre-mixed with 13 μm silver-coated hollow glass spheres (Potter Inc.) at room temperature. The organism was guided to the bottom of the container with a secondary light source. Vertical migration was triggered from the bottom of the container to the top by the subsequent generation of a green-laser sheet at the top of the tank. Videos were acquired within a two-dimensional plane at the center of the tank with a Sony Handycam at 30 fps. Instantaneous images were processed using PIVlab (a Matlab open-source routine for PIV processing) with a multipass method of decreasing window size from 64x64 to 32x32 with 50% overlap. The resulting velocity fields were validated through a post-processing routine primarily consisting of standard deviation and local median filters.

The development of the downward jet during the recovery stroke in the aforementioned set of experiments is shown in Figure 3.3. From these observations, it is evident that the vertical span of the generated jet is larger than the size of the organism. In addition, the metachronal motion of the appendages creates recirculating areas near the body that are smaller than the organism body length (Figure 3.4). Going back to the theoretical estimates of biogenic mixing efficiency presented in Chapter 1, these small scales are often taken to correspond to the hydrodynamic footprint of a vertically swimming organism. However, as seen in Figure 3.3, additional large-scale features are present, which could induce efficient mixing via the vertical advection of fluid across a stable density stratification.

In congruence with measurements obtained during vertical collective motion, it was observed that the upward drift along the passive dorsal side of the organism is outweighed by the downward jet during upward propulsion (Figure 3.5). Sudden rotation of the organism as it was swimming upwards allowed direct comparison of both effects (Figure 3.6).

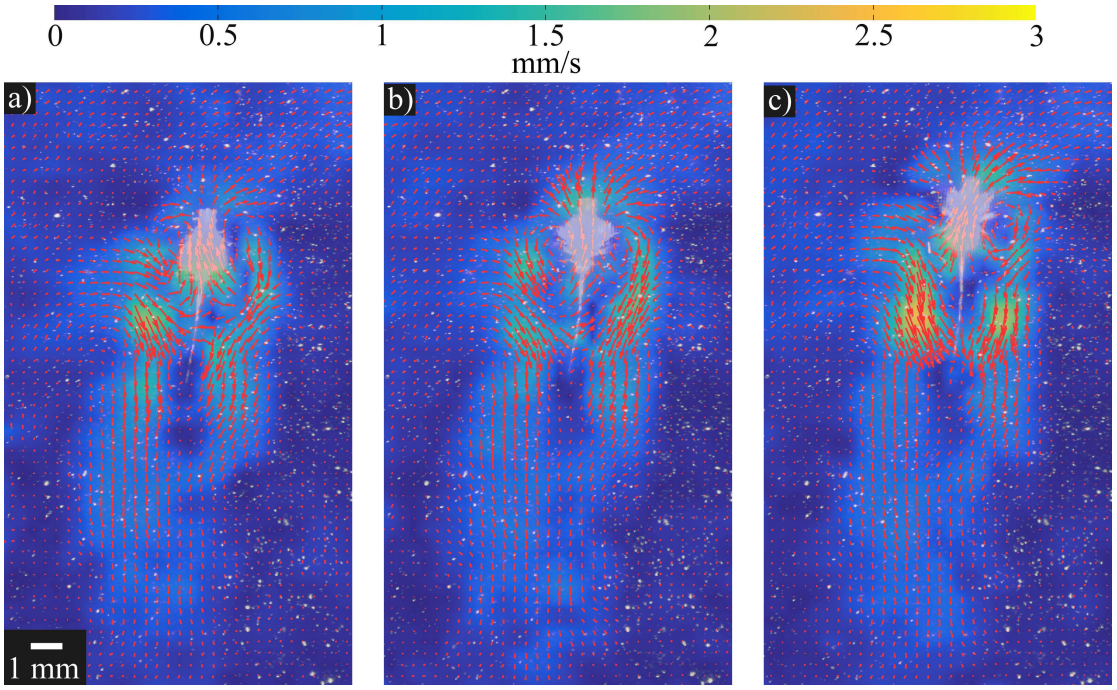

Figure 3.3: Near-field flow along the ventral side of a vertically migrating *A. salina*. The jet generated by the metachronal motion of the appendages of an individual organism is shown during the time-lapse of a recovery stroke (a) - (c).

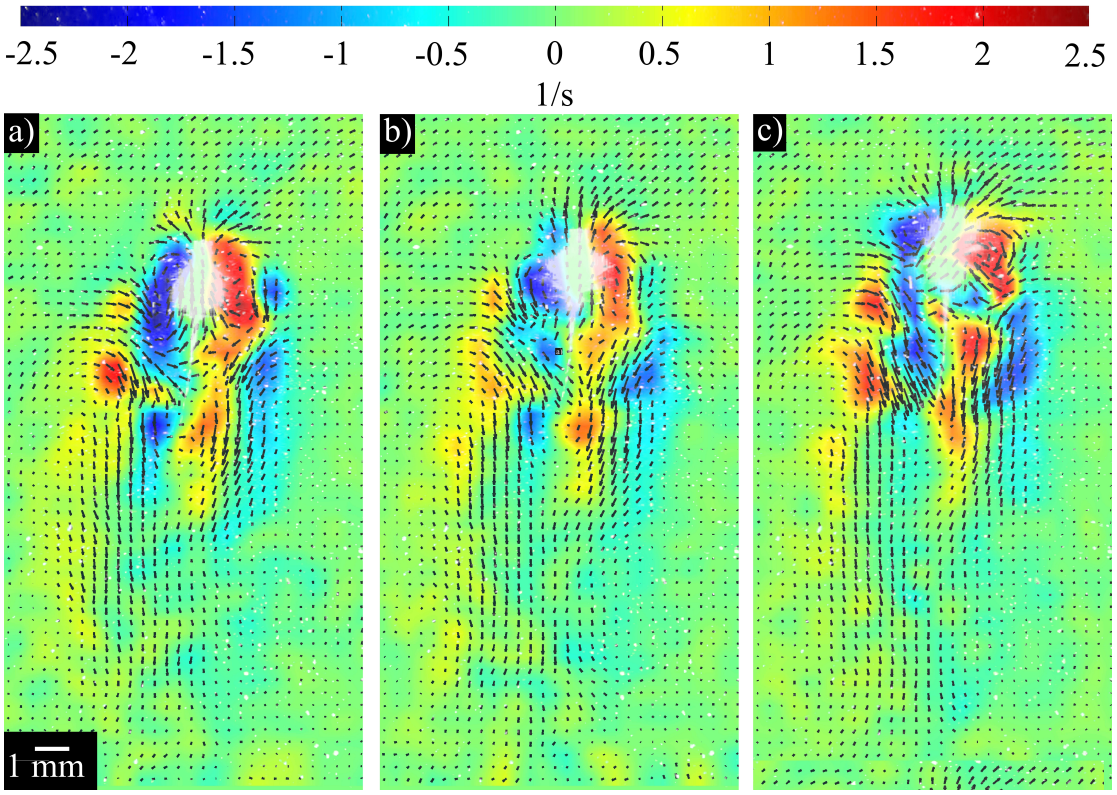

Figure 3.4: Vorticity field along the ventral side of a vertically migrating *A. salina*. The vorticity generated by the metachronal motion of the appendages of an individual organism is shown during the time-lapse of a recovery stroke (a) - (c).

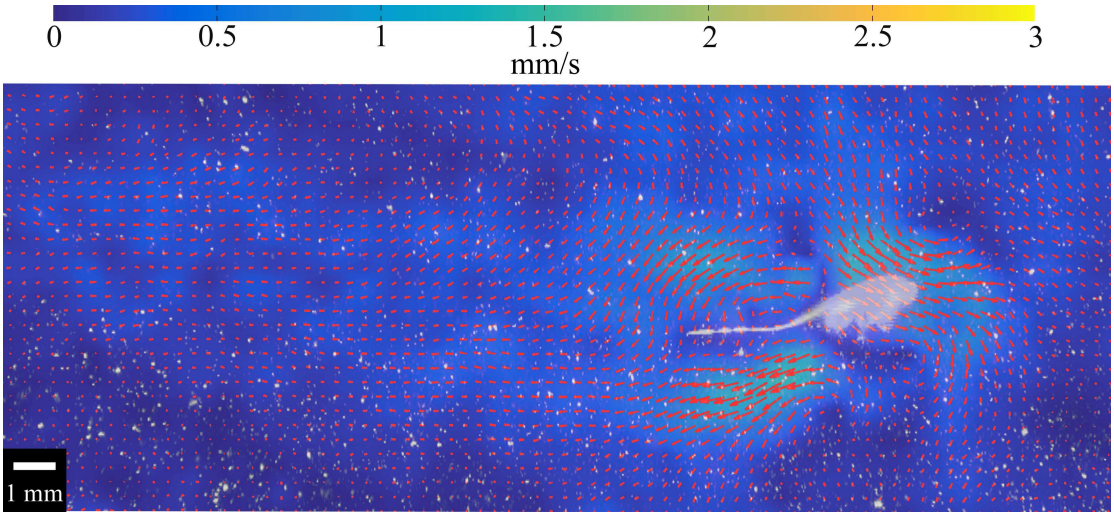

Figure 3.5: Near-field flow along the dorsal side of a vertically migrating *A. salina*. The image is shown rotated 90°to the right.

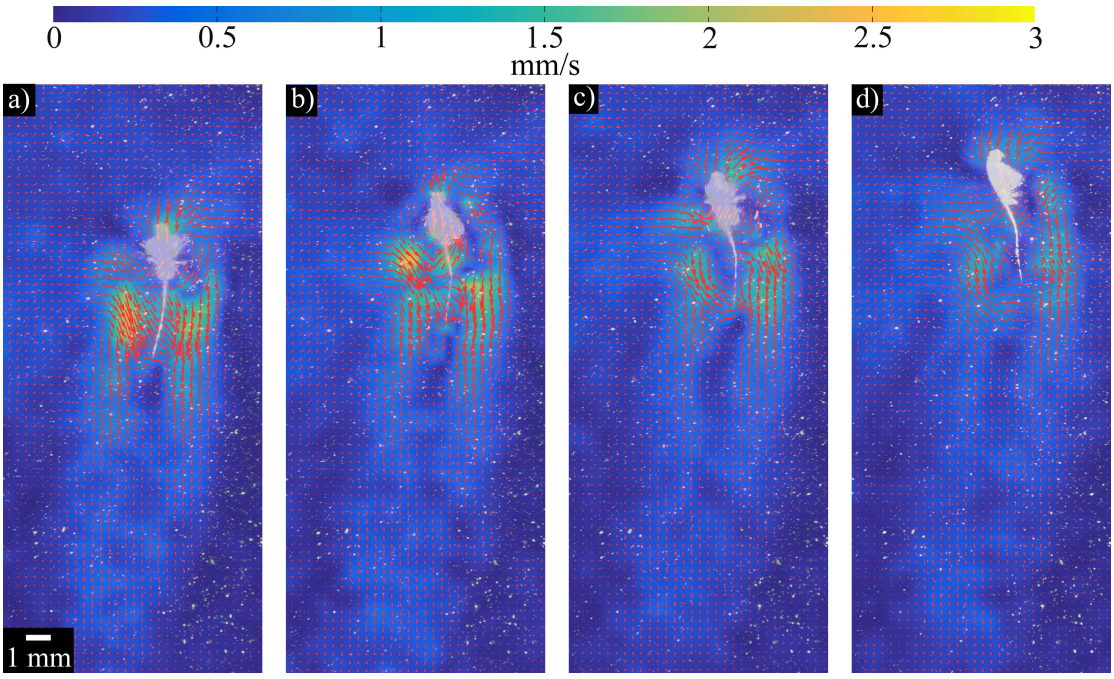

Figure 3.6: Counter-acting hydrodynamic features during vertical propulsion of *A. salina*. The flow field along both the dorsal and ventral sides are shown for a freely swimming organism (a) - (d). Initially, the organism was oriented such that the jet resulting from the metachronal motion of its appendages was observable (a), as time progresses self-rotation of the body allowed measurement of the near-field flow along its dorsal side (d).

3.3 Far-field Hydrodynamic Signature

As mentioned in the previous section, complex hydrodynamic interactions occurred as two or more organisms came in close proximity during collective vertical migration (Figure 3.2c). Synergy of the near-field flow of neighboring organisms enhanced downward fluid advection via the development of a pronounced downward jet. The time series presented in Figure 3.7 displays this process, in which two organisms spontaneously came in close proximity and continued migrating upwards, leaving a coherent trail behind.

A synopsis of the acquired measurements at the beginning of the migration ($\tau_2 =$ 47 s) is presented in Figure 3.8 for the same experimental set. Figure 3.8a is representative of the flow conditions as organisms start migrating upwards. The interactions shown in Figure 3.7 occurred in between panels a and b of Figure 3.8. The hydrodynamic trail generated from the interaction of two swimmers during vertical migration persisted long enough to contribute to the flow generated by subsequent migrating swimmers. Further development of the jet is observed as the migration progresses over time (Figure 3.8). As described in §2.3, organisms are concentrated within the left side of the field of view due to the alignment of this side with the center of the green laser sheet.

Measurements corresponding to the middle of the migration ($\tau_3 = 67$ s) are shown in Figure 3.9. The downward jet generated by the active ventral side of a single organism indeed dominated over the weak upward fluid drift induced along the passive side of the body and by the appendages during the recovery stroke. As a result, as the migration developed, collective animal motion incited a strong downward flow, characterized by a persistent, but spatially intermittent, downward jet that diverged over time.

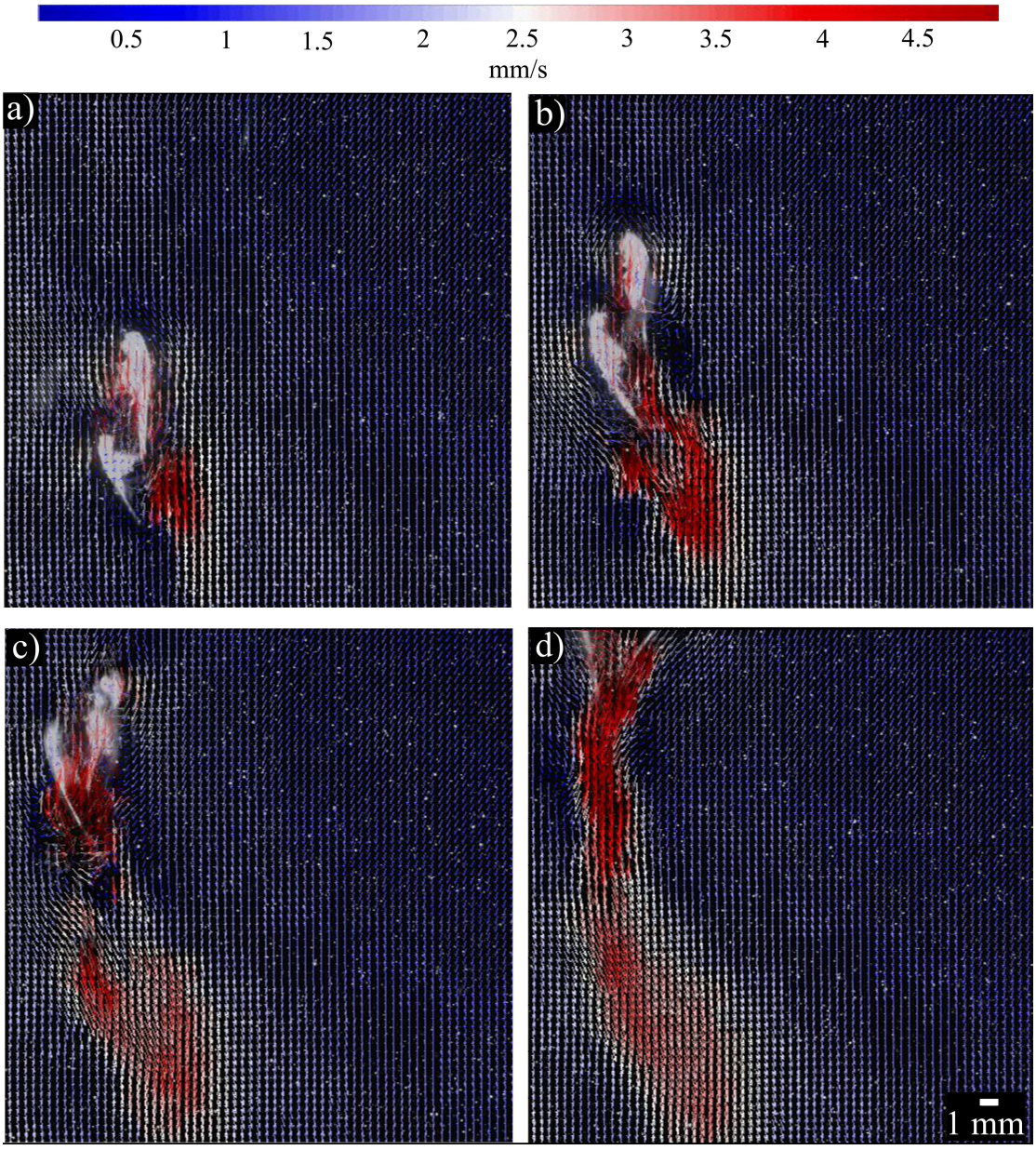

Figure 3.7: Animal-fluid interactions between neighboring organisms during DVM. The development of a single jet was observed at the beginning of the vertical migration as two organisms swam upward in close proximity. The presented time series (a - d) was acquired 61 s after the migration had been triggered, i.e., $\tau_2 + 14$ s. Images are shown with a time lapse of $\Delta t = 56$ ms.

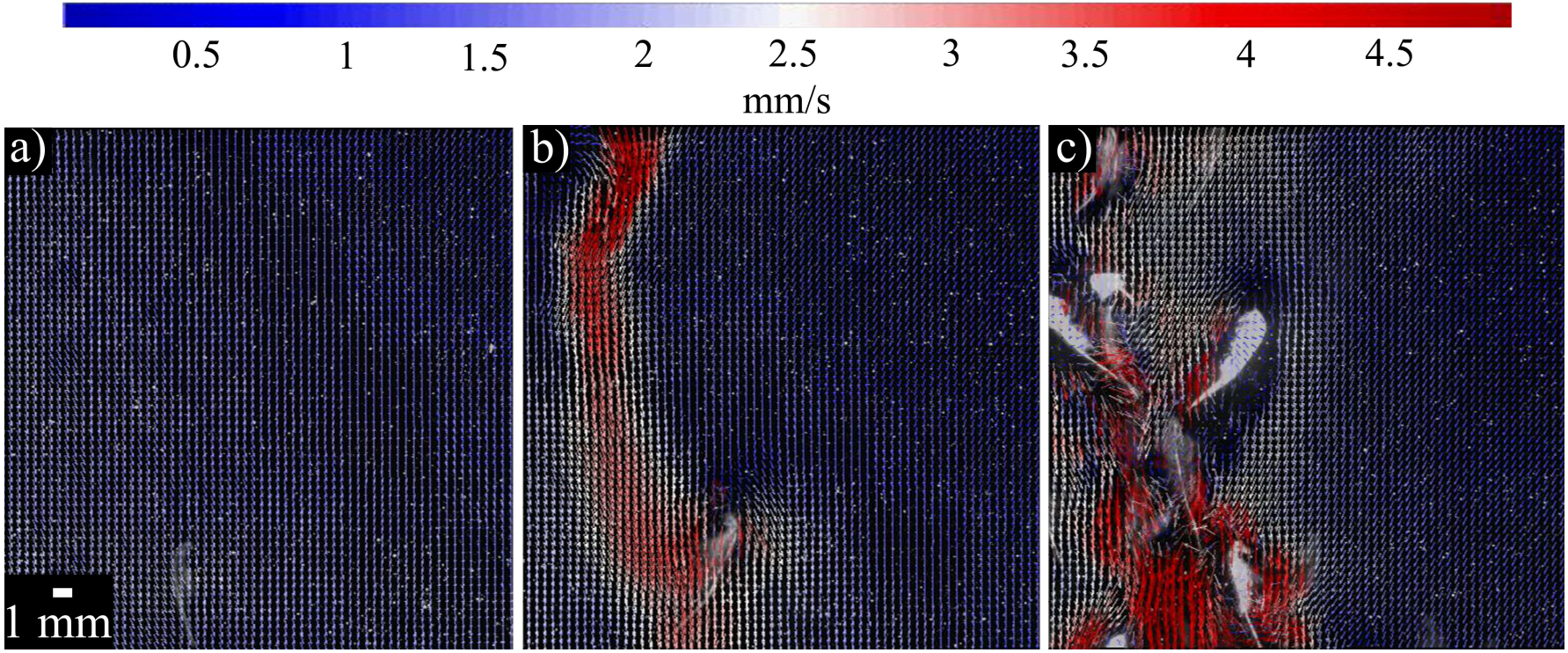

Figure 3.8: Velocity field measurements during the initial stage of DVM. Time series for a representative set acquired with the second time delay ($\tau_2 = 47$ s), which corresponds to the beginning of the migration. The onset of the downward jet and its subsequent evolution is shown for the following times: $t = \tau_2 + 8$ s (a), $t = \tau_2 + 16$ s (b), $t = \tau_2 + 24$ s (c).

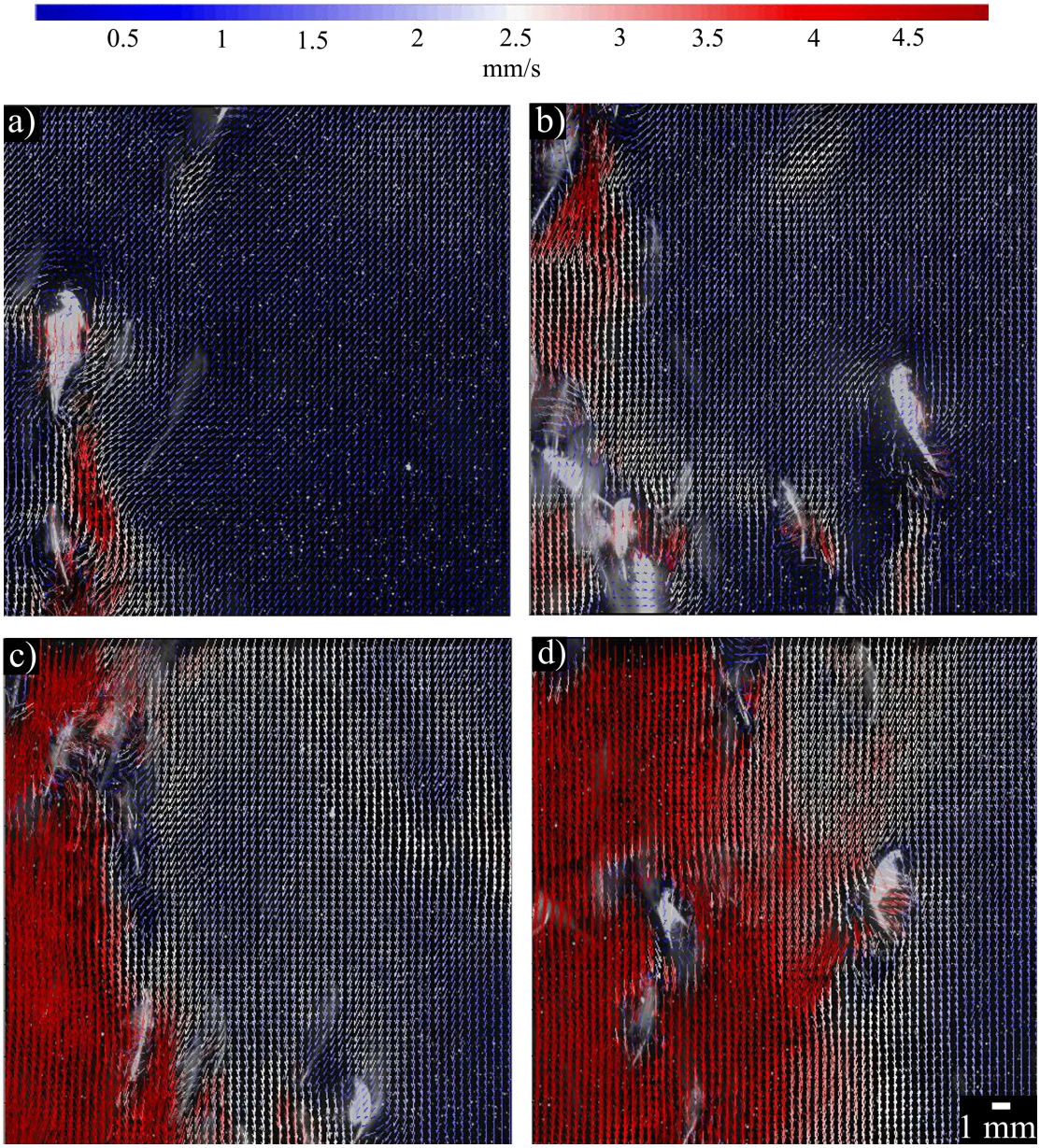

Figure 3.9: Velocity field measurements during DVM. Time series for a representative set acquired with the third time delay ($\tau_3 = 67$ s), which corresponds to the middle of the migration. The development of the downward jet is shown for the following times: $t = \tau_3$ s (a), $t = \tau_3 + 8$ s (b), $t = \tau_3 + 16$ s (c), $t = \tau_3 + 24$ s (d).

Qualitatively, the generated flow field defies the previous assumption of a fully non-turbulent flow in this Reynolds number range [41]. Granted, a critical value of approximately $Re = 1000$ is needed to reach fully developed turbulence. However, some aspects of turbulence are identifiable in the measured velocity fields, such as their irregularity, which suggests that this flow results from the interaction of hydrodynamic instabilities which could evolve to a turbulent state. In any case, the velocity time series at each PIV measurement node ($\tilde{u}_i$) can be simplified into

the contribution of a mean flow component (U_i):

$$U_i = \frac{1}{N}\sum_{n=1}^{N} \tilde{u}_{i_n} \qquad i = 1, 2 \ , \tag{3.1}$$

and that of a fluctuating component (u_i) [90], [76]:

$$u_i = \tilde{u}_i - U_i \qquad i = 1, 2 \ , \tag{3.2}$$

where N indicates the total number of acquired measurements and the subscripts $i = 1$ and $i = 2$ refer to the horizontal and the vertical direction, respectively.

The time series of the fluctuating vertical velocity component (u_2) is shown normalized by its root-mean-square (rms) value ($u_{2_{rms}}$) at different PIV measurement nodes spanning the camera field of view for a representative test of each experimental set in Figures 3.11 - 3.13. A set of four additional measurements was done following the laboratory procedures detailed in §2.4.1, but without organisms in the tank. Velocity measurements of a representative test of this control set are presented in Figure 3.10. The rms velocity is a measure of the strength or intensity of a turbulent velocity and is defined as:

$$u_{i_{rms}} = \sqrt{\overline{u_i^2}} \qquad i = 1, 2 \ , \tag{3.3}$$

where the overbar denotes a temporal mean (over the full measurement period). As shown in Figure 3.10, the temporal record of $u_2/u_{2_{rms}}$ corresponding to the control set displays a random signal evenly distributed above and below the mean. On the other hand, the time series of the normalized fluctuating velocity acquired during vertical migration changes sign, due to an increase of the absolute magnitude of the velocity at the given measurement node as the migration progresses (Figures 3.11, 3.12 and 3.13). At the beginning of the migration, this trend is displayed at some locations, where $u_2/u_{2_{rms}}$ is mainly positive throughout the record, except at approximately the last quarter (Figure 3.12). This is also observed in Figure 3.13, corresponding to measurements taken later in the migration, where the sign change occurs at half the time span of the signal.

A striking feature of the temporal evolution of $u_2/u_{2_{rms}}$ is the intermittent presence of high intensity bursts during vertical migration (Figures 3.12 and 3.13). As shown in Figure 3.11, this aspect was not observed in the velocity measurements acquired prior to migration, nor in the velocity time series of the control tests done without organisms in the water column (Figure 3.10). Inspection of the velocity fields during these occurrences showed that these features are caused whenever an organism strikes its appendages at that position (Figure 3.14).

To confirm the intermittent nature of the flow, the probability density function (PDF) of the normalized fluctuating vertical velocity component was computed for all experimental sets and the control case described above (Figures 3.15 - 3.18). As shown in Figure 3.15, the PDF of $u_2/u_{2_{rms}}$ for the experimental set corresponding to flow conditions without organisms in the water tank displays a Gaussian distribution, as expected. This normal distribution was observed at every measurement node for each of the acquired control tests. Interestingly, however, the PDF corresponding to the velocity measurements acquired prior to vertical migration exhibits a bimodal distribution at some PIV nodes (Figure 3.16), even though the flow conditions in this case were observed to be similar to the control set as seen from the processed velocity field (Figure 3.8) as well as the time series of $u_2/u_{2_{rms}}$ (Figure 3.11). As the migration progressed in time, a bimodal distribution was more frequently observed and, moreover, it was found to increasingly exhibit long tails at some positions of the PIV measurement field (Figures 3.17 & 3.18).

This type of distribution has been documented for measurements in experimentally generated turbulent flows acquired directly behind passive and active grids and has been attributed to the nature of multi-scale interactions and intermittence of the flow in the regions close to the grid [23], [56], [33]. The proposed physical interpretation is that the fluid coming from in between the elements composing a variably spaced turbulence-generating grid results in the confluence of flows characterized by different scales producing this bimodal behavior in the distribution of

the fluctuating velocity [23]. Furthermore, similar to the measurements acquired during vertical migration, the PDF exhibits long tails with a kurtosis larger than that of a normal distribution ($\gamma_2 > 3$).

The kurtosis or fourth standardized moment is a measure of the tail weight in a PDF and is defined as:

$$\gamma_2 = \frac{\overline{u_i^4}}{\sigma^4} = \frac{\overline{u_i^4}}{u_{i_{rms}}} \quad . \tag{3.4}$$

In the literature, this measure (also referred to as flatness factor) is taken as an indicator of what is known as intermittency (also external intermittency) in the flow, if its value is larger than that of a normal Gaussian distribution ($\gamma_2 = 3$) [81]. The concept of intermittency refers to the nature of some flows to alternately display bursts of turbulence, such as those displayed in Figures 3.12 and 3.13 [95]. This phenomenon has been observed to occur at the free-stream edge of shear flows such as jets, wakes, and turbulent boundary layers [90], [94], [73]. As will be discussed in §3.4.2, this has important implications regarding the distribution of energy among different scales within the flow.

The kurtosis was computed at every PIV measurement node for each experimental test and compared to that of a Gaussian distribution. This information is summarized in Table 3.1 for all experimental sets. These values confirm that intermittency of the flow increases as the migration progresses, as observed in Figures 3.15 - 3.18.

Experimental set	Percentage of PIV measurement nodes at which $\gamma_2 \geq 3$
No organisms	7%
Prior to DVM (τ_1)	4%
Beginning of DVM (τ_2)	63%
During DVM (τ_3)	88%

Table 3.1: Percentage of intermittent PIV nodes for all experimental sets.

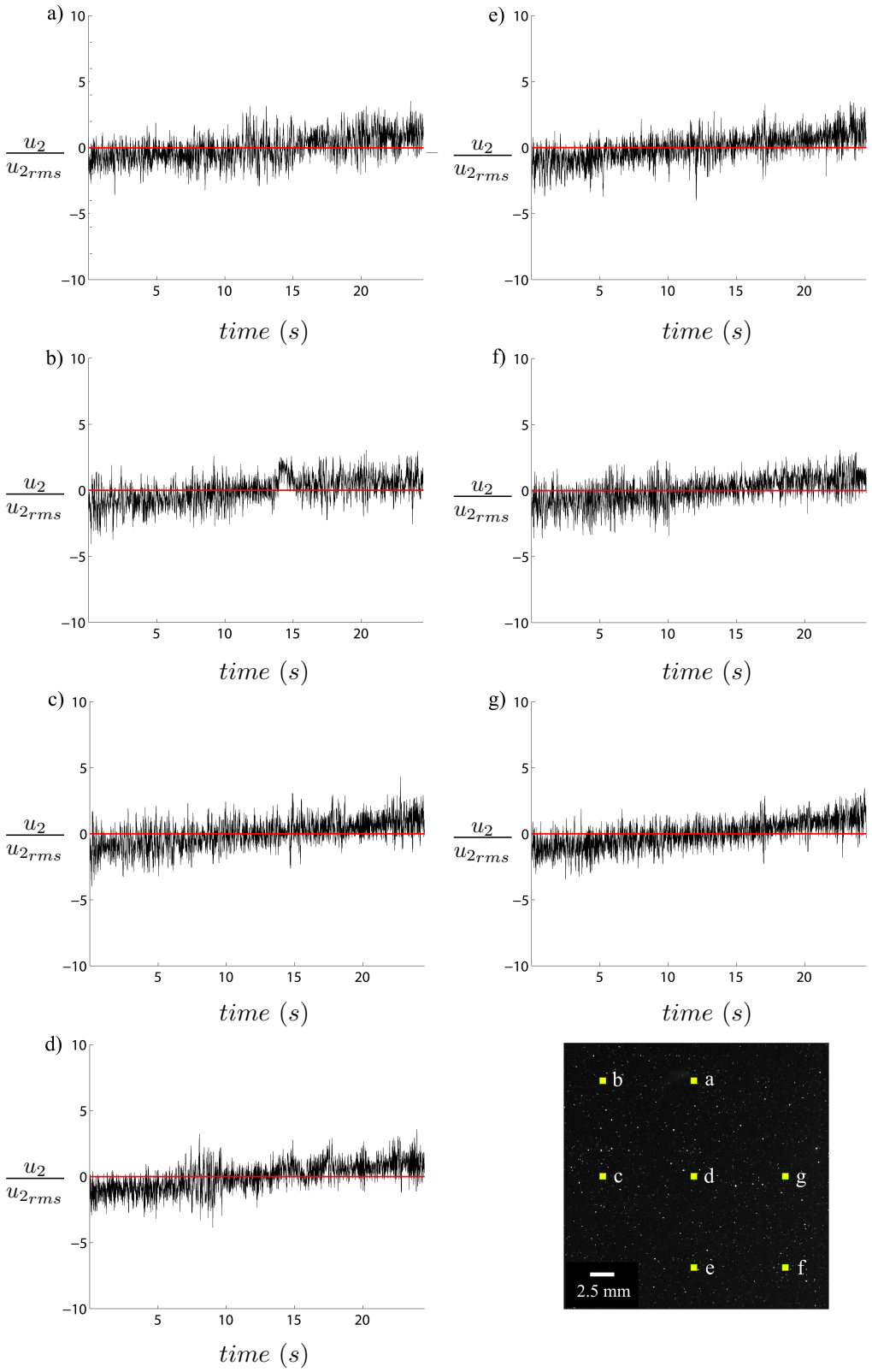

Figure 3.10: Time series of the fluctuating vertical velocity component for a control test without organisms. The magnitude of u_2 is shown normalized by $u_{2_{rms}}$ at the positions indicated in the raw PIV image. These measurements were taken following the procedures outlined in §2.4.1 to simulate an experiment, but no organisms were introduced into the tank.

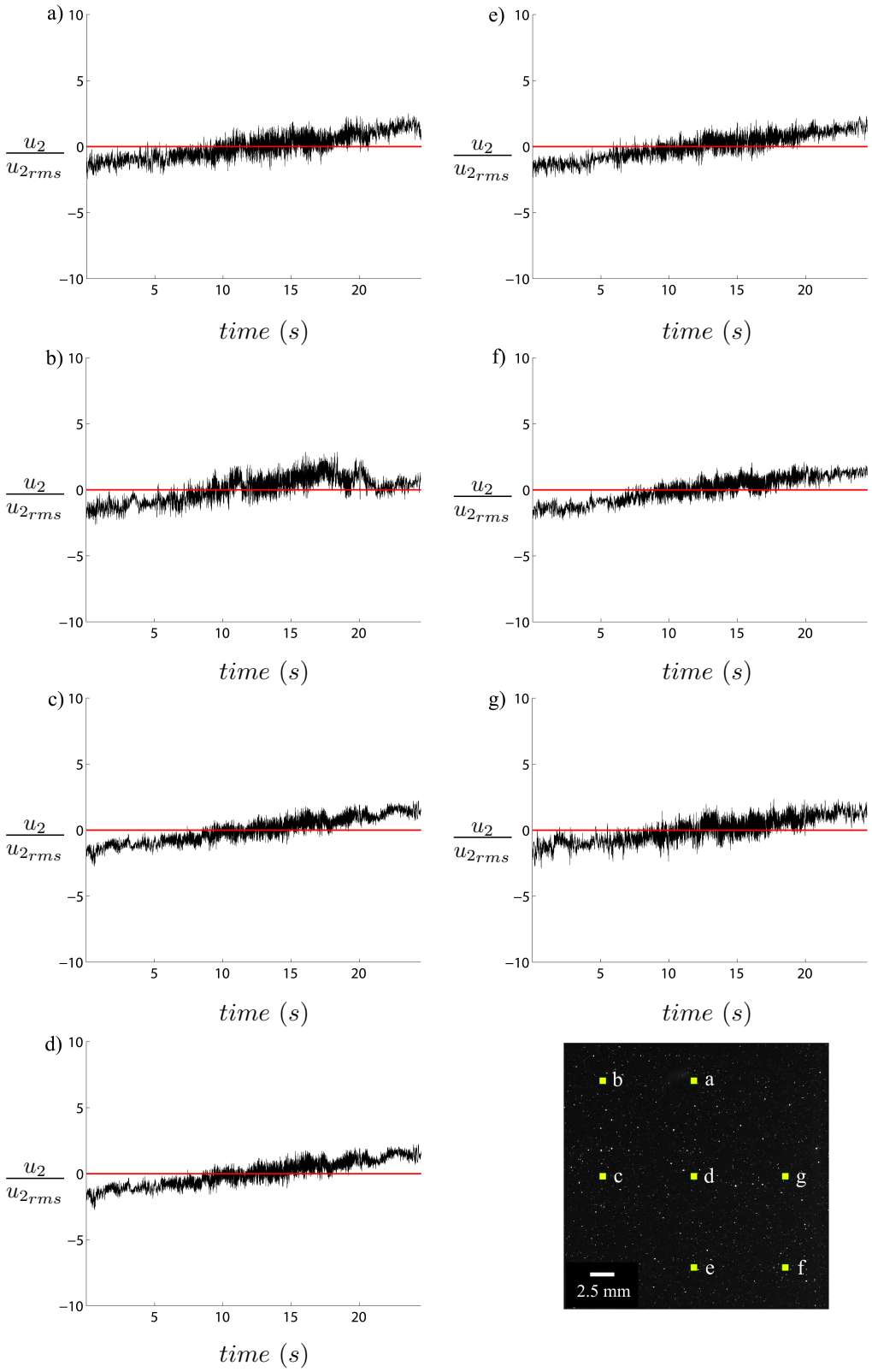

Figure 3.11: Time series of the fluctuating vertical velocity component prior to DVM. The magnitude of u_2 is shown normalized by $u_{2_{rms}}$ at the positions indicated in the raw PIV image. These measurements are a representative set of data acquired prior to vertical migration at the first time delay (τ_1).

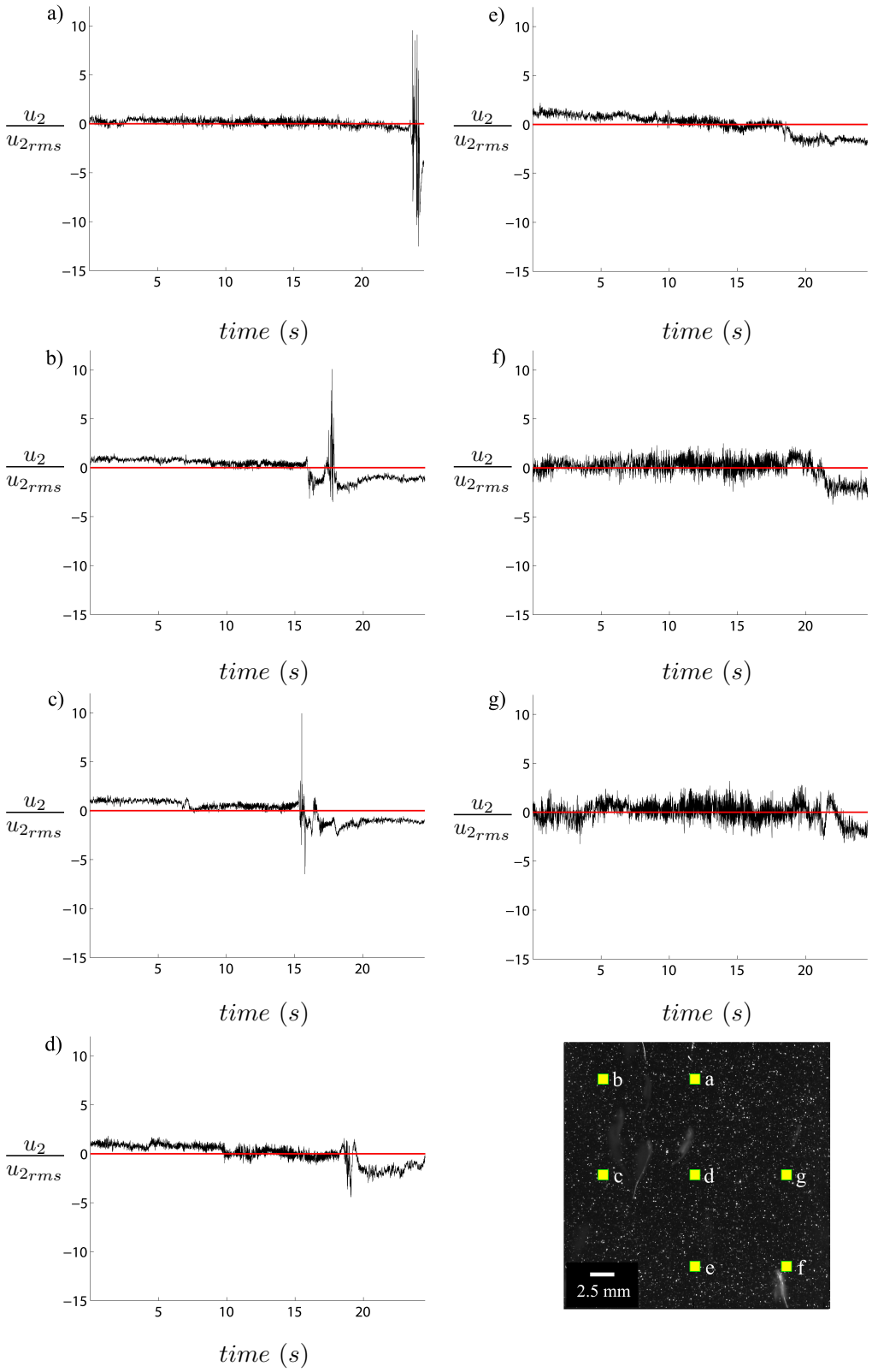

Figure 3.12: Time series of the fluctuating vertical velocity component during the initial stage of DVM. The magnitude of u_2 is shown normalized by $u_{2_{rms}}$ at the positions indicated in the raw PIV image. These measurements are a representative set of data acquired during the beginning of the migration at the second time delay (τ_2).

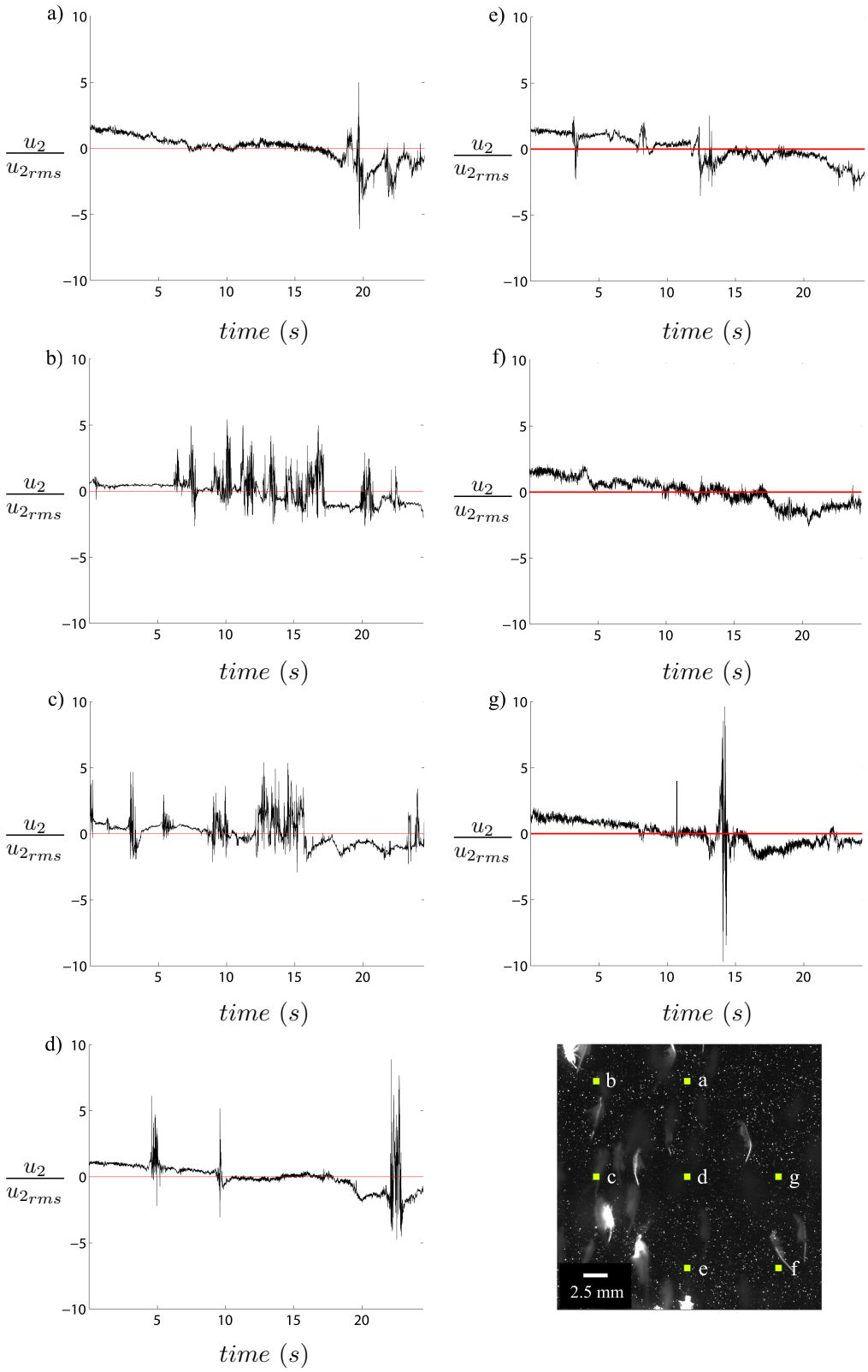

Figure 3.13: Time series of the fluctuating vertical velocity component during DVM. The magnitude of u_2 is shown normalized by $u_{2_{rms}}$ at the positions indicated in the raw PIV image. This measurement corresponds to the experimental test presented in Figure 3.9, which was taken at the third time delay (τ_3).

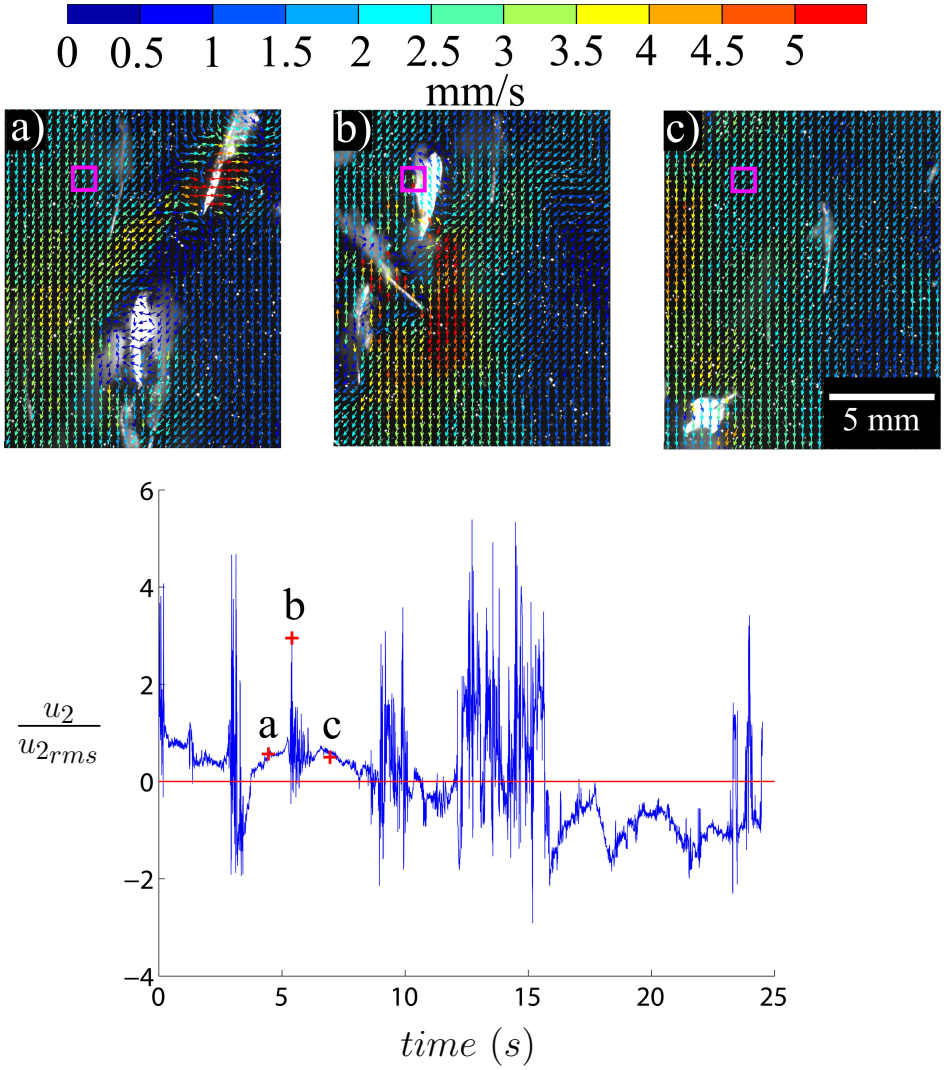

Figure 3.14: Velocity field and time series at a representative measurement node during animal migration. The velocity field at point c in Figure 3.13 is shown for different times during a high-intensity burst, corresponding to panels a, b, and c.

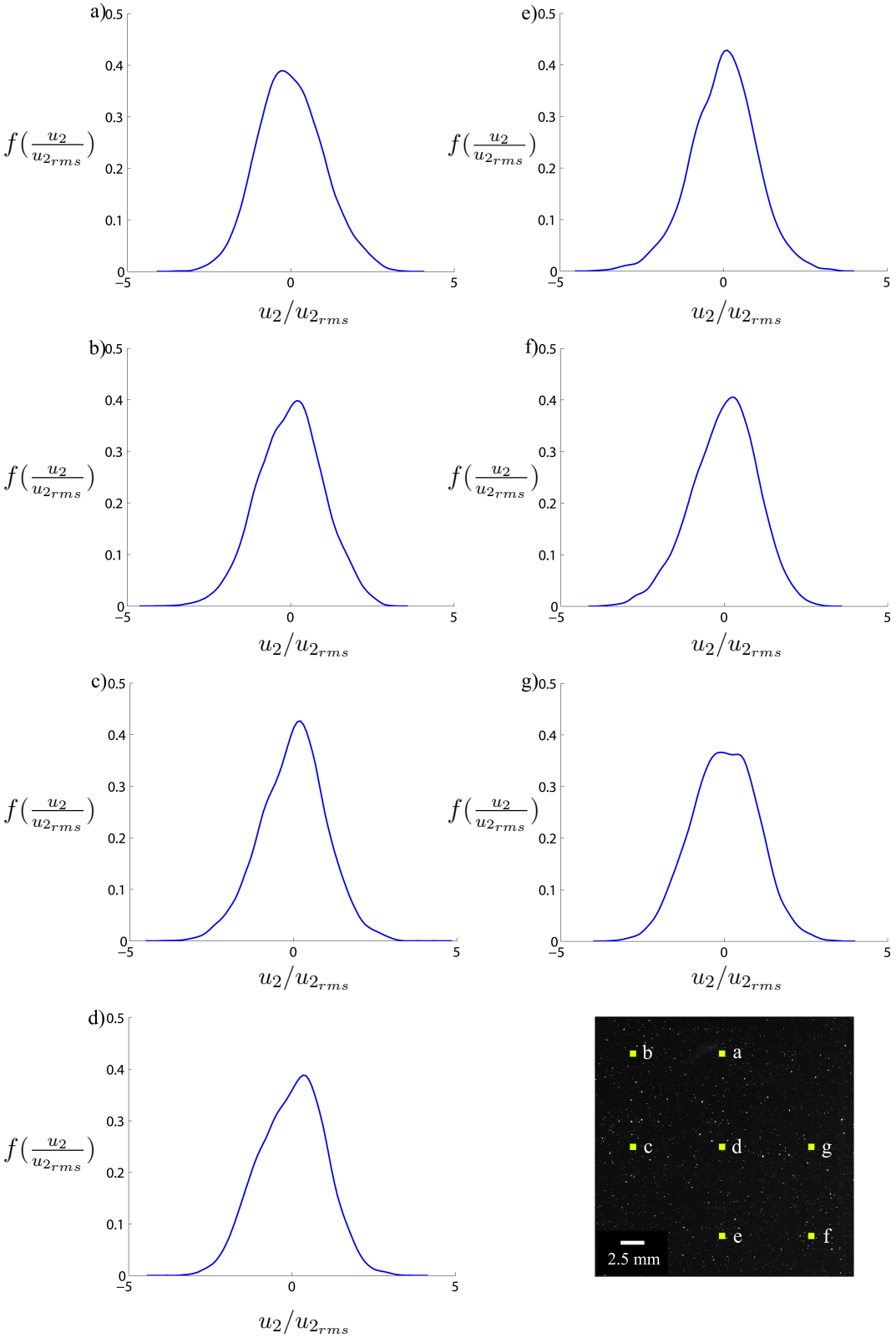

Figure 3.15: PDF of the fluctuating vertical velocity component for a control test without organisms. The distribution of the normalized velocity $f(u_2/u_{2_{rms}})$ is shown at the positions indicated in the raw PIV image. This measurement set corresponds to the one in Figure 3.10.

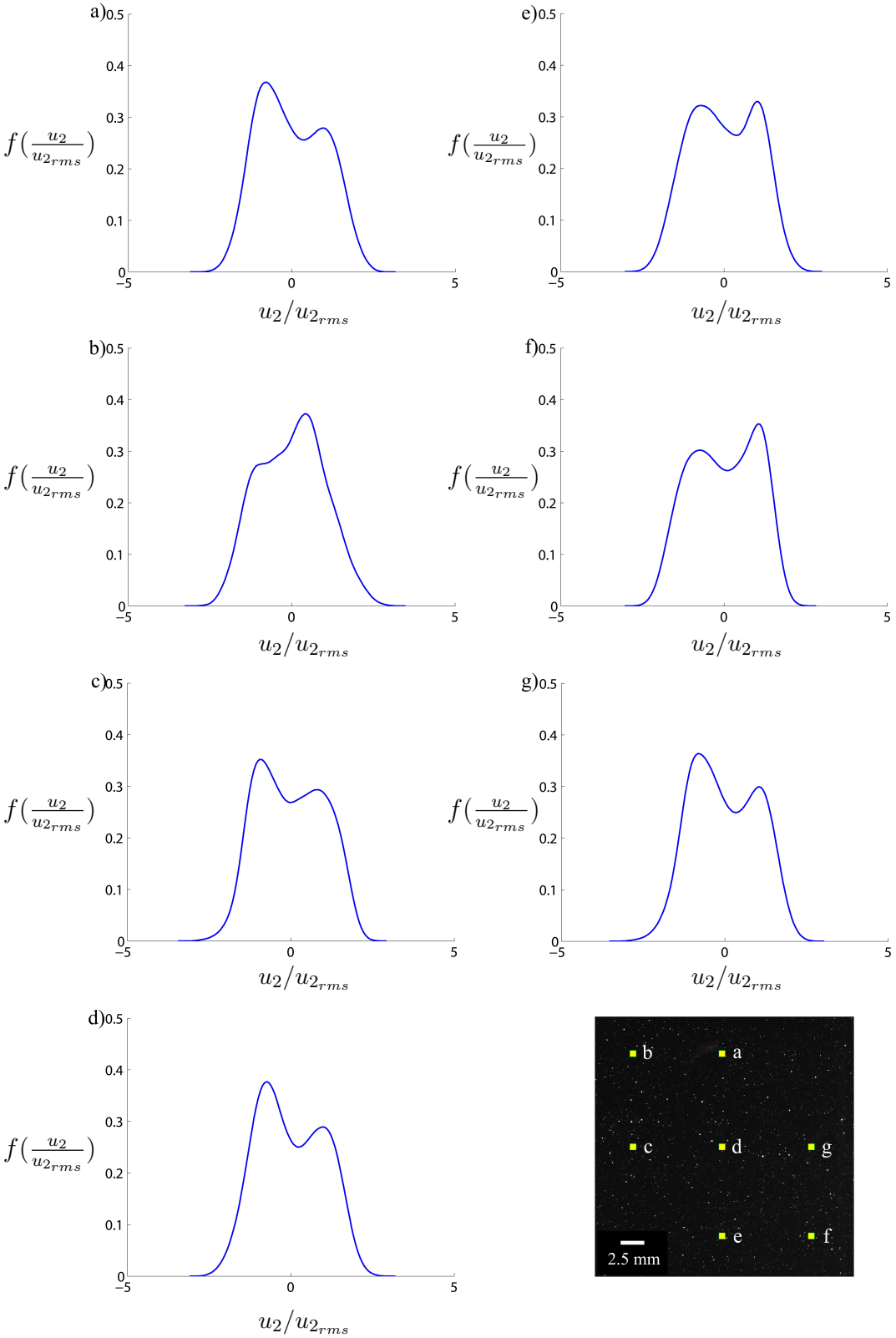

Figure 3.16: PDF of the fluctuating vertical velocity component prior to DVM. The distribution of the normalized velocity $f(u_2/u_{2_{rms}})$ is shown at the positions indicated in the raw PIV image. This measurement set corresponds to the one in Figure 3.11, which was acquired at the first time delay (τ_1).

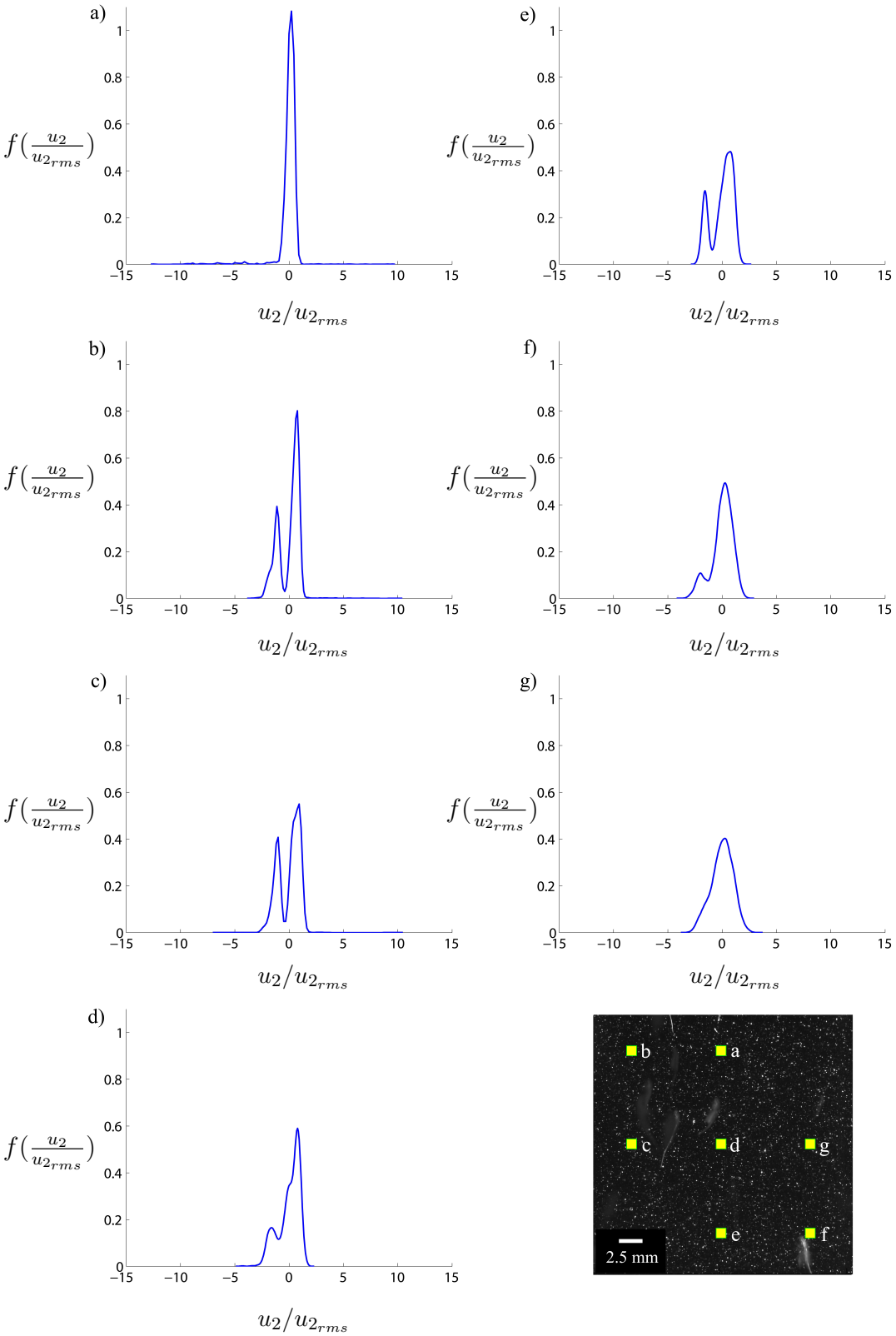

Figure 3.17: PDF of the fluctuating vertical velocity component at the beginning of DVM. The distribution of the normalized velocity $f(u_2/u_{2_{rms}})$ is shown at the positions indicated in the raw PIV image. This measurement set corresponds to the one in Figure 3.12, which was acquired at the second time delay (τ_2).

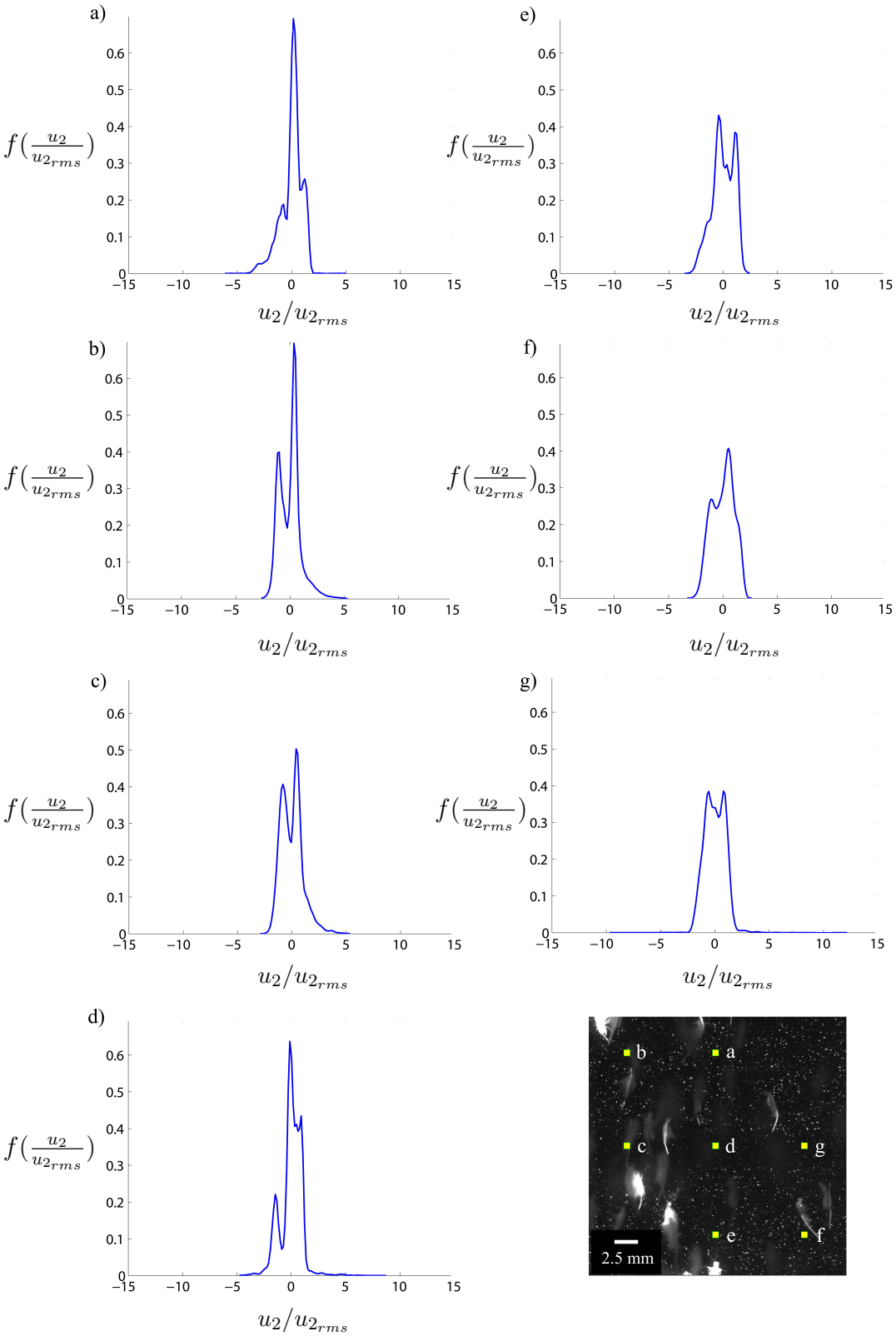

Figure 3.18: PDF of the fluctuating vertical velocity component during DVM. The distribution of the normalized velocity $f(u_2/u_{2_{rms}})$ is shown at the positions indicated in the raw PIV image. This measurement set corresponds to the one in Figure 3.13, which was acquired at the third time delay (τ_3).

3.4 Energy Distribution of the Generated Flow Field

3.4.1 Velocity Spectrum Tensor

Considering the fluctuating components of the velocity field obtained via Reynolds decomposition of the velocity at each measurement node (Equation 3.2), the two-point velocity correlation tensor was computed at every point in the measurement grid according to the following expression, for $|\mathbf{r}|\epsilon[0, 3.9]$ cm:

$$\mathbf{R}_{ij}(\mathbf{r}) \equiv \overline{u_i(\mathbf{x})u_j(\mathbf{x}+\mathbf{r})}\ , \qquad i,j = (1,2)\ \ , \tag{3.5}$$

where the overbar denotes a temporal mean. Thereafter, the spectral velocity tensor $\boldsymbol{\phi}_{ij}$ was computed from the two-point velocity correlation according to:

$$\boldsymbol{\phi}_{ij}(\boldsymbol{\kappa}) = \frac{1}{(2\pi)^3}\iiint_{-\infty}^{\infty} \mathbf{R}_{ij}(\mathbf{r})e^{-i\boldsymbol{\kappa}\mathbf{r}}d\mathbf{r}, \qquad i,j = (1,2)\ \ , \tag{3.6}$$

which was discretized using the 2D Fast Fourier Transform in Matlab within the spatial limits imposed by the field of view and the Nyquist limit (i.e., twice the PIV vector spacing).

Besides being the Fourier transform pair of the velocity correlation, $\boldsymbol{\phi}_{ij}$ provides a complete description of the energy distribution in the flow. In fact, the energy spectrum function ($E(\kappa)$) can be inferred by removing all directional information from $\boldsymbol{\phi}_{ij}$ [76]. Here, the main interest lies in determining the distribution of energy along the vertical direction, given the requirement of generating overturning structures in order to mix fluid within a stable density stratification. Therefore, the vertical component of the spectral velocity tensor $\boldsymbol{\phi}_{22}(\boldsymbol{\kappa})$ was computed from the measured PIV velocity fields for each of the three time delays, i.e., the stages prior to migration (τ_1) as well as the beginning (τ_2) and middle of the migration (τ_3). Refer to §2.4 for details on data acquisition procedures.

As shown in Figure 3.19, as the migration progressed, kinetic energy increased within the entire measurable range of length scales. The evolution of the spectrum with wavenumber for all cases showed that the energy produced by the collective vertical motion of small swimmers is introduced into the flow at scales considerably larger than the body length of a single organism. Moreover, the rate at which energy was transferred among different wavenumbers remained constant following a κ^{-1} power law.

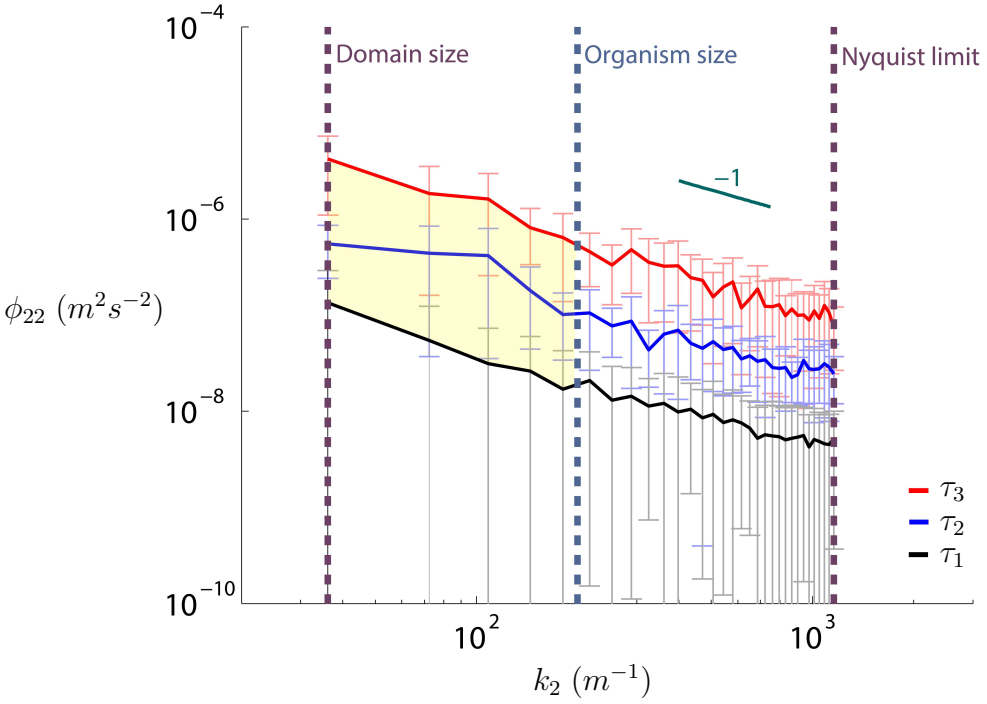

Figure 3.19: Velocity spectrum tensor during vertical migration. The vertical component of the velocity spectrum tensor is shown against vertical wavenumber for the three time delays corresponding to different stages in the migration at which data was acquired. The vertical lines indicate the wavenumbers corresponding to the domain size (i.e., field of view), organism size and the Nyquist limit (i.e., twice the PIV vector spacing). The yellow shaded region indicates increasing kinetic energy at length scales greater than the individual animal size (i.e., wavenumbers smaller than that corresponding to the individual animal size). Only a fraction of the data points were plotted with markers for clarity.

This shape of the kinetic energy spectrum is consistent with the power law observed in shear-dominated flows [71], [34], [64] (see §3.4.2). During vertical migration, kinetic energy is produced at length scales comparable to the organism

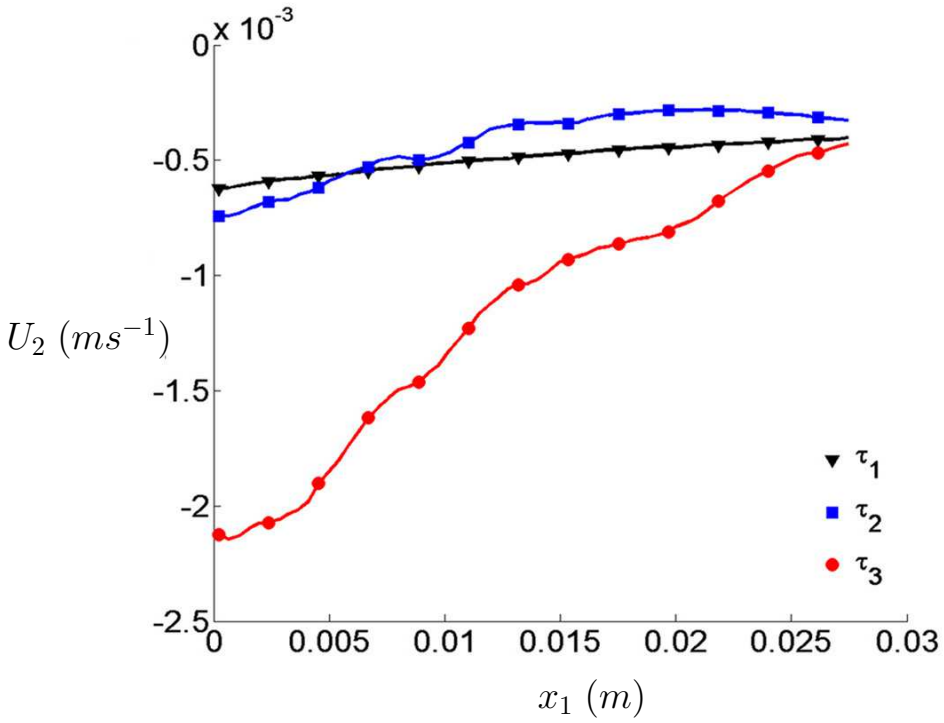

Figure 3.20: Vertical velocity profiles during vertical migration. The mean vertical velocity along a horizontal transect across the center of the field of view is shown for each stage of the migration. The left edge of the field of view matches the central region of the green laser sheet (see Figure 2.3). Only a fraction of the data points were plotted with markers for clarity.

appendages, as individual swimmers propel themselves upward by generating a shearing flow in the direction opposite to their motion. As illustrated in Figure 3.20, the mean velocity was lowest within the central region of the green laser sheet and increased following its spatial distribution, matching the concentration of organisms across the tank. Moreover, as the migration develops, near-field flow interactions among the organisms result in a spatially and temporally growing jet. Spatial gradients of velocity in the region of high shear at the boundary of the jet trigger a Kelvin-Helmholtz instability, which leads to the generation of eddies within the water column that are much larger than the size of individual organisms.

3.4.2 Dimensional Analysis of Observed Spectral Distribution

The kinetic energy distribution presented in §3.4.1 can be modeled via dimensional analysis of the important physical quantities in the observed fluid transport process [64]. A crucial aspect of the flow, briefly introduced in §3.3, is its non-locality: each swimming organism intermittently introduces small scales into the flow through the metachronal stroking of its appendages, which are embedded in a downward jet resulting from the hydrodynamic interactions between neighboring organisms during vertical migration. The overall picture, then, is that of a multi-scale flow in which the dominant interactions occur between these well separated scales, as seen from the bimodal distribution of the fluctuating velocity component u_2 (Figure 3.18). Small scales introduced by the appendage motion of each organism are more influenced by the large-scale advection and shearing imposed by the downward jet than by local interactions between them. In the classical Kolmogorov picture, energetic large-scale structures transfer energy at a constant rate through local interactions, i.e., eddies in the inertial range only interact with coherent structures that are smaller, but of comparable size, to transfer energy down to the dissipative scale. Here, energy is being pumped at a scale much smaller than the integral scale, which is set by the large scale jet dynamics. As a result, local interactions between small scales are negligible compared to the non-local ones that couple large and small scales.

This type of flow, in which the interactions between well-separated scales dominate over local ones, has been previously investigated by Nazarenko et al (see [64], [46]). The proposed hypothesis in these studies is that in non-local turbulent flows, the energy spectrum deviates from the Kolmogorov $\kappa^{-5/3}$ law, observed for isotropic turbulent flows, to a κ^{-1} power law. In two-dimensional turbulence, a κ^{-1} spectrum was theoretically, analytically, and numerically obtained by disregarding local interactions in the vorticity equation of a turbulent flow [64]. Similarly, in three-dimensions, non-locality was numerically studied by filtering the Navier-Stokes equations directly to neglect local interactions [46]. As a result, the recovered turbulent momentum equations are linear in the velocity fluctua-

tion and, more importantly, a flatter energy spectrum was observed, compared to the classical case displaying the $\kappa^{-5/3}$ law, which was independently obtained via DNS. The inability to increase the numerical resolution in the filtered numerical turbulence model has impeded the confirmation of the κ^{-1} power law with this method to date. However, a κ^{-1} dependence is predicted via dimensional analysis for both two-dimensional and three-dimensional non-local turbulent flows [64]. Here, a similar approach is taken in which the local interactions between small turbulent scales are neglected to linearize the Navier-Stokes equations and analyze the non-local turbulent flow on a dimensional basis following the methods of Nazarenko et al [64].

In the turbulent Navier-Stokes equations, local scale interactions arise from the non-linear terms in the equation governing the fluctuating component of the velocity field. This expression can be derived by considering the incompressible form of the momentum equation:

$$\frac{\partial \tilde{u}_i}{\partial t} + \tilde{u}_j \frac{\partial \tilde{u}_i}{\partial x_j} = -\frac{1}{\rho}\frac{\partial \tilde{p}}{\partial x_i} + \nu \frac{\partial^2 \tilde{u}_i}{\partial x_j \partial x_j} + \tilde{f}_i \ , \tag{3.7}$$

where $\tilde{u}_i$ and $\tilde{p}$ denote the instantaneous velocity and pressure of the fluid, and $\tilde{f}_i$ denotes forcing by the organisms. These variables can be simplified into a mean and a fluctuating component:

$$\tilde{u}_i = U_i + u_i \tag{3.8a}$$

$$\tilde{p} = P + p \tag{3.8b}$$

$$\tilde{f}_i = F_i + f_i \ \ . \tag{3.8c}$$

Here, as in the rest of this document, upper case letters denote temporal mean components and lower case letters fluctuations from the mean. Substituting Equations 3.8a, 3.8b, and 3.8c into Equation 3.7 and further averaging (denoted by an overbar) gives the following set of expressions:

Mean-flow equations:

$$\frac{\partial U_i}{\partial t} + U_j \frac{\partial U_i}{\partial x_j} = -\frac{1}{\rho}\frac{\partial P}{\partial x_i} + \nu \frac{\partial^2 U_i}{\partial x_j \partial x_j} - \frac{\partial \overline{u_i u_j}}{\partial x_j} + F_i \tag{3.9a}$$

$$\frac{\partial U_i}{\partial x_i} = 0 \tag{3.9b}$$

Fluctuating component equations:

$$\frac{\partial u_i}{\partial t} + \underbrace{U_j \frac{\partial u_i}{\partial x_j} + u_j \frac{\partial U_i}{\partial x_j}}_{\text{coupling of large and small scales}} + \underbrace{\frac{\partial}{\partial x_j}(u_i u_j - \overline{u_i u_j})}_{\text{non-linear terms}} = -\frac{1}{\rho}\frac{\partial p}{\partial x_i} + \nu \frac{\partial^2 u_i}{\partial x_j \partial x_j} + f_i \tag{3.10a}$$

$$\frac{\partial u_i}{\partial x_i} = 0 \tag{3.10b}$$

Based on the observed non-locality of the flow, the non-linear terms can be neglected in the momentum equation of the fluctuating component of the velocity, i.e., the fourth and fifth terms in the LHS of Equation 3.10a as well as the non-linear terms embedded in the pressure gradient term [46], which is related to the velocity components. This can be seen by taking the divergence of Equation 3.10a and using Equations 3.9b & 3.10b, which gives the Poisson equation for pressure [76]:

$$\frac{\partial}{\partial x_i}\left(\frac{\partial u_i}{\partial t} + U_j \frac{\partial u_i}{\partial x_j} + u_j \frac{\partial U_i}{\partial x_j} + \frac{\partial}{\partial x_j}(u_i u_j - \overline{u_i u_j})\right) = \frac{\partial}{\partial x_i}\left(-\frac{1}{\rho}\frac{\partial p}{\partial x_i} + \nu \frac{\partial^2 u_i}{\partial x_j \partial x_j} + f_i\right)$$

$$\frac{\partial U_j}{\partial x_i}\frac{\partial u_i}{\partial x_j} + \frac{\partial u_j}{\partial x_i}\frac{\partial U_i}{\partial x_j} + \frac{\partial^2}{\partial x_i \partial x_j}(u_i u_j - \overline{u_i u_j}) = -\frac{1}{\rho}\frac{\partial^2 p}{\partial x_i^2} + \frac{\partial f_i}{\partial x_i} \quad . \tag{3.11}$$

This results in:

$$\frac{\partial^2 p}{\partial x_i^2} = -\rho\left(\frac{\partial^2}{\partial x_i \partial x_j}\big(U_j u_i + u_j U_i\big) + \underbrace{\frac{\partial^2}{\partial x_i \partial x_j}(u_i u_j - \overline{u_i u_j})}_{\text{non-linear terms}} - \frac{\partial f_i}{\partial x_i}\right) \quad . \tag{3.12}$$

Therefore, it is evident that Green's solution of the pressure equation will be linear in the velocity fluctuation if the non-linear convective terms are neglected in Equation 3.10a. As a result, the fluctuating component of the turbulent Navier-Stokes equations is linear and, most importantly, the turbulent kinetic energy equation in spectral space is so as well. This can be verified by deriving this expression from the momentum equation for the fluctuating component. For this purpose, each term of Equation 3.10a is transformed into Fourier space below, similarly to what is done in [8].

The Fourier transform of a spatial derivative is defined as [76]:

$$\mathcal{F}\Big\{\frac{\partial g(\mathbf{x})}{\partial x_j}\Big\} = i\kappa_j \hat{g}(\boldsymbol{\kappa}) \ . \tag{3.13}$$

Thus, the terms in the LHS of Equation 3.10 in Fourier space are:

$$\mathcal{F}\Big\{\frac{\partial u_i}{\partial t}\Big\} = \frac{\partial \hat{u}_i}{\partial t} \tag{3.14a}$$

$$\mathcal{F}\Big\{U_j\frac{\partial u_i}{\partial x_j}\Big\} = \mathcal{F}\Big\{U_1\frac{\partial u_i}{\partial x_1} + U_2\frac{\partial u_i}{\partial x_2} + U_3\frac{\partial u_i}{\partial x_3}\Big\} = \mathcal{F}\Big\{U_2\frac{\partial u_i}{\partial x_2}\Big\} = iU_2\kappa_2\hat{u}_i \tag{3.14b}$$

$$\mathcal{F}\Big\{u_j\frac{\partial U_i}{\partial x_j}\Big\} = \hat{G}_i(\boldsymbol{\kappa}, t) \ . \tag{3.14c}$$

In the equations above note that $U_1 << U_2$ and $U_3 << U_2$ (where the subscripts 1, 2, and 3 denote the horizontal, vertical, and out-of-plane directions, respectively). Furthermore, the function $\hat{G}_i(\boldsymbol{\kappa}, t)$ is introduced here to show the Fourier transform of this term, which involves the convolution of the fluctuating velocity and the gradient of the mean flow.

Now, converting the RHS of Equation 3.10a to Fourier space results in:

$$\mathcal{F}\Big\{\frac{1}{\rho}\frac{\partial p}{\partial x_i}\Big\} = \frac{i}{\rho}\kappa_i\hat{p} \tag{3.15a}$$

$$\mathcal{F}\Big\{\nu\frac{\partial^2 u_i}{\partial x_j \partial x_j}\Big\} = -\nu \mid \boldsymbol{\kappa} \mid^2 \hat{u_i} \ , \tag{3.15b}$$

where

$$\mathcal{F}\Big\{\frac{\partial^2}{\partial x_j \partial x_j}\Big\} = (i\kappa_j)^2 = -\kappa_1^2 - \kappa_2^2 - \kappa_3^2 = - \mid \boldsymbol{\kappa} \mid^2$$

$$\mathcal{F}\Big\{f_i\Big\} = \hat{f_i} \ , \tag{3.15c}$$

resulting in the momentum equation in Fourier space:

$$\underbrace{\frac{\partial \hat{u_i}}{\partial t}}_{\text{A}} + \underbrace{i\hat{u_i}\kappa_2 U_2}_{\text{B}} + \underbrace{\hat{G_i}}_{\text{C}} = \underbrace{-\frac{i}{\rho}\kappa_i \hat{p}}_{\text{D}} - \underbrace{\nu \mid \boldsymbol{\kappa} \mid^2 \hat{u_i}}_{\text{E}} + \underbrace{\hat{f_i}}_{\text{F}} \ . \tag{3.16}$$

The spectral form of the turbulent kinetic energy equation can be obtained by multiplying Equation 3.16 by $\hat{u_i}^*$ (complex conjugate of $\hat{u_i}$), taking the real part ($\Re$) and integrating over $\boldsymbol{\kappa}$ to express the kinetic energy in terms of the energy spectrum function defined as [76]:

$$E(\kappa) = \iiint_{-\infty}^{\infty} \frac{1}{2}\phi_{ii}(\boldsymbol{\kappa})\delta(|\boldsymbol{\kappa}| - \kappa)d\boldsymbol{\kappa} \ . \tag{3.17}$$

Doing this term by term gives:

- Term (A):

  Taking $\hat{u_i} = a + bi$:

  $$\Re\left(\hat{u_i}^* \frac{\partial \hat{u_i}}{\partial t}\right) = \Re\left((a - bi)\frac{\partial}{\partial t}(a + bi)\right) = a\frac{\partial a}{\partial t} + b\frac{\partial b}{\partial t}$$

  and

  $$\hat{u_i}^* \frac{\partial \hat{u_i}}{\partial t} + \hat{u_i}\frac{\partial \hat{u_i}^*}{\partial t} = (a-bi)\frac{\partial}{\partial t}(a+bi) + (a+bi)\frac{\partial}{\partial t}(a-bi)) = 2\left(a\frac{\partial a}{\partial t} + b\frac{\partial b}{\partial t}\right) \ .$$

As such,

$$\Re\bigg(\int \hat{u_i}^* \frac{\partial \hat{u_i}}{\partial t} d\boldsymbol{\kappa}\bigg) = \frac{1}{2}\int \bigg(\hat{u_i}^* \frac{\partial \hat{u_i}}{\partial t} + \hat{u_i}\frac{\partial \hat{u_i}^*}{\partial t}\bigg) d\boldsymbol{\kappa} = \frac{1}{2}\frac{\partial}{\partial t}\int \hat{u_i}^* \hat{u_i} d\boldsymbol{\kappa},$$

where we can use the definition of the trace of the velocity spectrum tensor:

$$\boldsymbol{\phi}_{ii} = \mathcal{F}(\boldsymbol{R}_{ii}) = \mathcal{F}(u_i u_i)$$

to give:

$$\frac{1}{2}\frac{\partial}{\partial t}\int \hat{u_i}^* \hat{u_i} d\boldsymbol{\kappa} = \frac{1}{2}\frac{\partial}{\partial t}\int \boldsymbol{\phi}_{ii}\delta(|\boldsymbol{\kappa}| - \kappa) d\boldsymbol{\kappa} \ \ ,$$

where the Dirac delta function is taken to integrate over $\boldsymbol{\kappa}$ [76]. Moreover, assuming that $\boldsymbol{\phi}_{22} >> \boldsymbol{\phi}_{11}$ and $\boldsymbol{\phi}_{22} >> \boldsymbol{\phi}_{33}$, then:

$$\frac{1}{2}\frac{\partial}{\partial t}\int \boldsymbol{\phi}_{ii}\delta(|\boldsymbol{\kappa}| - \kappa) d\boldsymbol{\kappa} = \frac{\partial E(\kappa_2, t)}{\partial t} \tag{3.18}$$

- Term (B):

$$\Re\bigg(\int iU_2\kappa_2 \hat{u_i}\hat{u_i}^* d\boldsymbol{\kappa}\bigg) = 0 \tag{3.19}$$

- Term (C):

$$\Re\bigg(\int \hat{u_i}^* \hat{G_i} d\boldsymbol{\kappa}\bigg) \tag{3.20}$$

- Term (D):

$$\Re\bigg(\int -i\rho^{-1}\kappa_i \hat{u_i}^* \hat{p} d\boldsymbol{\kappa}\bigg) \tag{3.21}$$

- Term (E):

$$\begin{gathered}\Re\bigg(\int -\nu \mid \boldsymbol{\kappa} \mid^2 \hat{u_i}\hat{u_i}^* d\boldsymbol{\kappa}\bigg) = -2\nu \mid \boldsymbol{\kappa} \mid^2 \int \tfrac{1}{2}\hat{u_i}^* \hat{u_i} d\boldsymbol{\kappa} = \\ -2\nu \mid \boldsymbol{\kappa} \mid^2 \tfrac{1}{2}\int \boldsymbol{\phi}_{ii}\delta(|\boldsymbol{\kappa}| - \kappa) d\boldsymbol{\kappa} = -2\nu \mid \boldsymbol{\kappa} \mid^2 E(\kappa_2, t) \ \ ,\end{gathered} \tag{3.22}$$

assuming that $\boldsymbol{\phi}_{22} >> \boldsymbol{\phi}_{11}$ and $\boldsymbol{\phi}_{22} >> \boldsymbol{\phi}_{33}$.

- Term (F):

$$\Re\Big(\int \hat{u_i}^* \hat{f}_i d\boldsymbol{\kappa}\Big) \tag{3.23}$$

Therefore, the turbulent kinetic energy in spectral form is:

$$\frac{\partial E(\kappa_2,t)}{\partial t}+\Re\Big(\int \hat{u_i}^* \hat{G}_i d\boldsymbol{\kappa}\Big) = -\Re\Big(\int i\rho^{-1}\kappa_i \hat{u_i}^* \hat{p} d\boldsymbol{\kappa}\Big) - 2\nu \mid \boldsymbol{\kappa} \mid^2 E(\kappa_2,t) + \Re\Big(\int \hat{u_i}^* \hat{f}_i d\boldsymbol{\kappa}\Big)$$

or:

$$\frac{\partial E(\kappa_2,t)}{\partial t} + 2\nu \mid \boldsymbol{\kappa} \mid^2 E(\kappa_2,t) = \Re\Big(-\int \Big(\hat{u_i}^* \hat{G}_i + i\rho^{-1}\kappa_i \hat{u_i}^* \hat{p} - \hat{u_i}^* \hat{f}_i\Big) d\boldsymbol{\kappa}\Big), \tag{3.24}$$

where the turbulent kinetic energy dissipation rate is defined as [76]:

$$\frac{\partial \varepsilon}{\partial \kappa_2} = 2\nu \mid \boldsymbol{\kappa} \mid^2 E(\kappa_2,t) \ .$$

Now, given that the nonlinearities in the momentum equation have been neglected, the derived spectral energy equation is linear in $E(\kappa_2,t)$ (see Equation 3.24). Therefore, its solution will form a linear space [16]. Accordingly, the relation between E and ε, which is defined as the spectral flux of the energy spectrum, has to be linear given the nature of the governing equations of motion [64]:

$$E \propto \varepsilon \ . \tag{3.25}$$

Considering the physical quantities that determine the energy spectrum and their dimensions, the spectral decay may be estimated [64]:

Quantity	Dimensions	Units
Energy spectrum $E(\kappa_2,t)$	EL	L^3T^{-2}
Energy flux ε	ET^{-1}	L^2T^{-3}
Strain rate α	UL^{-1}	T^{-1}
Wavenumber κ_2	L^{-1}	L^{-1}

This results in:

$$\underbrace{E}_{[L^3T^{-2}]} \propto \underbrace{\frac{\varepsilon}{\alpha}}_{[L^2T^{-2}]} \underbrace{\kappa_2^{-1}}_{[L]} \quad . \tag{3.26}$$

As hypothesized by Laval et al [64], this scaling of the kinetic energy spectrum has been observed in three-dimensional turbulent flows subjected to shear, such as in the atmospheric turbulent boundary layer and in near-wall turbulent flows ([10] and [71], respectively). The interaction of large and small scales in these cases becomes non-negligible as opposed to what occurs in isotropic turbulent flows, due to the presence of a mean strain rate [96], [28].

Further evidence of the occurrence of the κ^{-1} regime is more commonly reported regarding scalar transport in turbulent flows. This power law occurs in what is known as the Batchelor regime and has also been directly attributed to the non-locality of the flow in recent investigations (see [82], for example). This scaling was theoretically derived by Batchelor for the specific scenario of passive scalar spectra [5]. Although its universality has not been confirmed, it has been experimentally observed that for high Schmidt numbers, the measured spectrum follows a κ^{-1} dependence as theoretically predicted [102]. In this case non-locality arises from the fact that momentum diffuses at scales larger than that of the scalar, and hence the interactions between these well-separated scales dominate the dynamics at high wavenumbers [64]. Recent investigations in this field have shown the transition from local scalar mixing, characterized by a -5/3 spectrum, to a non-local one, showing a -1 slope instead, via numerical simulations [72], [82].

From a mathematical standpoint, different models have been proposed on the basis of dynamical systems theory to understand the transition from a steady state to chaos [92], [53]. One of these scenarios, developed by Pomeau and Manneville, displays a transition to turbulence via the random appearance of intermittent high-intensity bursts in an otherwise laminar signal [55], [75]. Moreover, this specific

dissipative dynamical system (describing a temporal signal measured at a specific location in the flow) is observed to exhibit a $1/f$ spectrum (f denotes frequency), which has been theoretically associated with non-local flows [89]. Experimental observation of a so-called Pomeau-Manneville scenario has been achieved in Rayleigh-Benard convection and qualitatively in open flows as well (see [6] and [85], for example). Although its physical interpretation and applicability with respect to turbulent flows is not trivial, it supports the connection between the power law observed here and intermittency, which has been argued to be a result of non-local effects in turbulent flows [23], [46].

3.5 Large-field Flow Visualizations: Observation of Large-scale Coherent Structures

Qualitative flow visualizations of a larger field of view than that used for PIV at the same vertical position confirmed the formation of eddies next to the downward jet, which is consistent with the onset of a Kelvin-Helmholtz instability (Figure 3.21). Furthermore, this observation matches a linear stability analysis of the flow, which predicts that the length scale of the generated flow structures is at least an order of magnitude greater than the body size of a single organism.

As observed in Figure 3.21, the destabilizing effect of shear in the outer region of the downward jet triggers a Kelvin-Helmholtz instability during vertical animal migration. In the set of experiments presented in this chapter, the resulting vortex sheet is always unstable to waves of all lengths due to the homogeneity of the fluid [40].

It has been shown that linear stability analysis yields a good description of the initial development of shear layers such as those occurring in jets [30]. For this purpose, the shear flow generated by an unsteady jet may be considered as the result of the interaction of unstable waves. Knowledge of the shear layer shape, quantified by the momentum thickness, provides insight into the length scale of the eddies that form via the Kelvin-Helmholtz instability. The dimensionless Strouhal

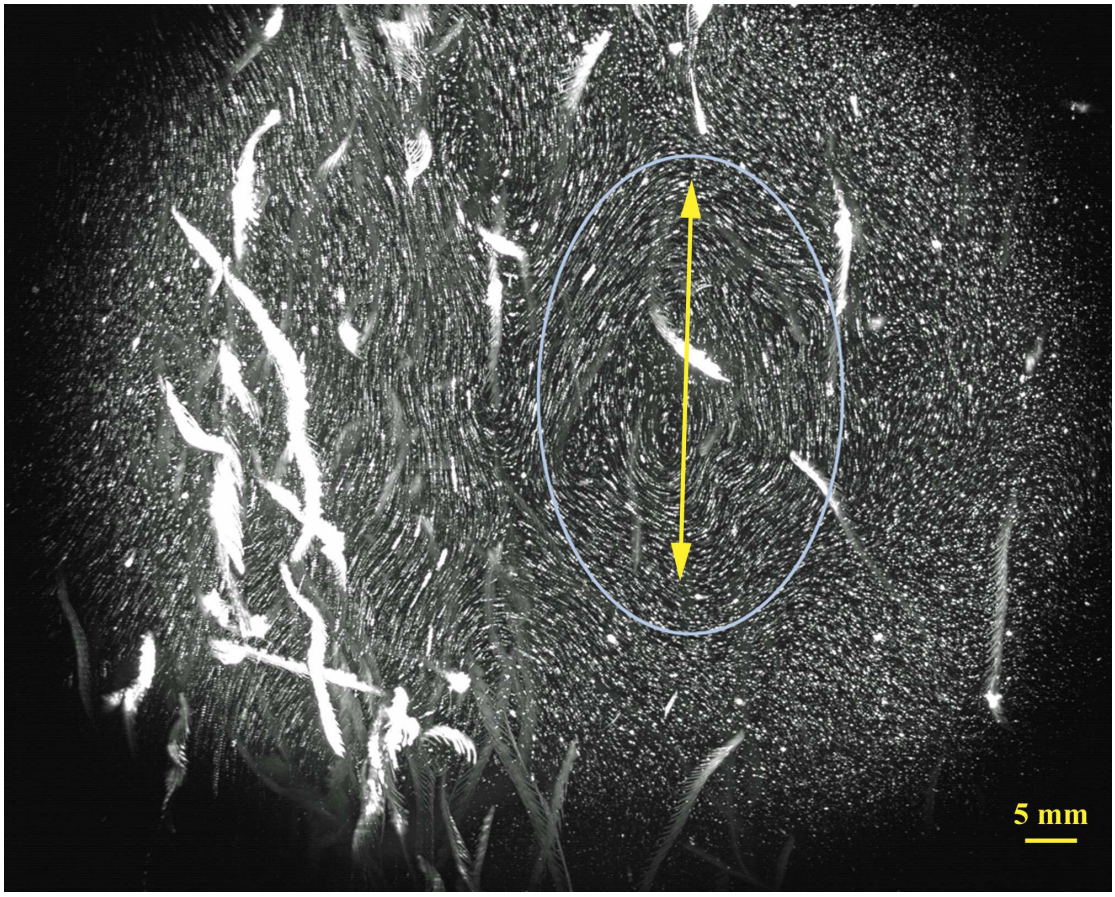

Figure 3.21: Large-field flow visualization of a vertical migration in non-stratified fluid. This image shows the pathlines of PIV particles seeded in the water as well as the swimming organisms. The depicted particle and animal streaks are the result of overlaying a 30-second sequence of raw PIV images recorded during the middle of a vertical migration. The generated large-scale flow structures next to the downward jet (e.g., blue oval) are significantly larger than the individual organisms. The vignetting of the image is due to the narrow-band laser filter on the camera, which becomes apparent when zoomed out to capture the larger-scale flow structures.

number of the most unstable jet mode is given by $St_n = f_n U^{-1} \theta_0 = 0.032$ [30], where f_n is the natural frequency of the unstable mode, U is the mean velocity in the shear layer, and θ_0 is the momentum thickness of the shear layer defined as [40]:

$$\theta_0 = \int_0^\infty \frac{\tilde{u}}{U_0}\left(1 - \frac{\tilde{u}}{U_0}\right) dx \quad , \tag{3.27}$$

where U_0 denotes the free stream velocity. The measured momentum thickness in the jet formed during vertical migration was $\theta_0 \approx 5$ mm. Therefore, the predicted length scale of eddies formed due to the associated Kelvin-Helmholtz instability

is $Uf_n^{-1} \approx (10^{-1})$ m, which is significantly larger than the individual animal size (≈ 5 mm).

3.6 Discussion

In this chapter, animal-fluid interactions during vertical migration were investigated for individual swimmers as well as for aggregations of *A. salina*. The premise that Darwinian drift is dependent upon organism swimming mode was confirmed. It was found that, during metachronal swimming, this fluid transport mechanism is repressed and hydrodynamic trails larger than the size of a single organism are formed in lieu. Nonetheless, these observations prove that the near-field flow of a self-propelled swimmer is a crucial factor regarding fluid transport. Our measurements also demonstrate that inertial effects are non-negligible during DVM of self-propelled zooplankton, which highlights the need to deviate from analysis based on solutions to the Stokes equations to correctly model this process.

Time-resolved PIV measurements during vertical migration of an aggregation demonstrated that hydrodynamic interactions between neighboring organisms enhance fluid transport. Large-scale propagation of a downward jet behind each organism inevitably interacts with the flow field due to a neighboring swimmer and, as a result, a spatially and temporally diverging downward jet develops within the region in which animals migrate upwards. This large-scale fluid transport process is related to the non-uniform animal concentration in the water column, which is imposed by the finite width of the green laser sheet in the laboratory apparatus (refer to Chapter 2). However, this is consistent with the DVM process as it occurs in the ocean, wherein aggregations of zooplankton are also found to form non-uniform patches as seen in photographic data as well as in recent glider measurements [27], [25].

The far-field fluid dynamical scenario due to DVM is characterized by non-local interactions between well-separated scales that enhance the formation of large scale structures, which in turn introduce intermittency in the flow. Furthermore, it

was found that the corresponding distribution of kinetic energy with wavenumber follows a spectral decay of κ^{-1}, which agrees with this description. By neglecting nonlinearities in the equations of motion, which represent local interactions between fluid structures, this power law can be explained via dimensional analysis involving the strain rate, the kinetic energy dissipation flux, and the wavenumber. Moreover, the shape of the velocity spectrum exhibits an increase of energy over all measurable length scales including, most importantly, length scales larger than the size of an individual organism. Large-field flow visualizations presented at the end of this chapter indeed show the formation of large-scale eddies adjacent to the developed jet. The destabilizing effect of shear introduced by the collective effects during vertical migration trigger a Kelvin-Helmholtz instability, which was described via linear stability analysis of the most unstable mode.

The results compiled in this chapter demonstrate the existence of an inverse cascade through which kinetic energy is introduced into the flow at the scale of individual swimmers and is subsequently transferred—via the collective formation of intermittent jets that are Kelvin-Helmholtz unstable—to larger scales at which mixing can potentially occur efficiently. Additional experimental studies of vertical animal migration in a stably stratified fluid are presented in the next chapter with the aim to investigate the evolution of the observed Kelvin-Helmholtz instability in the presence of restoring buoyancy effects. We hypothesize that the evolution of Kelvin-Helmholtz instabilities at the boundaries of the intermittent jets within a DVM could trigger Rayleigh-Taylor instabilities across surfaces of constant density and the formation of internal waves along those surfaces. Both processes could potentially result in large mixing eddies, which may explain findings of density overturns after krill migration in the ocean described at the beginning of this chapter [43]. Moreover, the presence of this additional mode could imply an increase of the estimated limit of the mixing efficiency from the commonly reported 0.2 for shear instabilities parallel to iso-density surfaces up to 0.75, which has been measured for mixing by Rayleigh-Taylor unstable flows within stable density stratifications [48].

Chapter 4

The Role of Stratification on Fluid Transport During Vertical Collective Motion

4.1 Introduction

In Chapter 3, it was demonstrated that animal-fluid interactions during vertical collective motion does result in energetic large-scale fluid structures, regardless of the small size of the self-propelled organisms conforming the migrating aggregation. It was observed that the development of a jet propagating opposite to animal motion was the dominant fluid transport mechanism during DVM. The destabilizing effect of shear in the homogeneous fluid column set off the subsequent roll up of fluid via the development of a Kelvin-Helmholtz instability. As discussed in §3.6, this could have important implications regarding fluid transport and vertical mixing in the presence of stratification; namely, it could provide a means to generate overturns that could potentially mix fluid across isopycnals, i.e., iso-density surfaces, in an efficient manner.

Having verified that large-scale fluid transport indeed results from collective hydrodynamic interactions during DVM, the effect of a stable density stratification on the observed fluid transport process will be addressed in this chapter. The main question is whether the restoring effect of buoyancy will dampen the development of individual hydrodynamic trails, thus stabilizing the flow field, or if the orientation of the shear layer with respect to the stable stratification will result in a hydrodynamic instability such as Rayleigh-Taylor, for example.

For this purpose, additional instrumentation was implemented into the experimental apparatus to thermally stratify the water tank (refer to §2.3). At the beginning of this chapter, the measured density profile is presented and characterized in terms of its stability (§4.2). Similar to the experimental sets analyzed in Chapter 3, time-resolved PIV measurements were acquired during vertical migration in the presence of a stable thermal stratification. The development of fluid transport features during vertical migration is presented in §4.3 and compared to the observed far-field signature of migrating aggregations in homogeneous fluid. The energy distribution among the resolved range of length scales and an analysis of the estimated spectral decay is given in §4.3.2. Finally, an energy balance approach to estimate the efficiency of this biogenic process is detailed in §4.4, followed by a brief discussion in §4.5.

4.2 Characterization of the Density Profile

The most important feature regarding vertical energy and nutrient transport in the ocean is its stable density stratification. The parameter used to characterize the strength of the ocean stratification is the buoyancy frequency, defined in §1.3.1 as:

$$N = \sqrt{-\frac{g}{\rho_0}\frac{d\rho}{dz}} \quad , \tag{4.1}$$

where, ρ_0 is a constant reference density [93]. From this expression, it is evident that only stable stratifications ($\frac{d\rho}{dz} < 0$) result in real values of N. Furthermore, based on Newton's second law, the buoyancy frequency determines the highest frequency at which a fluid parcel will oscillate if advected from its stable position. Hence, weak stratifications are characterized by low values of N, whereas strong stratifications result in higher values. In the ocean, the buoyancy frequency is typically found to be $N = 10^{-2}$ s^{-1} within the pycnocline and it can reach up to $N = 10^{-4}$ s^{-1} in the deep ocean [93].

In order to simulate oceanic conditions, a stable density stratification was set up by gradually heating the water column from top to bottom as detailed in §2.4. The main challenge with matching the strength of the stratification in the experimental apparatus with the one that organisms undergoing DVM encounter in the ocean is imposed by the height of the test tank. From Equation 4.2, it is evident that to acquire a buoyancy frequency of $N = 10^{-2}$ s^{-1}, the difference in density from top to bottom of the water column ($\Delta\rho$) is restricted to be:

$$\Delta\rho = -\frac{\rho_0}{g} N^2 H \approx -10^{-2} H \frac{kg}{m^3} \quad ,$$

where H is the height of the test tank (1.2 m). For a thermally stratified water column with this dimensions, this translates into a temperature difference of $\Delta T = 0.05$ ℃, which is not feasible with the present laboratory methodologies.

Setting the minimum limit on the temperature difference from the top to bottom of the water tank to be $\Delta T = 5$ ℃ results in a density difference of $|\Delta\rho| \approx 1$ kgm^{-3} and a buoyancy frequency of $N = 10^{-1}$ s^{-1}. Thus, experimental results acquired with this configuration provide information on the limit case of a strong stratification. Measurements of the resulting density gradient and buoyancy frequency are shown in Figures 4.1 and 4.2, respectively, for each experimental test.

4.3 Jet Development and Energy Distribution: Comparison with the Non-stratified Case

This section complements the results presented in Chapter 3. By maintaining the same experimental conditions, the effect of a stable density stratification on biogenic fluid transport and mixing via DVM was directly investigated. The immediate consequence of investigating fluid transport and mixing via DVM within a strong stratification is that vertical dispersion is dramatically restricted compared to vertical transport within the pycnocline. We hypothesize that the hydrody-

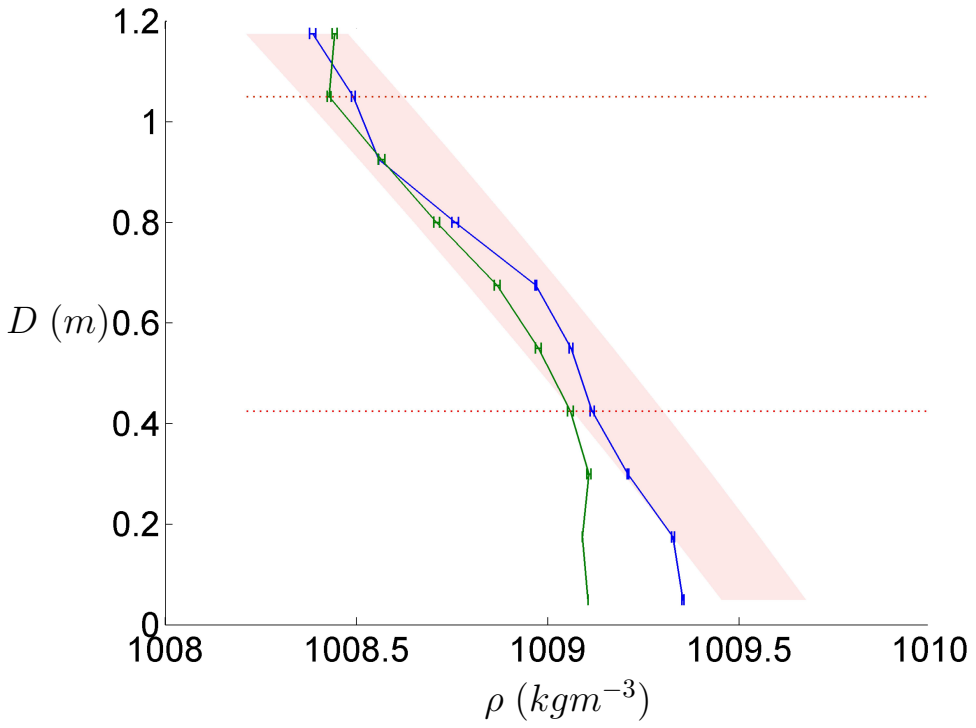

Figure 4.1: Density profile prior to vertical migration. The temporal mean of the density profile acquired every 3 s during $\sim$ 2.5 minutes prior to animal migration is shown for each experimental test (lines blue and green). The horizontal error bar denotes the standard deviation of this measurement at the vertical position of each sensor, which is denoted by D (the distance from the bottom of the tank). The red shaded region indicates the idealized case of a perfectly linear density profile, taking into account sensor measurement accuracy ($\pm$0.5 ℃). The PIV measurement field of view was located in between the dotted lines, at about 0.6 m from the bottom of the column.

namic features observed in this setting can be considered a lower bound with respect to ocean conditions. As mentioned in §2.4.2, two experimental sets were acquired. Each set consisted of one PIV measurement prior to vertical migration, i.e., at the first time delay ($\tau_1 = 0$ s), and one PIV measurement at the middle of the migration, i.e., at the third time delay ($\tau_3 = 67$ s).

4.3.1 Observed Hydrodynamic Features

Raw PIV images were post-processed as described in §3.2. Contrary to previous numerical studies [4], the Reynolds number was found to be the same as for DVM in a non-stratified fluid ($Re = 50$), given that the swimming speed of the organisms remained constant. Furthermore, similar to the non-stratified case, it was observed that each swimmer generated a jet that propagated in the opposite

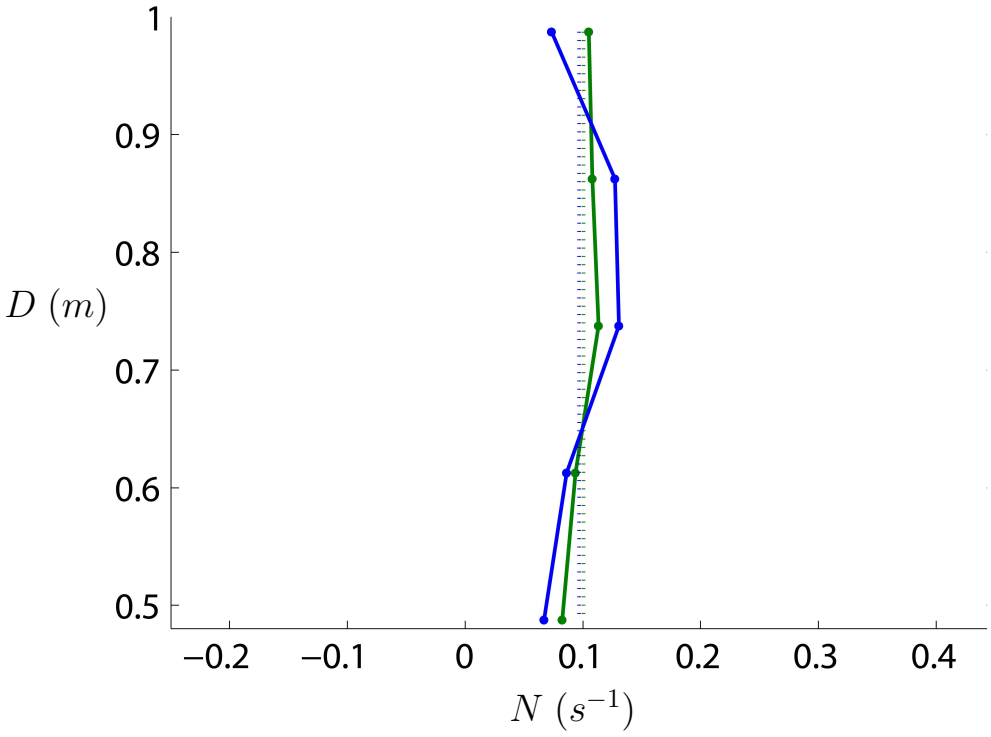

Figure 4.2: Buoyancy frequency of the thermal stratification. The buoyancy frequency in between the dotted lines in Figure 4.1 is shown for each experimental test (lines blue and green). The broken lines correspond to the mean value of each test (also in blue and green).

direction to its motion, which counteracted and dominated the weak upward drift within its dorsal side (Figure 4.3). As anticipated, the density stratification imposed by the linear thermal gradient greatly restricted vertical fluid motion. As a result, the vertical extent of the hydrodynamic trails behind migrating organisms was reduced considerably compared to those observed in non-stratified fluid. Nonetheless, the size of the jet was still noticeably greater than the body length of a single organism.

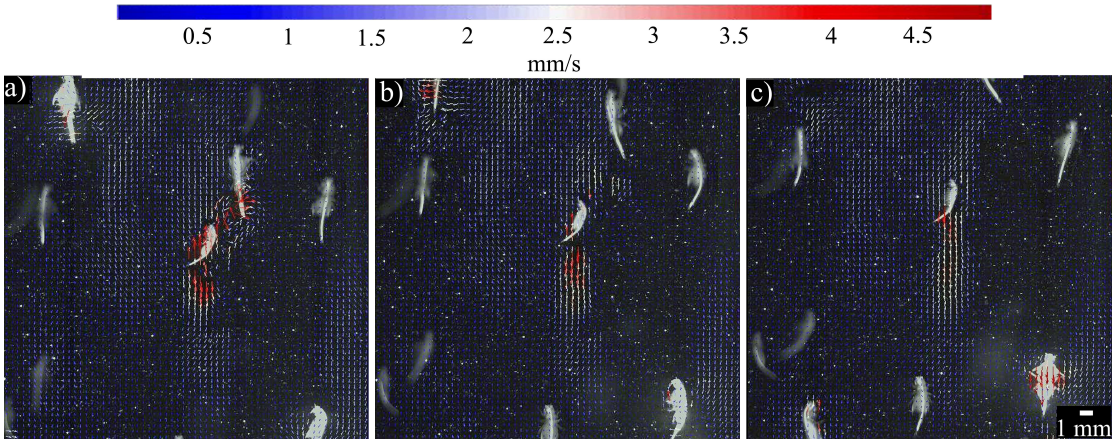

Figure 4.3: Hydrodynamic trail development behind a single organism during DVM in stratified fluid. The presented time series (a - c) was acquired 83 s after the migration had been triggered ($\tau_3 + 16$ s). Images are shown with a time lapse of $\Delta t = 252$ ms.

As the migration progressed in time, the hydrodynamic interactions between adjacent swimmers also resulted in net downward fluid motion (Figure 4.4). However, spatial and temporal growth of the jet was less pronounced, compared to a non-stratified fluid environment.

Further analysis of the velocity time series via Reynolds decomposition of the velocity at each PIV measurement node confirmed the non-local behavior of the flow. As shown in Figure 4.6, the PDF of the vertical fluctuating velocity u_2 at the center of the measurement domain displayed a multi-modal distribution with long tails, characterized by a kurtosis larger than that of a normal Gaussian distribution ($\gamma_2 = 18$ in the PDF in Figure 4.6). This behavior was also observed at other PIV grid positions, in which at least two modes were recognizable from the PDF. As in the non-stratified case, the extended tails in the distribution confirmed the intermittent nature of the flow. This property was also evident in the temporal evolution of the fluctuating velocity, in which high intensity bursts randomly appeared within all positions of the measurement grid (Figure 4.8).

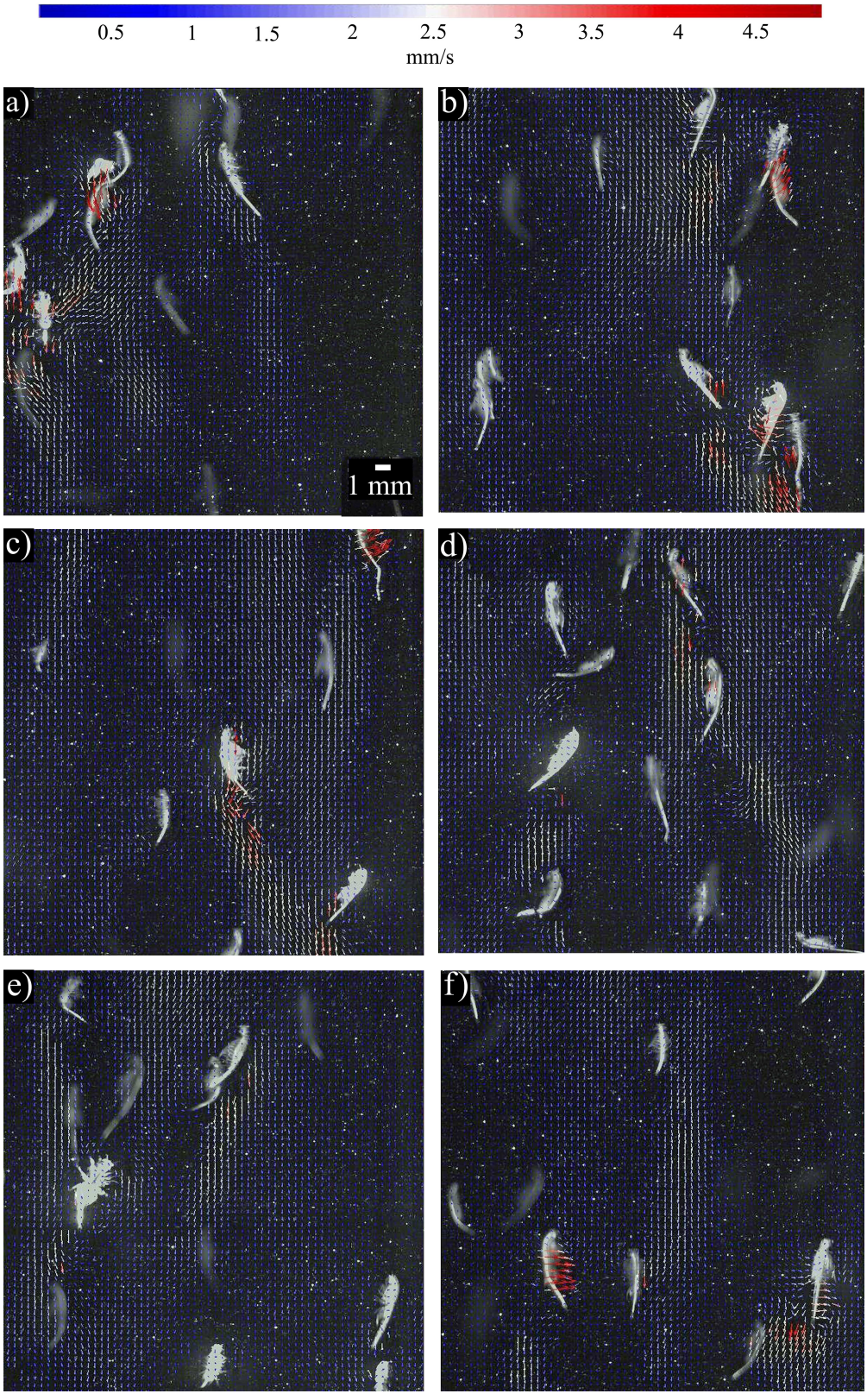

Figure 4.4: Velocity field measurements during vertical migration in stratified fluid. Time series of a representative set acquired with the third time delay ($\tau_3 =$ 67 s), which corresponds to the middle of the migration. The flow field is shown for the following times: $t = \tau_3 + 2.8$ s (a), $t = \tau_3 + 5.6$ s (b), $t = \tau_3 + 8.4$ s (c), $t = \tau_3 + 11.2$ s (d), $t = \tau_3 + 14$ s (e), $t = \tau_3 + 16.8$ s (f).

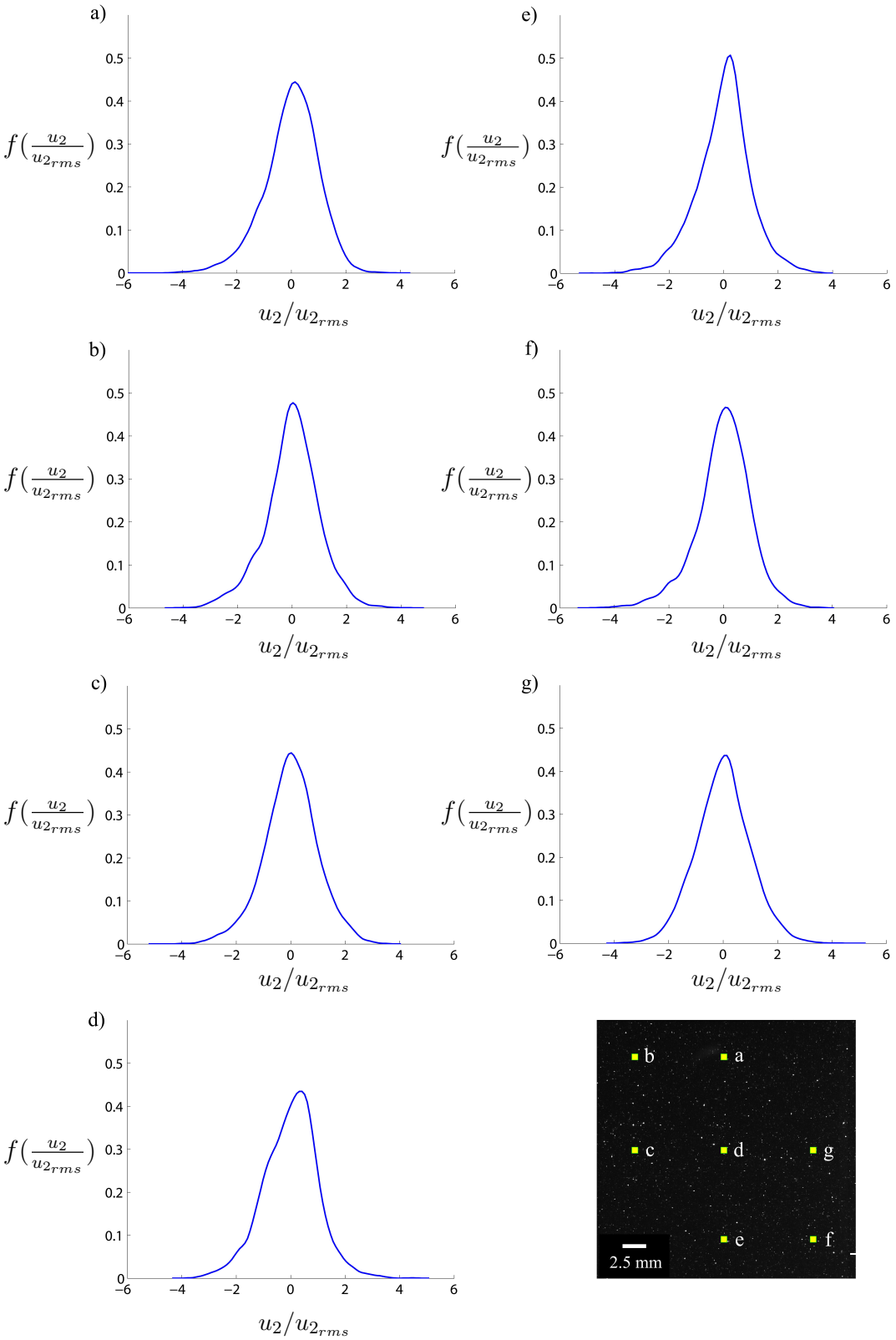

Figure 4.5: PDF of the fluctuating vertical velocity component prior to DVM in stratified fluid. The distribution of the normalized velocity $f(u_2/u_{2_{rms}})$ is shown at the positions indicated in the raw PIV image. This measurement set corresponds to the one in Figure 4.7, which was acquired at the first time delay (τ_1).

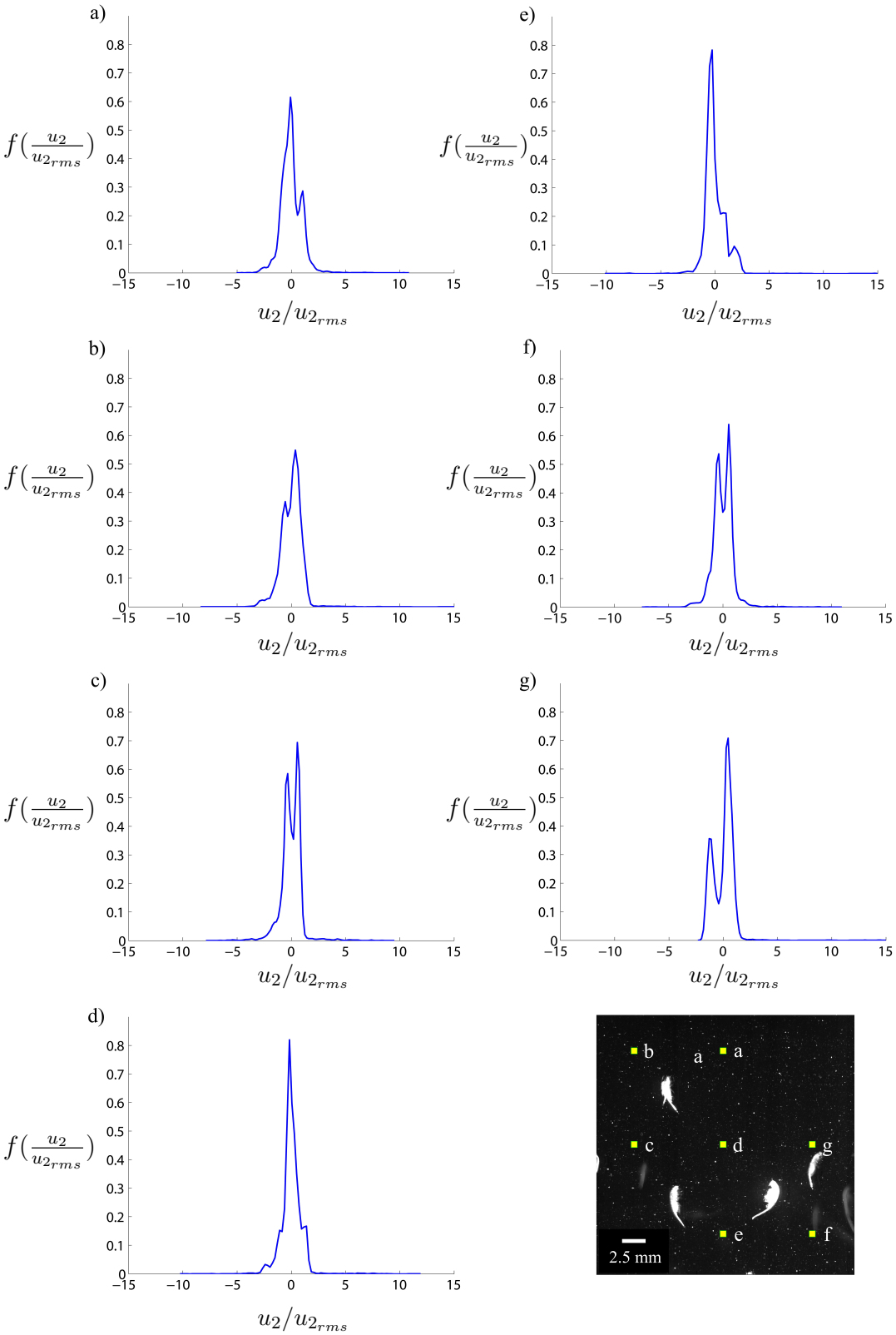

Figure 4.6: PDF of the fluctuating vertical velocity component during DVM in stratified fluid. The distribution of the normalized velocity $f(u_2/u_{2_{rms}})$ is shown at the positions indicated in the raw PIV image. This measurement set corresponds to the one in Figure 4.8, which was acquired at the third time delay (τ_3).

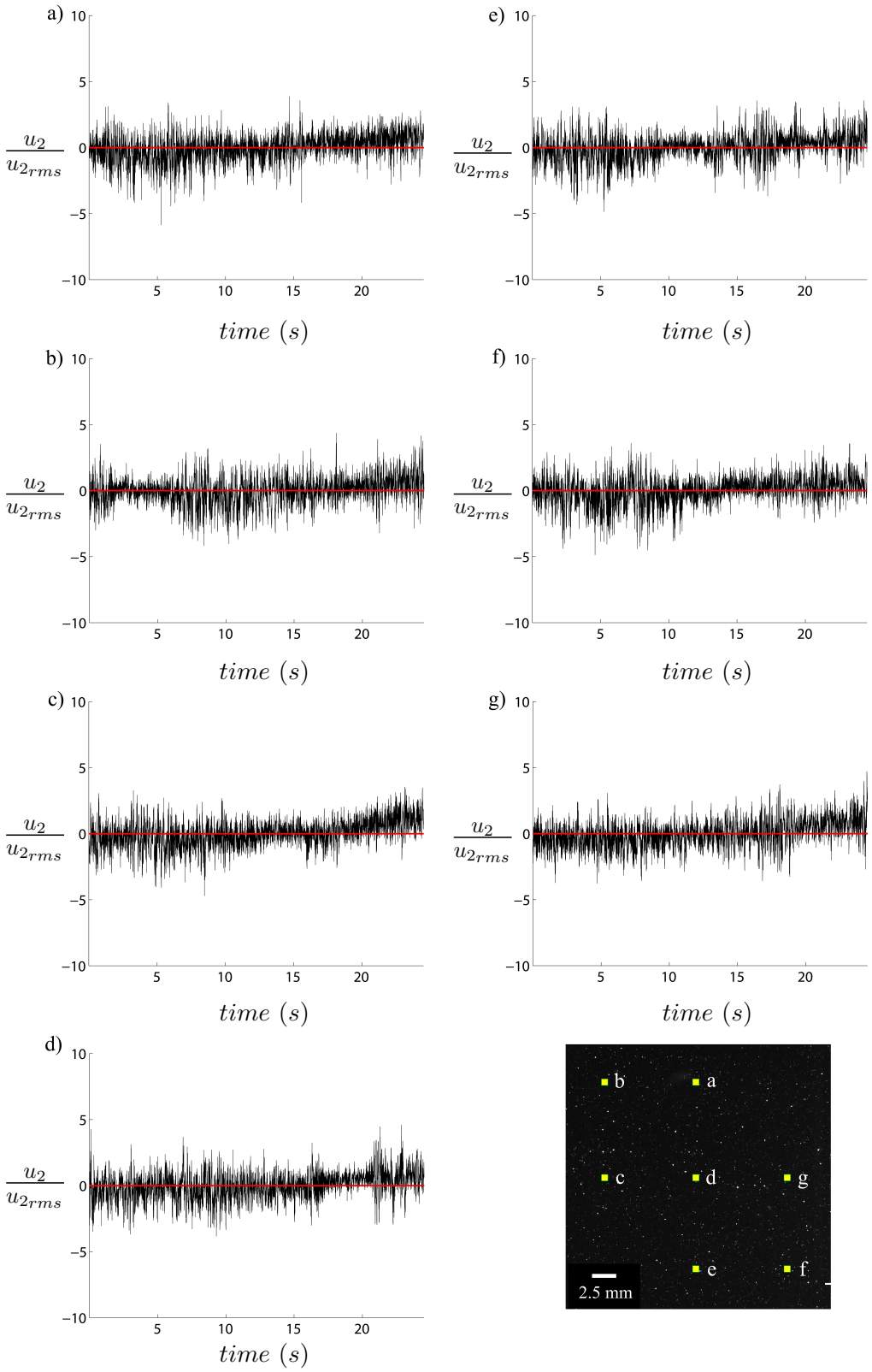

Figure 4.7: Time series of the vertical velocity component prior to DVM in stratified fluid. The magnitude of u_2 is shown normalized by $u_{2_{rms}}$ at the positions indicated in the raw PIV image. These measurements are a representative set of data acquired prior to vertical migration at the first time delay (τ_1).

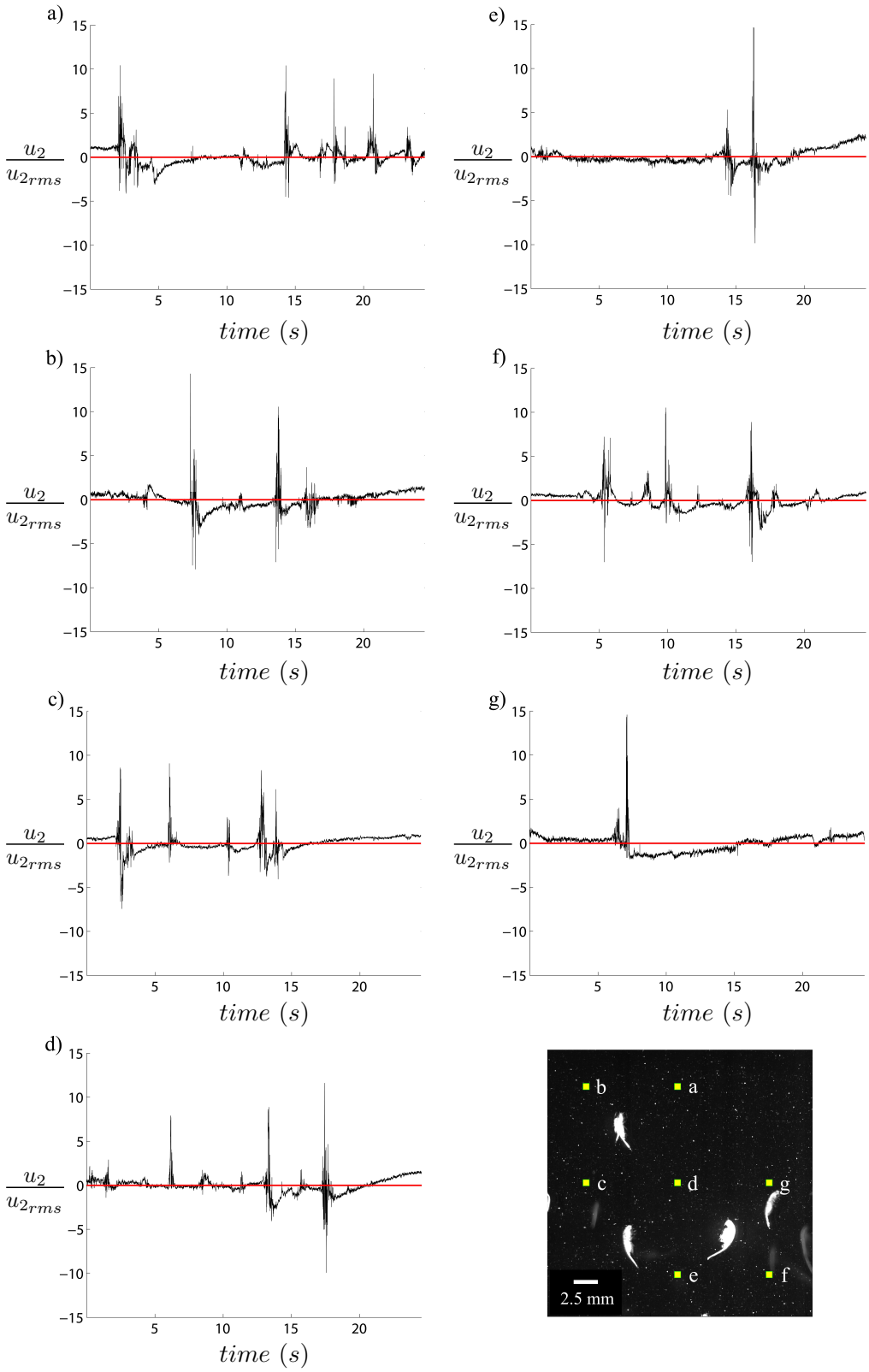

Figure 4.8: Time series of the vertical velocity component during DVM in stratified fluid. The magnitude of u_2 is shown normalized by $u_{2_{rms}}$ at the positions indicated in the raw PIV image. These measurements are a representative set of data acquired during vertical migration at the third time delay (τ_3).

4.3.2 Velocity Spectrum Tensor

As shown in Figure 4.9, the stabilizing effect of stratification completely annihilated the far-field flow signature of the organisms as they gathered at the bottom of the water tank prior to the onset of the migration, which corresponds to measurements acquired at $t = \tau_1$. The mean vertical velocity at a horizontal transect at mid-height of the water column was practically zero, whereas a weak downward flow was measured in experiments done in a homogeneous fluid at the same time delay. Similarly, the velocity profile during vertical migration displayed a decrease in downward velocity values, compared to those reached in a non-stratified water column. Thus, buoyancy forces acted as an additional sink to kinetic energy arising from vertical fluid motion.

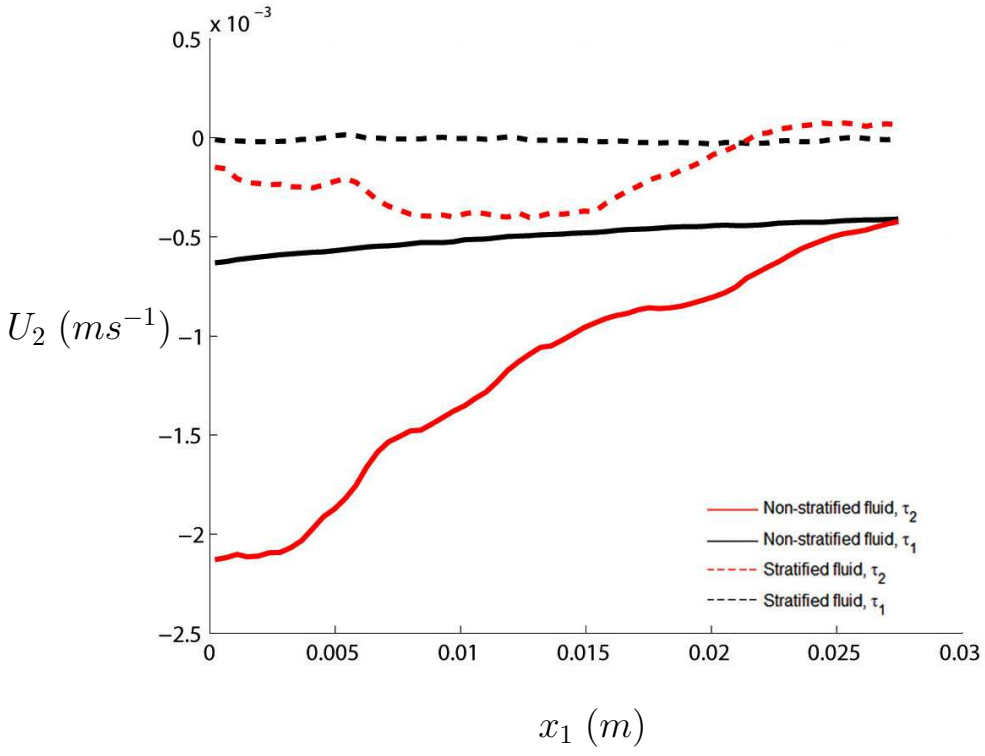

Figure 4.9: Vertical velocity profiles during vertical migration. Mean vertical velocity along a horizontal transect across the center of the field of view is shown for experiments in non-stratified (solid lines) and stratified (broken lines) fluids for two stages of the migration: τ_1 (black lines), which captures the flow conditions in the tank prior to vertical migration, and τ_2 (red lines), which corresponds to the middle of the migration.

In agreement with the observed velocity profile, the vertical component of the

velocity spectrum tensor, computed as indicated in §3.4, showed a lower energy level than that obtained in a non-stratified fluid (Figure 4.10). In fact, the energy distribution corresponding to $t = \tau_1$ was within the accuracy limit for PIV measurements [2]. Therefore, only the velocity spectrum tensor corresponding to $t = \tau_3$ was considered in the calculation of the mixing efficiency in §4.4.2. Nonetheless, energy was still introduced at scales larger than the size of an individual swimmer, which suggests that the strength of the stratification was not sufficient to impede the onset of shear-induced hydrodynamic instabilities.

As described in §4.3.1, the PDF of the fluctuating velocity measured during vertical migration in a stratified fluid displayed the presence of at least two different modes in the flow, similarly to experiments done in homogeneous fluid. Congruent with this result, the velocity spectrum corresponding to measurements done in a stable stratification follows a κ^{-1} power law, indicating that the evolution of a multi-scale flow was not annihilated by the stabilizing effect of buoyancy. Therefore, the interplay between the small scales introduced by the appendage motion of each swimmer and the large-scale advection imposed by the downward jet dominates the dynamics.

4.3.3 Dimensional Analysis of the Observed Spectral Distribution

The power law that the vertical component of the velocity spectrum displays under stratified conditions can be explained on the same basis as was done in the non-stratified case. Due to the small change in density across the water tank, density fluctuations during vertical migration are such that $\mid \rho \mid << \rho_0$, where ρ_0 is a constant reference density taken to be the density at the top of the water column. As a result, the Navier-Stokes equations can be written under the Boussinesq approximation [51]:

$$\frac{\partial \tilde{u}_i}{\partial t} + \tilde{u}_j \frac{\partial \tilde{u}_i}{\partial x_j} = -\frac{1}{\rho_0}\frac{\partial \tilde{p}}{\partial x_i} + \nu \frac{\partial^2 \tilde{u}_i}{\partial x_j \partial x_j} - \frac{\tilde{\rho}}{\rho_0} g \delta_{i2} + \tilde{f}_i \ , \tag{4.2}$$

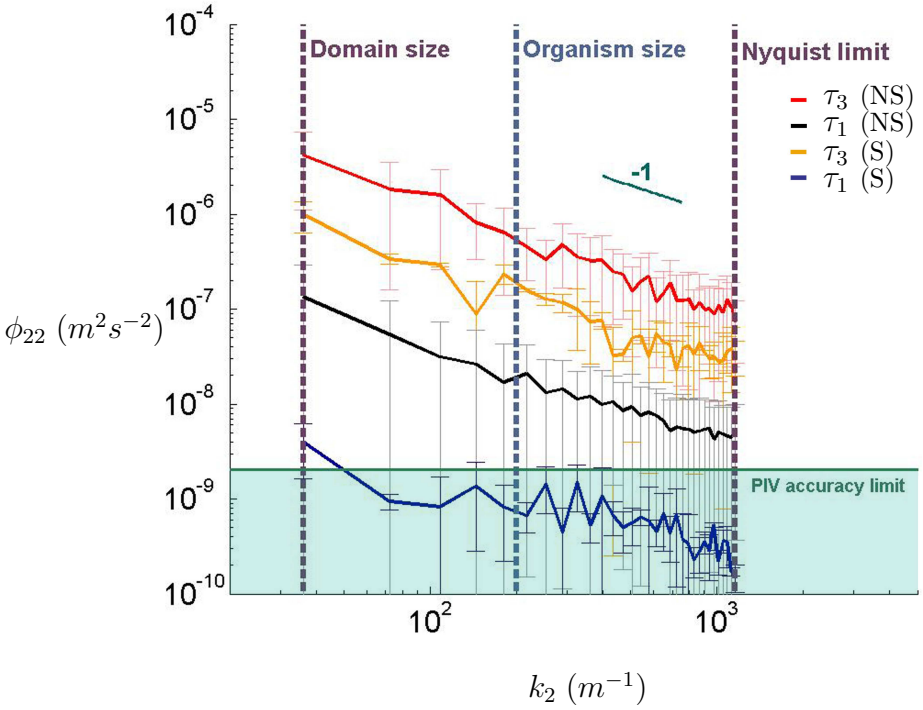

Figure 4.10: Velocity spectrum tensor during vertical migration. The vertical component of the velocity spectrum tensor is shown against vertical wavenumber for the three time delays corresponding to different stages in the migration at which data was acquired. The vertical lines indicate the wavenumbers corresponding to the domain size (i.e., field of view), organism size and the Nyquist limit (i.e., twice the PIV vector spacing). The yellow shaded region indicates increasing kinetic energy at length scales greater than the individual animal size (i.e., wavenumbers smaller than that corresponding to the individual animal size). Only a fraction of the data points were plotted with markers for clarity.

where corrections to the inertial term due to density variations are considered negligible [40]. Similarly to §3.4.2, the mean flow and fluctuating component equations can be derived from this expression via a Reynolds-decomposition of the flow:

$$\tilde{u}_i = U_i + u_i \tag{4.3a}$$

$$\tilde{p} = P + p \tag{4.3b}$$

$$\tilde{\rho} = \overline{\rho} + \rho \tag{4.3c}$$

$$\tilde{f}_i = F_i + f_i \ . \tag{4.3d}$$

Substituting Equations 4.3a - 4.3d into 4.2, and averaging the obtained expression, results in the following set of equations:

Mean-flow equations:

$$\frac{\partial U_i}{\partial t} + U_j \frac{\partial U_i}{\partial x_j} = -\frac{1}{\rho_0}\frac{\partial P}{\partial x_i} + \nu \frac{\partial^2 U_i}{\partial x_j \partial x_j} - \frac{\partial \overline{u_i u_j}}{\partial x_j} - g\frac{\overline{\rho}}{\rho_0}\delta_{i2} + F_i \tag{4.4a}$$

$$\frac{\partial U_i}{\partial x_i} = 0 \tag{4.4b}$$

Fluctuating component equations:

$$\frac{\partial u_i}{\partial t} + U_j \frac{\partial u_i}{\partial x_j} + u_j \frac{\partial U_i}{\partial x_j} + \underbrace{\frac{\partial}{\partial x_j}(u_i u_j - \overline{u_i u_j})}_{\text{non-linear terms}} = -\frac{1}{\rho_0}\frac{\partial p}{\partial x_i} + \nu \frac{\partial^2 u_i}{\partial x_j \partial x_j} - g\frac{\rho}{\rho_0}\delta_{i2} + f_i \tag{4.5a}$$

$$\frac{\partial u_i}{\partial x_i} = 0 \tag{4.5b}$$

Based on the non-local nature of the flow, the non-linear terms in Equation 4.5a can be neglected and the turbulent energy equation can be obtained in spectral space via Fourier transform of each term and multiplying by $\hat{u_i}^*$ as in §3.4.2:

$$\frac{\partial E(\kappa_2, t)}{\partial t} + \frac{\partial}{\partial \kappa_2}(\varepsilon + B) = \Re\Bigg(- \int \left(\hat{u_i}^* \hat{G}_i + i\rho_0^{-1}\kappa_i \hat{u_i}^* \hat{p} - \hat{u_i}^* \hat{f}_i \right) d\boldsymbol{\kappa} \Bigg), \tag{4.6}$$

where the buoyancy flux is defined as [69]:

$$\frac{\partial B}{\partial \kappa_2} = \Re\left(g\frac{\hat{u_i}^* \hat{\rho}}{\rho_0}\delta_{i2} \right) \ .$$

Similarly to the non-stratified case, the derived energy equation is linear as a result of considering the interaction between the large-scale energetic structures and small-scale eddies as the ones dominating the dynamics of the flow. Therefore, the energy spectrum function can only be a linear function of the dissipation and buoyancy flux:

$$E \propto (\varepsilon + B) \ , \tag{4.7}$$

which results in the following scaling:

$$\underbrace{E}_{[L^3T^{-2}]} \propto \underbrace{\frac{\varepsilon + B}{\alpha}}_{[L^2T^{-2}]} \underbrace{\kappa_2^{-1}}_{[L]} \quad . \tag{4.8}$$

4.3.4 Flow Visualizations in Stratified Fluid

Further analysis of the generated flow field was done by superimposing one second of raw PIV images to resolve the pathlines of the flow. As shown in Figure 4.11, this image overlay displayed portions of swirling eddy-like features in the vicinity of the jet that appeared to be at least an order of magnitude greater than the size of an individual swimmer. Comparison of the flow disturbance due to a single swimmer with the resolved sections of the coherent fluid structures indicates that these result from the hydrodynamic interactions during vertical collective motion.

This observation agrees with the computed distribution of kinetic energy with vertical wavenumber during vertical migration, in which greater levels of energy were found to be distributed within scales larger than that pertaining to an individual organism (Figure 4.10). As presented in §3.5, flow visualizations in a larger field of view of a migration event in non-stratified fluid also displayed the formation of larger scale fluid structures than that of the organisms in the vicinity of the migrating aggregations. This suggests that the restricting force due to the stable stratification does not inhibit the onset of fluid instabilities responsible for overturning fluid on scales larger than that of individual swimmers.

As discussed in Chapter 1, the stability of the stratification imposes a cutoff on fluid overturns that can efficiently alter the density distribution of the water column, namely, the Ozmidov scale. Below this length scale, overturning eddies are constrained vertically by buoyancy forces and can only mix fluid horizontally. The next section will focus on determining the mixing efficiency of the observed fluid transport processes during vertical migration. A discussion regarding the

Figure 4.11: Visualization of flow pathlines. Superposition of one second of raw PIV images displays the pathlines of the flow during vertical migration of *A. Salina*. The white elongated shapes indicate the trajectory of the organisms. The flow generated by a single swimmer during 0.16 s is shown in the blue inset at the upper left corner of the image. The orange shadowing indicates the size and shape of the organism at a given instant. Both images are displayed with the same spatial resolution.

size of the observed eddies with respect to the Ozmidov scale is provided in §4.4.1.

4.4 Efficiency of Biogenic Mixing via DVM

As discussed in Chapter 1, almost a decade after field measurements demonstrated the ability of migrating krill aggregations to dissipate energy at a comparable level to the breakup of internal waves [42], the hypothesis that biogenic mixing is relevant to ocean dynamics has remained controversial due to the inability to measure directly the efficiency of this biological process. In crudest terms, the mixing efficiency of DVM is a measure of how effectively mechanical energy, introduced by each organism during propulsion, is converted into an irreversible change of the

density field structure of the water column.

As a consequence of the stability of the ocean stratification, assessment of the mixing efficiency requires knowledge of the resulting energy distribution during DVM. The measurements presented in previous sections prove that fluid structures larger than the size of a single organism result from animal-fluid interactions during the vertical migration of an aggregation, even within a strong stable stratification. Thus, the assumption that the integral length scales of the flow are of the same size as the organisms themselves is not valid, and previous estimates of biogenic mixing based on this premise are underestimated.

Following this line of thought, the final results on our laboratory study are presented in this section, which focuses on the mixing efficiency of DVM. The discussion starts by comparing the large scale structures observed during vertical migration to the Ozmidov scale, followed by the estimation of the mixing efficiency directly from the measured kinetic energy spectra via an energy balance approach. Finally, Chapter 4 closes the analysis with a brief discussion of the impact of DVM in the ocean based on the experimentally derived mixing efficiency.

4.4.1 Mixing coefficient: Estimate via the Ozmidov scale

As discussed in Chapter 1, the mixing efficiency of a given biogenic process can be estimated via a direct comparison of the characteristic length scales of the flow. In this context, the Ozmidov scale l_B bounds the turbulent fluid motions at which efficient vertical mixing can be achieved. By definition, this scale corresponds to a fluid overturn for which inertial effects are fully balanced by buoyancy. Using the rate of kinetic energy dissipation, the magnitude of the velocity of a fluid motion at the Ozmidov scale can be dimensionally set to be $(\varepsilon l_B)^{1/3}$. Furthermore, the balance between inertia and buoyancy can be written in terms of the Froude number as [51]:

$$\frac{(\varepsilon l_B)^{1/3}}{N l_B} = 1 \quad , \tag{4.9}$$

from which the length scale of such motion is given by

$$l_B = \sqrt{\frac{\varepsilon}{N^3}} \ . \tag{4.10}$$

As derived in §1.3.1, the mixing coefficient Γ, associated with the mixing efficiency or Richardson number, can be written in terms of the Ozmidov scale,

$$\begin{aligned} \Gamma &\approx \left(\frac{L}{l_B}\right)^{4/3} \qquad L < l_B \\ \Gamma &\approx \gamma_0 \qquad\qquad L \geq l_B \ , \end{aligned} \tag{4.11}$$

where γ_0 is the maximum feasible value. Thus, fluid motions with an integral length scale of the same order of magnitude as the Ozmidov scale, or greater, can achieve the efficiency factor set by the hydrodynamic mixing mechanism that is induced during a given biogenic process.

To determine the mixing coefficient in the experimentally induced migrations of *A. salina*, the rate of turbulent kinetic energy dissipation was estimated from the PIV measurements. By definition, precise measurement of ε requires information regarding the velocity gradients in the three directions [93]:

$$\varepsilon = 2\nu\overline{s_{ij}s_{ij}} \ , \tag{4.12}$$

where s_{ij} is the fluctuating strain rate:

$$s_{ij} = \frac{1}{2}\left(\frac{\partial u_i}{\partial x_j} + \frac{\partial u_j}{\partial x_i}\right) \ . \tag{4.13}$$

Expanding Equation 4.12 yields:

$$\varepsilon = \nu\overline{\left(2\left(\frac{\partial u_1}{\partial x_1}\right)^2 + \left(\frac{\partial u_2}{\partial x_1}\right)^2 + \left(\frac{\partial u_3}{\partial x_1}\right)^2 + \left(\frac{\partial u_1}{\partial x_2}\right)^2 + 2\left(\frac{\partial u_2}{\partial x_2}\right)^2 + \left(\frac{\partial u_3}{\partial x_2}\right)^2 + \left(\frac{\partial u_1}{\partial x_3}\right)^2 + \left(\frac{\partial u_2}{\partial x_3}\right)^2 + 2\left(\frac{\partial u_3}{\partial x_3}\right)^2 + 2\left(\frac{\partial u_1}{\partial x_2}\frac{\partial u_2}{\partial x_1}\right) + 2\left(\frac{\partial u_1}{\partial x_3}\frac{\partial u_3}{\partial x_1}\right) + 2\left(\frac{\partial u_2}{\partial x_3}\frac{\partial u_3}{\partial x_2}\right)\right)} \quad .$$

This quantity was estimated from the two-dimensional PIV measurements presented in this chapter by assuming that the velocity component in the direction perpendicular to the measurement plane was comparable to the measured horizontal velocity component:

$$u_3 \approx u_1 \quad , \tag{4.14}$$

and, similarly, gradients in this direction were assumed to be proportional to horizontal gradients:

$$\frac{\partial}{\partial x_3} \approx \frac{\partial}{\partial x_1} \quad . \tag{4.15}$$

Substituting conditions 4.14 & 4.15 into Equation 4.4.1 results in:

$$\varepsilon = \nu\overline{\left(2\left(\frac{\partial u_1}{\partial x_1}\right)^2 + \left(\frac{\partial u_2}{\partial x_1}\right)^2 + \left(\frac{\partial u_1}{\partial x_1}\right)^2 + \left(\frac{\partial u_1}{\partial x_2}\right)^2 + 2\left(\frac{\partial u_2}{\partial x_2}\right)^2 + \left(\frac{\partial u_1}{\partial x_2}\right)^2 + \left(\frac{\partial u_1}{\partial x_1}\right)^2 + \left(\frac{\partial u_2}{\partial x_1}\right)^2 + 2\left(\frac{\partial u_1}{\partial x_1}\right)^2 + 2\left(\frac{\partial u_1}{\partial x_2}\frac{\partial u_2}{\partial x_1}\right) + 2\left(\frac{\partial u_1}{\partial x_1}\frac{\partial u_1}{\partial x_1}\right) + 2\left(\frac{\partial u_2}{\partial x_1}\frac{\partial u_1}{\partial x_2}\right)\right)}$$

which can be simplified to:

$$\varepsilon = \nu\overline{\left(8\left(\frac{\partial u_1}{\partial x_1}\right)^2 + 2\left(\frac{\partial u_2}{\partial x_1}\right)^2 + 2\left(\frac{\partial u_1}{\partial x_2}\right)^2 + 2\left(\frac{\partial u_2}{\partial x_2}\right)^2 + 4\left(\frac{\partial u_2}{\partial x_1}\frac{\partial u_1}{\partial x_2}\right)\right)} \quad , \tag{4.16}$$

and calculated by implementing the `gradient` function in Matlab, which uses a central difference scheme[1].

[1]Primary error sources in the calculation of ε from PIV measurements stem from the estimation of the spatial velocity gradients [88]. This error is minimized for an optimal spacing of the velocity vector grid, such that the spacing between grid points Δx is of the same order as the Kolmogorov scale η. Integration of the velocity spectrum tensor resulted in $\eta = (\nu^3/\varepsilon)^{1/4} = O(10^{-3})$ m, i.e., $\eta \approx \Delta x$.

Under these assumptions, the Ozmidov scale was estimated as defined in Equation 4.10 by spatially averaging the computed values of turbulent kinetic energy dissipation rate within the field of view and noting that the measured buoyancy frequency was nominally $N = 0.1$ s^{-1} (Figure 4.2). This resulted in an average value of $l_B = 4.1 \pm 1.9$ cm.

The integral scale of the flow field during vertical migration of *A. salina* was given by that corresponding to the large-scale eddies generated via a Kelvin-Helmholtz instability of the fluid jet. It can be assumed that the upper limit for this measure was set by the size of the structures observed in a non-stratified water column, which was found to be $L \approx 0.1$ m. In the presence of a strong stratification, fluid overturns were also observed, but its scale could not be resolved given that their size was larger than the field of view of the camera. Qualitatively, however, they appeared to be at least on the order of $L \approx 10^{-2}$ m. Therefore, the size of the most energetic fluid scales generated via DVM can be considered to be at least of the same order of magnitude as the Ozmidov scale and, as a result, the efficiency factor is not bounded by the ratio of these length scales, i.e., $\Gamma = \gamma_0$.

4.4.2 Mixing efficiency: An Energy Balance Approach

Most literature does not make a distinction between the mixing efficiency R_f and the mixing coefficient Γ (defined in Equations 1.1 and 1.5). They are conversely used to characterize mixing and, what is more, the maximum value of the mixing coefficient achieved within the efficient mixing regime ($L \geq l_B$) is automatically set to be $\gamma_0 = 0.2$ without further clarification.

In reality, the parameter characterizing the mixing efficiency of a given hydrodynamic transport mechanism is given by the flux Richardson number, whereas the coefficient Γ is the ratio between the buoyancy flux and the rate of kinetic energy dissipation [87], [68]. The definition of both measures can be derived from the

turbulent kinetic energy equation:

$$\underbrace{\frac{D}{Dt}\frac{1}{2}\overline{u_i u_i}}_{\text{I}} = \underbrace{-\overline{\frac{u_i}{\rho_0}\frac{\partial p}{\partial x_i}} - \frac{\partial}{\partial x_j}\frac{1}{2}\overline{u_i u_i u_j} + 2\nu\frac{\partial}{\partial x_j}\overline{(u_i s_{ij})}}_{\text{II}} \underbrace{-\overline{u_i u_j}\frac{\partial U_i}{\partial x_j}}_{\text{III}} - \underbrace{\overline{u_i\frac{\rho}{\rho_0}g\delta_{i2}}}_{\text{IV}} - \underbrace{\varepsilon}_{\text{V}} \ , \tag{4.17}$$

where I is the total rate of change of turbulent kinetic energy, II represents its spatial distribution by the turbulent transport terms, III is the production rate of turbulent kinetic energy due to shear, IV is the work done by the buoyancy flux, and V is the rate of turbulent kinetic energy dissipation.

Assuming steady state and neglecting turbulent advection by the mean flow, the balance of kinetic energy occurs between the production term P, the work against buoyancy B, and the dissipation rate ε [69]:

$$\underbrace{-\overline{u_i u_j}\frac{\partial U_i}{\partial x_j}}_{P} = \underbrace{\overline{u_i\frac{\rho}{\rho_0}g\delta_{i2}}}_{B} + \varepsilon \ , \tag{4.18}$$

where the transport terms in Equation 4.17 are assumed to spatially transfer energy in between fluid scales without changing the total amount of energy [69].

The mixing coefficient Γ can be derived by substituting the definition of flux Richardson number into Equation 4.18 [69]:

$$R_f = \frac{B}{P} \ , \tag{4.19}$$

$$\frac{B}{R_f} = B + \varepsilon$$

$$B\left(\frac{1}{R_f} - 1\right) = \varepsilon$$

$$B = \left(\frac{R_f}{1 - R_f}\right)\varepsilon = \Gamma\varepsilon \ . \tag{4.20}$$

It is evident from Equation 4.20 that the value of the mixing efficiency R_f must

be less than unity, whereas the mixing coefficient Γ can, in principle, be defined by any positive constant $\Gamma = \gamma_0 \geq 1$ (if $L \geq l_b$).

In the ocean, the mixing efficiency of internal wave breaking via shear between the stratified ocean layers has been reported to be in the range $0.18 \leq R_f \leq 0.2$, which results in a mixing coefficient $\Gamma \approx 0.2$. Theoretical predictions as well as experimental observations of mixing via this mechanism agree with this value. Thus, assuming that $\Gamma \approx R_f = 0.2$ is only appropriate when mixing is induced via the onset of a Kelvin-Helmholtz instability due to a horizontally oriented shear layer with respect to a stable vertical density profile. Here, it has been observed that vertical migration also results in the development of a shear layer that becomes Kelvin-Helmholtz unstable. However, in this case, the shear layer and the density profile are collocated. Thus, the assumption that $\Gamma \approx 0.2$ for biogenic mixing via DVM is not necessarily valid.

The mixing efficiency R_f can be calculated based on the energy balance in Equation 4.18, from which the mixing coefficient Γ can be derived and used to compute a diffusivity constant to characterize the biogenic mixing process. In this case, the derived eddy diffusivity of heat can be assumed to be equal to that of density given that the stratification was solely imposed by a linear temperature gradient in the experimental apparatus [93].

Following this methodology, the energy balance in Equation 4.18 can be applied to the experimental sets in homogeneous as well as in stratified fluid. In the presence of a stable thermal stratification, the balance of kinetic energy occurs between the production of turbulent kinetic energy P_s and losses due to buoyancy B as well as dissipation ε_s, whereas in an homogeneous fluid production P_{ns} is fully balanced by viscous dissipation ε_{ns} alone:

$$\begin{aligned} P_s &= B + \varepsilon_s \\ P_{ns} &= \varepsilon_{ns} \quad , \end{aligned} \tag{4.21}$$

where it can be assumed that $P_s = P_{ns}$ given that the same number of organisms

were introduced into the tank and measurements were taken at the same stage of the vertical migration. Substituting these expressions in the definition of mixing efficiency yields:

$$R_f = \frac{B}{P_s} = \frac{P_s - \varepsilon_s}{P_s} = \frac{P_{ns} - \varepsilon_s}{P_{ns}} = \frac{\varepsilon_{ns} - \varepsilon_s}{\varepsilon_{ns}} \quad . \tag{4.22}$$

The kinetic energy dissipation rate in the measurement plane was estimated by integrating the trace of the velocity spectra of the corresponding experimental sets[2]:

$$\begin{aligned} \varepsilon_s &= 2\nu \int_{\kappa_{2_{min}}}^{\kappa_{2_{max}}} \int_{\kappa_{1_{min}}}^{\kappa_{1_{max}}} \kappa_1 \kappa_2 (\phi_{11_s} + \phi_{22_s}) d\kappa_1 d\kappa_2 \\ \varepsilon_{ns} &= 2\nu \int_{\kappa_{2_{min}}}^{\kappa_{2_{max}}} \int_{\kappa_{1_{min}}}^{\kappa_{1_{max}}} \kappa_1 \kappa_2 (\phi_{11_{ns}} + \phi_{22_{ns}}) d\kappa_1 d\kappa_2 \quad . \end{aligned} \tag{4.23}$$

An ensemble average over the acquired experimental sets resulted in: $\varepsilon_{ns} = 5.56 \times 10^{-6}$ m^{2}s^{-3} and $\varepsilon_s = 1.84 \times 10^{-6}$ m^{2}s^{-3}. Therefore, the mixing efficiency for the observed vertical migrations is[3]:

$$R_f = \frac{\varepsilon_{ns} - \varepsilon_s}{\varepsilon_{ns}} = 0.67 \pm 0.19 \tag{4.24}$$

and thus the mixing coefficient results in

$$\Gamma = \frac{R_f}{1 - R_f} = 2.02 \quad , \tag{4.25}$$

which is considerably greater than the assumed value of $\Gamma = 0.2$. The reason behind this discrepancy is that mixing during vertical migration occurs via a very different mechanism than the one behind this commonly observed value in the ocean. As described in Chapter 1, kinetic energy from winds and tides penetrates the ocean depth via internal waves, which can propagate and oscillate between isopycnals, i.e., iso-density surfaces. One mechanism by which energy is released

[2]The components of the velocity spectrum ϕ_{11} and ϕ_{22} computed via `fft2` in Matlab were compensated by the magnitude of κ_1 and κ_2 such that the dimensions were $\phi_{ij}[=]L^5T^{-2}$.

[3]Evaluation of R_f via the calculation of ε_{ns} and ε_s with the PIV method described in §4.4.1 resulted in $R_f = 0.72 \pm 0.31$.

and transformed into potential energy, perhaps the most commonly observed one, is via the onset of a shear-induced Kelvin-Helmholtz instability in between isopycnals. The necessary condition for instability to occur in such a horizontal shear flow is given by a constant known as the gradient Richardson number Ri, which provides a measure of the relative strength of the stratification with respect to the generated shear:

$$Ri = \frac{N^2}{(dU/dz)^2} \tag{4.26}$$

If $Ri < 0.25$, then small disturbances cannot be stabilized by the stratification and the formation of billows occurs, leading to overturns and subsequent mixing at the interface of the fluid layers. Another type of shear-induced instability is the Holmboe instability, which is induced in a similar manner to the Kelvin-Helmholtz. In this case, the shear layer is thicker than the thickness of the isopycnal and, as a result, a different billow structure develops. Numerical analyses of this regime suggest that higher mixing efficiencies can be achieved prior to turbulence in such unstable shear flows [84].

Here, the shear discontinuity is introduced perpendicular to the isopycnals. Further development of the hydrodynamic instability results in fluid overturns in the region adjacent to the migration, in which denser fluid is positioned above lighter fluid. Moreover, the multi-scale nature of the flow promotes continuous entrainment of the surrounding fluid. The far-field observations obtained in homogeneous fluid as well as the high value of the mixing efficiency in the presence of stratification indicate that the downward jet produced by the hydrodynamic interactions between neighboring swimmers induces the development of a Rayleigh-Taylor instability in a linearly stratified fluid.

This flow instability has been extensively studied in a closed two-layered system. In this case, the mixing efficiency has been found to be $R_f \approx 0.5$ [13]. However, recent experimental investigations show that if the instability is constrained within a stable stratification, much higher mixing efficiencies are possible. In the case of an instability developing within a stable linear stratification, the mixing efficiency

was found to reach a value of $R_f = 0.75$ [48]. The main reason behind this difference is that, in the simplified version of an unstable step-wise stratification, the amount of mixing that can be achieved is constrained by the amount of potential energy that is initially available to mix fluid [48], whereas if the instability develops within a stable stratification, the limitation on the efficiency is imposed by the energetics of the system rather than by its initial boundary conditions [107]. In the latter case, the upper bound on the efficiency is set by the growth of the mixing layer and the fluid properties in this region [107].

As mentioned above, these results can be extrapolated to evaluate the contribution of diel vertical migrations to upper ocean mixing via the calculation of a vertical eddy diffusivity, except for regions susceptible to double diffusion [93]. This can be achieved by using the mixing coefficient to relate the kinetic energy dissipation rate measured in the ocean to the eddy diffusivity K, defined as [69]

$$K = \frac{g\overline{u_2\rho}\rho_0^{-1}}{N^2} \quad , \tag{4.27}$$

and using expression 4.20:

$$K = \frac{B}{N^2} = \Gamma\frac{\varepsilon}{N^2} \quad . \tag{4.28}$$

Field measurements of the rate of kinetic energy dissipation in the nearby region of vertically migrating aggregations are available only for strongly stratified coastal regions $N = 10^{-2}$ s^{-1} [42], [80]. While intense events yielding values of ε up to 10^{-5} m^{2}s^{-3} have been reported [42], subsequent field studies in the same geographical region revealed ε to commonly range from 10^{-9} to 10^{-7} m^{2}s^{-3} [80]. Due to the high efficiencies associated with vertical migrations of *A. salina*, we expect vertical diffusivities in these cases to range in the order of 10^{-5} to 10^{-3} m^{2}s^{-1} with rare events in the order of 10^{-1} m^{2}s^{-1}, which is comparable to the effect of internal wave breakup near bottom ocean topography spanning from 10^{-5} m^{2}s^{-1} to values exceeding 10^{-3} m^{2}s^{-1} very close to the boundaries [74], [22].

4.5 Discussion

The results presented in Chapter 3 regarding the fluid dynamic interactions between adjacent organisms during vertical migration of an aggregation were extended in this chapter to include the effect of a stable stratification. Thermal stratification of the water column prior to animal migration resulted in a density gradient characterized by a buoyancy frequency $N = 10^{-1}$ s^{-1}, which was at least an order of magnitude greater than the one measured in upper ocean regions. This was due to the constraint imposed by the physical dimensions of the test tank on the maximum temperature difference that can be set between the top and bottom of the water column. Nonetheless, the results from this study provide a lower bound on the induced transport and mixing that can be achieved by vertical migrations of zooplankton in a stratified medium.

The velocity measurements obtained with PIV showed that the dynamic evolution of the flow was not dramatically changed by the effect of buoyancy. As expected, vertical transport was hindered, but the development of a downward jet as well as the evolution of a multi-scale flow was similar to that in non-stratified conditions. The decay of the measured velocity spectra obeyed the same κ^{-1} law as measurements obtained in a homogeneous fluid. This behavior was modeled as in Chapter 3, by neglecting the non-linear terms in the equations of motion, based on the non-local nature of the flow. The effect imposed by stratification on the energy equation occurs via the buoyancy flux term, which acts as an additional sink to the rate of change of kinetic energy. While viscous dissipation transforms the available kinetic energy to heat, buoyancy fluxes transform it into background potential energy. These processes change the total kinetic energy in the flow, but they do not inhibit the dominant interactions between well-separated scales. The most important consequence is that, even in the presence of stratification, an inverse cascade from the small scales at which individual organisms introduce kinetic energy into the flow to larger scales at which mixing can be done effectively is triggered via the onset of shear-dominated hydrodynamic instabilities. Therefore, these observations do not agree with the assumption that biogenic mixing is an inefficient process due to the inability to introduce energy at scales large enough

to impact the density structure of the water column.

The mixing efficiency was estimated following a traditional energy balance method, from which a mixing efficiency of $R_f = 0.67$ was obtained for the experimental observations described in this chapter, which means that more than half of the produced kinetic energy is converted into potential energy by buoyancy fluxes. This estimate agrees with the notion that DVM trigger a Rayleigh-Taylor instability, which has been observed to be an efficient mixing mechanism whenever the instability is confined within a stable stratification. As mentioned in Chapter 1, there is no general theory to quantify mixing and, as a consequence, various methodologies have been proposed in this field. The major criticism of estimating mixing based on momentum arguments is that it does not account for molecular diffusion [41]. Irreversible mixing is indeed only achieved by diffusing away the property gradients resulting from transport mechanisms. However, the mixing efficiencies derived via the presented method are valid given that the density gradient is solely imposed by changes in temperature [93]. Thus, the eddy diffusivity derived via the mixing coefficient can be assumed to be comparable to that of heat.

Chapter 5

Effect of Swimmer Configuration on Fluid Transport During Vertical Collective Motion

5.1 Introduction

The focus of the present document has hitherto been centered on the experimental investigation of fluid transport and mixing by vertically migrating aggregations of *A. salina* in the laboratory. Here, a complementary numerical method is presented that employs PIV data of individual critters to study the effect of animal configuration within a migrating aggregation as well as swimming mode in the limit of a dilute animal aggregation. The main motivation for the development of this tool is the difficulty and expense associated with the experimental and in situ identification of potential efficient biogenic mixers. It has long been hypothesized that swimming mode as well as animal configuration within a group is most likely to have an important effect regarding vertical transport and mixing [36]. Furthermore, besides metachronal swimmers, such as krill, copepods, and other species of zooplankton, have been proposed as relevant species. Thus, to this end, a numerical method that implements velocimetry data of an individual swimmer to facilitate the assessment of induced vertical transport and mixing within DVM is presented in this chapter.

As discussed in Chapter 1, numerical models that simulate the flow due to individual swimmers based on solutions to the Stokes equations have been proposed to study biogenic mixing. These models are invaluable since they have success-

fully captured the far-field time-averaged flow generated by an active swimmer. However, disagreement with experimental observations of enhanced fluid transport suggests the necessity to include the near-field flow in the analysis in order to correctly estimate the amount of fluid being drifted by a self-propelled animal. To this effect, and with the aim of exploiting a decade-long of successful velocimetry data acquisition by biologists, fluid dynamicists, and oceanographers, the proposed method directly implements processed velocimetry data of individual swimmers to simulate DVM of dilute aggregations.

Similar to the potential flow model by Dabiri [12], vertical migration of multiple swimmers is simulated by arranging a number of self-propelled organisms to a pre-determined configuration, such that no spatial overlap of the flow due to neighboring swimmers occurs. Fluid transport is then quantified by tracking the advection of virtual fluid particles due to the vertical motion of simulated swimmers. In contrast to the potential flow model analysis, however, the fluid velocity due to a swimmer is not evaluated from potential flow solutions of migrating spheres, but rather obtained from processed experimental PIV measurements of *Aurelia aurita*. Therefore, not only is the near-field flow signature incorporated, but also the unsteady nature of animal propulsion.

A description of the raw velocimetry data for the swimming ephyrae as well as of the PIV processing routine is enclosed in §5.2.1 and §5.2.2, respectively. The setup of the numerical model and the parameters of the numerical experiments are documented in §5.2.3, which includes a description of the fluid particle advecting scheme. Results regarding fluid transport due to the explored animal configurations are presented in §5.3 in terms of the drift volume, in the case of a single swimmer, and mean drift of the tracked fluid particle batch in the case of aggregations of multiple swimmers. Finally, mixing is quantified via the calculation of a vertical diffusivity computed from the absolute dispersion of the simulated fluid particles. A brief discussion is provided in §5.4.

5.2 Methodology

5.2.1 Flow Field Measurements

The flow generated by an individual swimming ephyrae of the scyphozoan jellyfish *Aurelia aurita* was measured using two-dimensional PIV [1]. Measurements were taken in water with constant salinity at room temperature, previously seeded with neutrally buoyant silver-coated hollow glass spheres of 13 μm in diameter (Potter Industries Inc.). The particles were illuminated within a two-dimensional plane using a 532 nm (green), 300 mW laser (Laserglow Technologies) and a cylindrical lens (-4 mm of focal length). High-definition video was acquired at 30 fps using a Sony Handycam oriented perpendicular to the laser sheet [63].

5.2.2 PIV Data Processing

Raw PIV images were processed using a similar procedure as the one described in §2.3.4 to obtain a time series of instantaneous velocity fields. Consecutive image pairs were cross-correlated using Davis 9 (LaVision Inc.). Image interrogation was conducted via two multi-pass iterations of decreasing window size from 64×64 to 32×32 pixels with a 50% overlap. Post-processing of the velocity fields was done by applying a universal outlier detection test.

5.2.3 Numerical Method

The structure of the developed numerical model is based on the idea of using the time series of PIV measurements for a single organism as building blocks to simulate longer vertical swimmer trajectories and construct aggregations of self-propelled swimmers with the constraint of not allowing any spatial overlap of the flow field between neighboring swimmers. To ensure continuity as vertical trajectories are extended, only velocimetry measurements corresponding to complete swimming strokes are identified and cropped at a given horizontal and vertical distance from the centroid of the organism as described below. These cropped

[1] Data was acquired by Dr. Janna Nawroth during her graduate studies at Caltech and the results presented here are reproduced under her permission.

velocity fields are then introduced onto a larger domain at a prescribed position below a row of simulated fluid particles and set to translate vertically according to the vertical displacement of the centroid position of the organism in the raw images. As the organisms migrate vertically, the position of the fluid particle patch is tracked and used to determine fluid transport and mixing via Lagrangian statistics.

Centroid Identification

To accurately determine the centroid of the jellyfish at each time step, the raw PIV images were analyzed in Adobe Photoshop Elements 9 to discern the contour of the jellyfish body from the background. After loading each image onto the program, the contour of the organism was manually identified using the selection brush tool. The region encompassed by the selected contour was marked with white, and the uneven illumination of the image due to the reflection of the PIV particles was replaced with a uniform black background (Figure 5.1). This procedure was done individually for every image of the raw data set.

The centroid position was then computed from the obtained black-and-white images using the `regionprops` command in Matlab. As shown in Figure 5.1, the jellyfish was originally captured swimming towards a deeper vertical position (see [63]). However, given that the organism is neutrally buoyant, inverting its orientation does not modify the generated flow field. Therefore, the images were flipped in the vertical direction to simulate vertical migrations from a deeper denser region to a shallower one (see Figure 5.2).

Cropping of the Velocity Field

As shown in [63], the vorticity generated by *Aurelia aurita* during propulsion is compact in a region close to the body of the organism. Therefore, the instantaneous velocity fields were cropped along a rectangular box of constant width and height (12.16×8.96 mm, respectively) outside of which $\nabla \times \mathbf{u} = 0$, as shown in Figure 5.3.

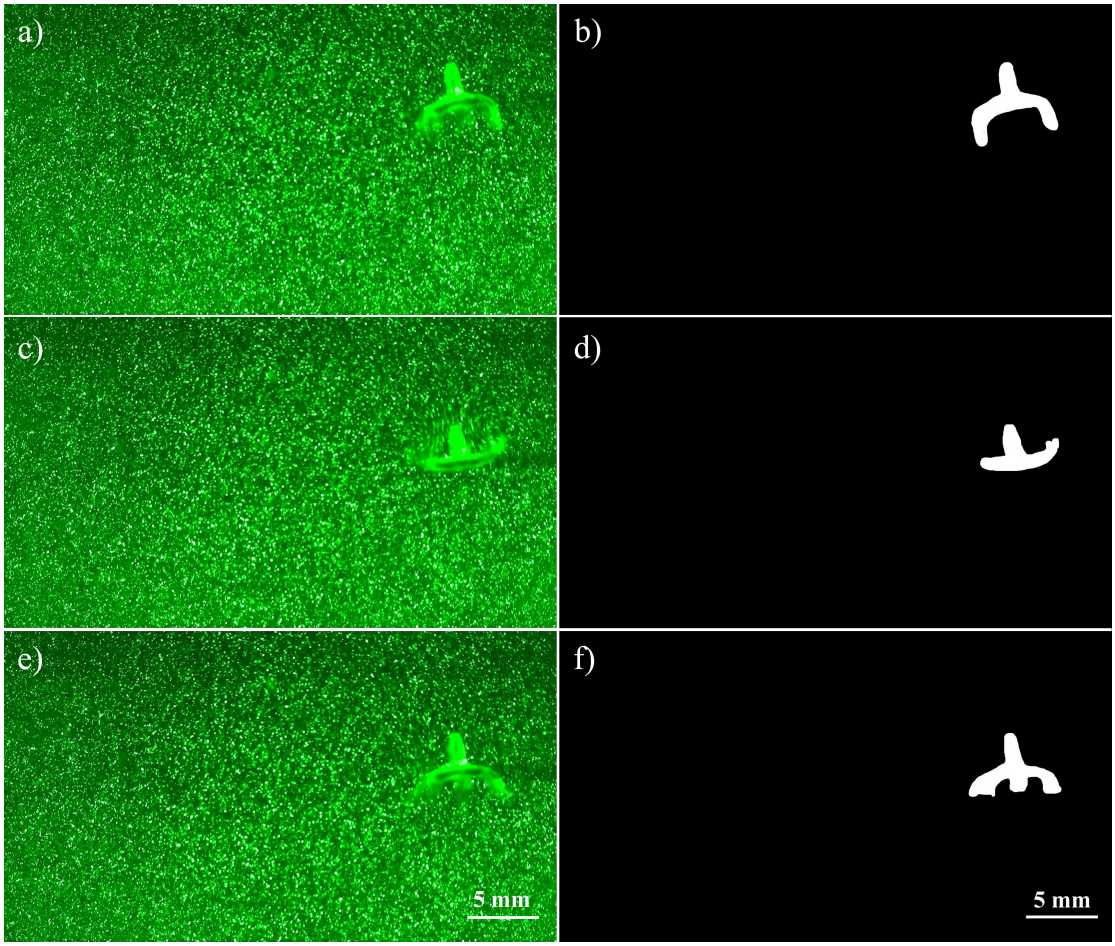

Figure 5.1: Animal contour detection. Image pairs showing raw PIV images (a,c,d) and their processed versions displaying the identified jellyfish contour (b,d,e) within different time steps. The time between image pairs is $\Delta t = 0.27$ s.

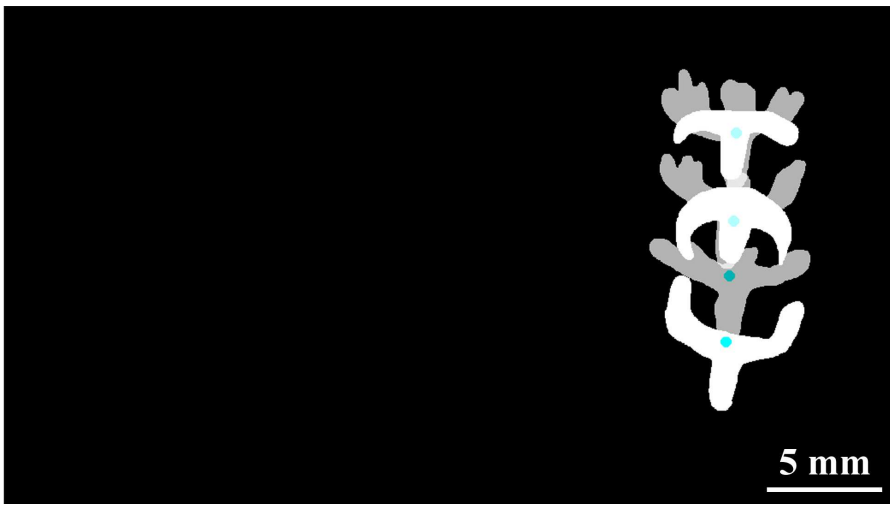

Figure 5.2: Centroid detection of *Aurelia aurita*. This image shows the position of the jellyfish with the modified orientation adopted to simulate the vertical migration of the organism at different instants separated by a time lapse $\Delta t = 0.46$ s. The computed centroid position of the organism is denoted with a blue dot.

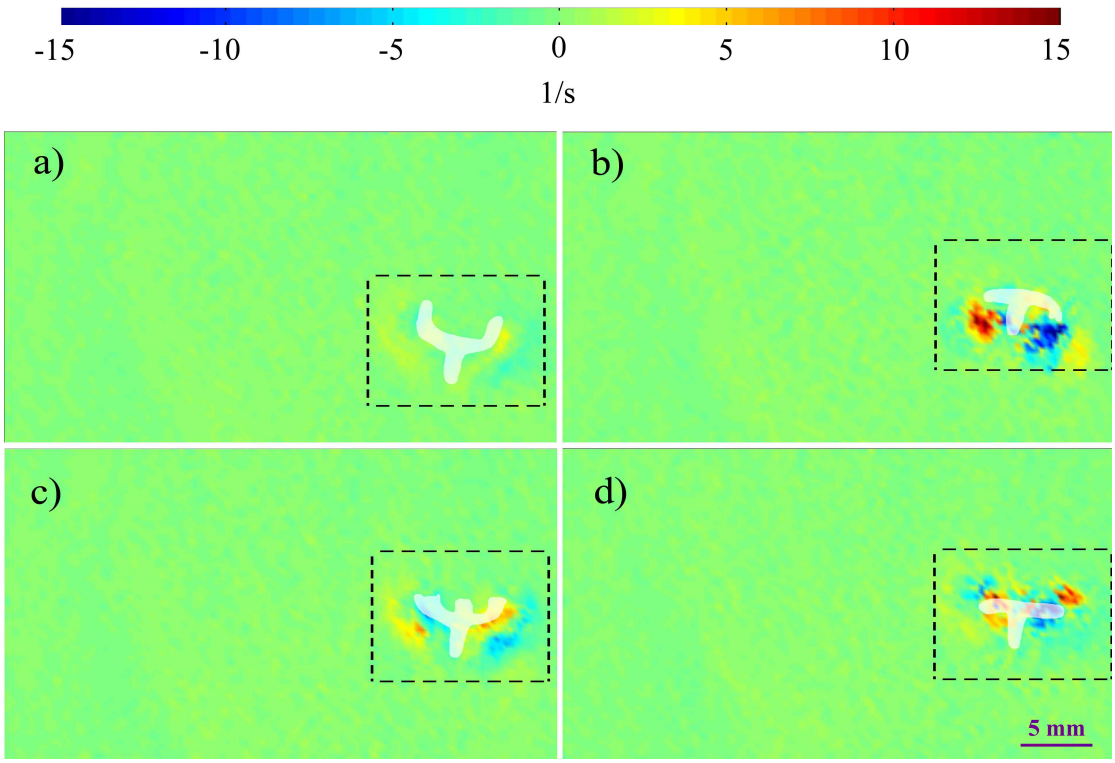

Figure 5.3: Vorticity field series during propulsion of *Aurelia aurita*. The vorticity field during propulsion is shown for the complete camera field of view. The broken lines define the rectangular region used to crop the velocity fields at each instant. The time between images is $\Delta t = 0.27$ s.

A total of five swimming strokes were identified in the raw data, from which the first and last one had to be discarded due to the proximity of the body of the jellyfish to the top and bottom edges of the field of view. As a result, instantaneous velocity fields spanning three complete swimming strokes were cropped with respect to the centroid of the organism at each frame. To this end, the velocity field was linearly interpolated such that the centroid position was included within the set of nodes of the velocity grid, with respect to which the crop box was defined.

Numerical Experiments

The velocity information spanning three swimming strokes, encompassed within the box described above, constituted the elementary unit from which vertically migrating aggregations were constructed in our model. As illustrated in Figure 5.4, four different configurations of jellyfish aggregations were analyzed, according to the case studies of the potential flow model in [12]. This included the following cases:

- A single swimmer migrating vertically
- An aggregation of swimmers migrating in line
- An aggregation of swimmers vertically migrating in a two-column staggered formation
- An aggregation of swimmers vertically migrating in a three-column staggered formation

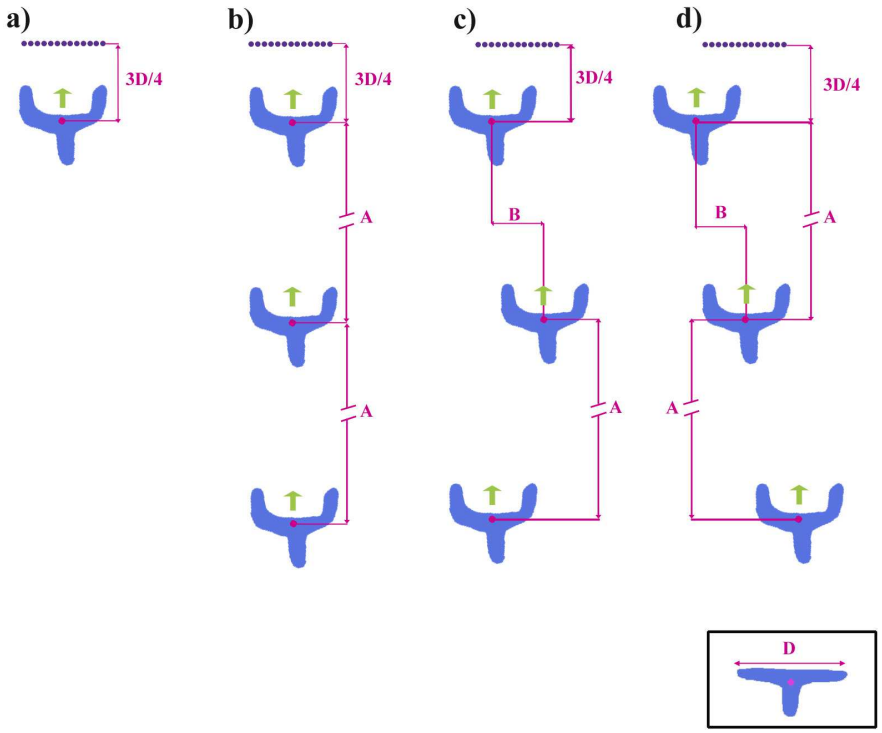

Figure 5.4: Test configurations of simulated DVM of *Aurelia aurita*. Four different animal configurations were numerically studied: a single migrating organism (a), multiple organisms vertically migrating in line (b), multiple organisms migrating in a two-column staggered formation (c), and multiple organisms migrating in a three-column staggered formation(d). Upper case letters A and B denote the inter-organism vertical and horizontal spacing, respectively, while the sketch inside the black outlined box at the bottom right corner indicates the definition of one body diameter D (7.3 mm).

The vertical migration of aggregations of multiple organisms was simulated both in a non-stratified ($N = 0$ s^{-1}) and stratified ($N = 10^{-3}$ s^{-1}) fluid environments. Simulations were done setting the vertical spacing between swimmers to be the vertical distance at which maximum fluid transport is acquired by a single vertically migrating jellyfish ($8.5D$). The horizontal spacing between neighboring

organisms was set to be $1/2D$, in agreement with the guidelines presented in [12]. Additional tests using a smaller spacing were conducted for the two-column and three-column staggered cases in stratified fluid, where vertical and horizontal spacings between swimmers were set to be $4.25D$ and $1/4D$, respectively. A summary of the parameters used in all the simulations presented in this chapter are summarized in Table 5.1.

Buoyancy frequency	$N = 10^{-3}\ s^{-1}$		$N = 0\ s^{-1}$
Vertical inter-organism spacing	$8.5D$	$4.25D$	$8.5D$
Horizontal inter-organism spacing	$1/2D$	$1/4D$	$1/2D$
Number of swimmers	36	38	36

Table 5.1: Numerical model parameters.

Fluid transport was quantified by continuously tracking the position of a batch of twenty fluid particles during each numerical experiment. In each case, the simulated row of equidistant fluid particles was initialized $3/4D$ above the centroid of the first swimmer of the aggregation and set to horizontally span one body diameter ($D = 7.3$ mm). The initial positions of the swimmers was given by the parameters in Figure 5.3 and Table 5.1. Vertical migration of each swimmer within an aggregation was initialized by introducing the first cropped velocity field at its starting position. Thereafter, each swimmer was allowed to migrate vertically by subsequently introducing the series of cropped velocity fields at a vertical position set by the displacement of the jellyfish centroid in the raw PIV images for the duration of the three strokes of acquired PIV data. Once the last velocity field of the third acquired stroke was introduced, the first cropped velocity field from the measurement series was inserted at the same vertical position to simulate a larger vertical swimming trajectory. In all configurations, vertical migration was simulated until the centroid of the first swimmer in the aggregation had translated

$300D$ from its starting position.

Particle Advection Scheme

In non-stratified fluid, the instantaneous position of each fluid particle was computed by solving the following initial value problem using the forward Euler method with a time step set by the PIV image acquisition rate ($\Delta t = 0.033$ s):

$$\frac{d\mathbf{x}}{dt} = \mathbf{u}(x_1, x_2) \ , \quad \mathbf{x}(t_0) = \mathbf{x}_0 \ , \tag{5.1}$$

where $\mathbf{u}(x_1, x_2)$ is the measured velocity field at each particle position.

In the limit of small density variations, the effect of buoyancy on fluid transport was taken into account by incorporating an effective velocity, acting only in the vertical direction as a result of the buoyancy acceleration under the Boussinesq approximation [12], [98]:

$$\mathbf{u}_b = -N(x_2 - x_{2_0})\hat{\mathbf{j}} \ , \tag{5.2}$$

where x_{2_0} is the density equilibrium depth, taken to be the position in the vertical direction at which the particle row was initialized.

Fluid advection in a homogenous water column was hence estimated using Equation 5.1, whereas Equations 5.1 and 5.2 were combined to estimate fluid transport in the presence of a weak linear stratification. In the interest of comparing our results with those reported by [12] for a force-free swimmer potential flow model, numerical experiments were performed for the same values of the buoyancy frequency, namely $N = 0$ s^{-1} and $N = 10^{-3}$ s^{-1}.

5.3 Results

The results of numerical experiments done with a single swimmer migrating upwards already demonstrate the influence of the near-field flow on large scale fluid transport. As illustrated in Figures 5.5 and 5.6, it was observed that as the ephyrae

propelled itself upwards, the horizontal fluid particle batch, initially placed ahead of the organism, was quickly trapped and advected within the bell region close to the jellyfish body. Snapshots of the cropped velocity field during vertical migration are shown in Figure 5.5, along with the position of fluid particles near the body of the organism simulated considering both $N = 0$ s^{-1} and $N = 10^{-3}$ s^{-1}. From these images, it is evident that stratification does not severely impede vertical fluid transport, and in fact; its effect is only truly felt once the particles have been greatly displaced from its equilibrium position. Figure 5.6 shows the position of all the particles within the batch at four different time instants separated by $\Delta t = 0.47$ s during vertical migration. It was found that fluid particles were vertically transported up to 8 body diameters from their starting position, in non-stratified fluid, and up to 6.4 body diameters if the effect of buoyancy was considered. These estimates agree with observations of large scale fluid transport both in situ and in the laboratory for vertically migrating jellyfish [37], [62]. Furthermore, a similar numerical analysis incorporating experimentally acquired velocimetry data of an individual jellyfish yields large scale fluid transport during vertical migration as well [35].

Fluid particle trajectories simulated in both fluid conditions are presented in Figure 5.7. In both cases, the organism was set to migrate a total of twenty body diameters starting $3/4D$ below the horizontal particle batch, which was initialized at $x_2 = 0$ mm. The horizontal position of the centroid of the organism was aligned with the particle batch, which was centered at the origin. In contrast to the flow generated via potential flow model solutions of a translating solid sphere [12], fluid particle trajectories are greatly influenced by the jellyfish wake structure. In this case, the production of wide vortex rings during propulsion induces large scale fluid transport via drift, as seen in other jellyfish species with the same propulsion mechanism (see [35], for example).

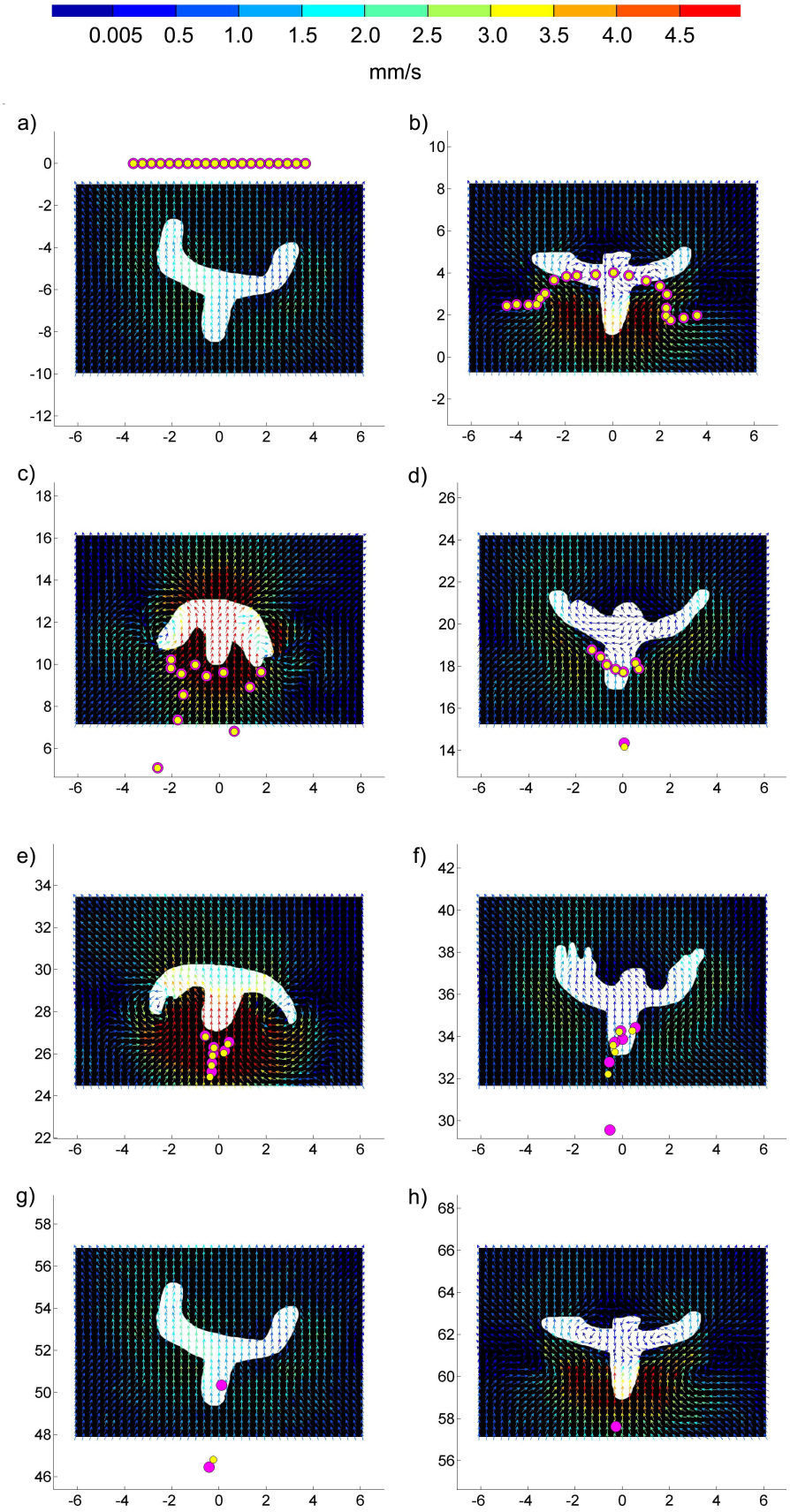

Figure 5.5: Velocity field time series showing fluid particle advection due to the vertical migration of a single ephyrae. Simulated fluid particles are color coded according to the value of the buoyancy frequency used to compute its position: $N = 0$ s^{-1} (purple) and $N = 10^{-3}$ s^{-1} (yellow). The time lapse between images is $\Delta t = 2$ s. All spatial units are in mm.

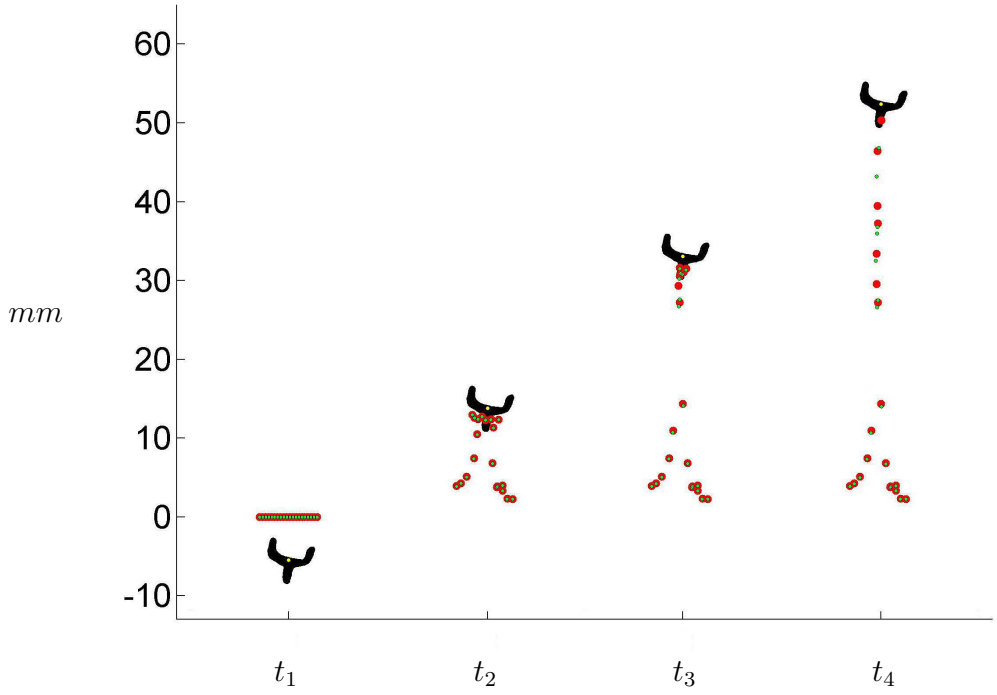

Figure 5.6: Advection of a fluid particle row during the vertical migration of a single ephyrae. The instantaneous position of the simulated fluid particle row is shown for the following times: $t_1 = 0$ s, $t_2 = 4.7$ s, $t_3 = 9.37$ s, and $t_4 = 14.03$ s. Simulated fluid particles are color coded according to the value of the buoyancy frequency used to compute its position: $N = 0\,\mathrm{s}^{-1}$ (red) and $N = 10^{-3}\,\mathrm{s}^{-1}$ (green).

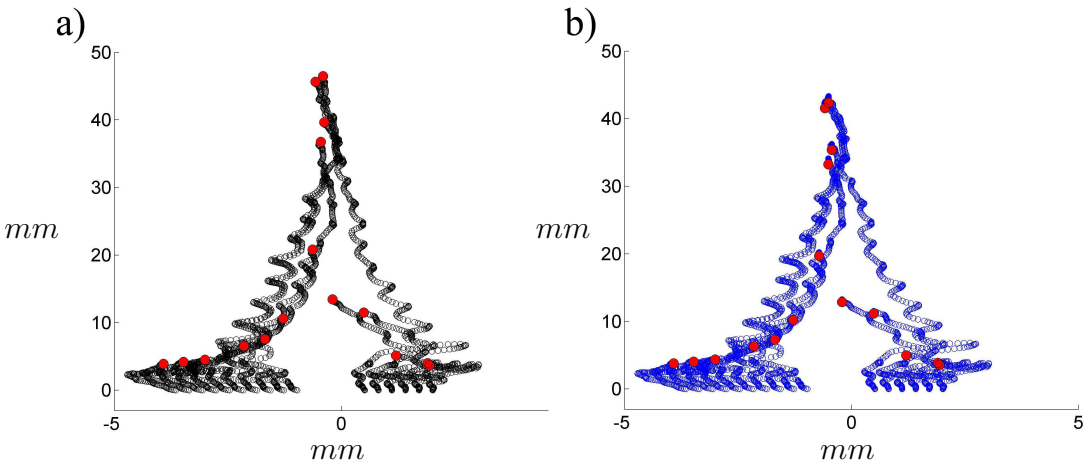

Figure 5.7: Fluid particle trajectories due to the vertical migration of a single ephyrae in non-stratified (a) and stratified fluid (b). The final positions of the fluid particles are denoted with red. Note that only a fraction of all simulated fluid particle trajectories were plotted.

The drift volume, defined as the volume of fluid contained between the surface

coincident with the initial equilibrium position of the tracked fluid particle batch and the one delineated by the final position of these particles after the jellyfish has swum past this material line (see §1.3.2), was computed for the case of a single swimmer according to the following expression [19]:

$$D_f = \int_0^{2\pi} \int_0^R \mathbf{X}\, r dr d\theta \ , \tag{5.3}$$

where $\mathbf{X}$ is defined by the position of the simulated fluid particles at any given time instant and R is set by the instantaneous horizontal position of a particle with respect to the initialized position of the center of the particle row.

The non-dimensionalized drift volume is shown in Figure 5.8 as a function of time in non-stratified as well as stratified fluid. The drift volume was normalized using the volume of the jellyfish (V_{jelly}), which was approximated as the volume of a sphere using the organism body diameter (D) defined in Figure 5.4:

$$D^* = \frac{D_f}{V_{jelly}} = \frac{D_f}{4/3\pi(D/2)^3} \ , \tag{5.4}$$

while time was non-dimensionalized using the average swimming speed of the organism ($U = 4.15$ mm/s), computed using the displacement of the centroid of the organism:

$$t^* = \frac{tU}{D/2} \ . \tag{5.5}$$

Initially, the drift volume increased linearly with time as the organism migrated vertically, exceeding the volume of the jellyfish within just a few strokes. The spikes in the curves are due to the rearrangement of the particles in the horizontal direction as they were trapped closer to the bell. The total volume drifted by the organism during vertical migration was 2.34 times greater than the volume of the organism. In the presence of stratification, the drift volume decreased over time due to the restoring action of buoyancy once this maximum value was attained and the simulated particles were no longer dragged by the organism. Thus, for a single swimmer migrating upwards, the effect of stratification is initially minimal and does not inhibit fluid transport.

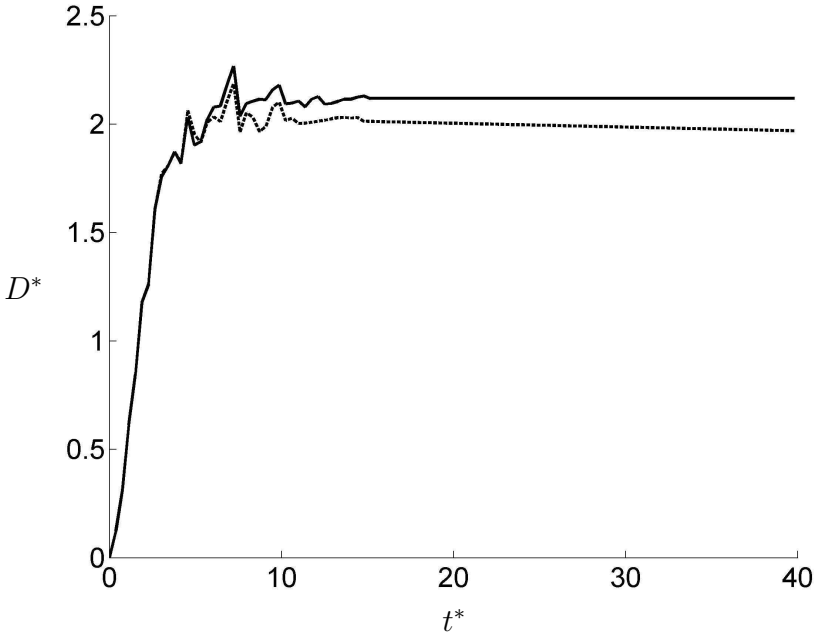

Figure 5.8: Drift volume for a single swimmer migrating upwards. The non-dimensionalized drift volume D^* is shown as a function of dimensionless time t^* both in a non-stratified (solid line) and stratified fluid (dashed line).

Vertical fluid transport due to the vertical migration of multiple swimmers was quantified in terms of the mean drift of the fluid particle batch in the vertical direction, which is given by the vertical displacement of the center of mass of the group of particles [44]:

$$M_{x_2}(t) = \frac{1}{N}\sum_{i=1}^{N}(x_{2_i}(t) - x_{2_i}(0)) \ , \tag{5.6}$$

where N is the number of particles in the initially horizontal batch of equidistant fluid particles, $x_{2_i}(t)$ is the vertical position of a given particle i at a given instant and $x_{2_i}(0)$ is its equilibrium position.

Although less evident in the case of a single swimmer than in the cases presented below, the wake structure has a notable effect on vertical fluid transport. The main difference between fluid transport due to a real swimmer and that due to a solid sphere in potential flow is the final shape of the drift volume due to the near-field flow of the swimmer. In the case of *Aurelia aurita*, the production of

two vortex rings near its bell traps particles in this near-body region and carries them on length scales greater than the jellyfish body diameter. As a result of the continuous production of vortex rings during propulsion, fluid particles close to the organism are horizontally drawn to the center of the ephyrae. In the case of a solid sphere in potential flow, the absence of vortex rings in the wake of the translating object results in a wider drift fluid column. As will be shown below, this has immediate consequences on fluid transport due to a migrating group of organisms with a given configuration.

The vertical fluid displacement of the centroid of the simulated particle row is shown in Figure 5.9 as a function of the distance travelled by the first swimmer in the aggregation for the three different configurations described in §5.2.3, both in stratified and non-stratified fluid. The vertical spacing between organisms was $8.5D$, which was the number of travel diameters needed by a single vertically migrating organism in non-stratified fluid to achieve maximum fluid transport. Furthermore, the horizontal spacing between consecutive organisms in the two-column and three-column staggered configurations was set to $1/2D$ to match the spacing between translating spheres in the potential flow model by Dabiri [12]. The fluid particles that became entrained within the wake region close to the bell and therefore boundlessly advected as the organism migrated upwards were not included in this calculation nor in the statistics presented below.

As expected, the centroid of the particle batch was advected on much greater length scales by the swimmer modeled implementing experimental velocimetry data than by the flow field generated via the inviscid model used in [12]. A striking aspect, however, is the fact that the inline configuration was the case for which vertical fluid transport was greatest, followed by the two-column staggered case. The displacement of the centroid of the simulated particles for the three-column staggered case yielded almost half of the vertical displacement than that achieved by the inline configuration, contrary to the predictions made from the potential flow model results in [12]. The reason for this discrepancy is the difference in swimming mode between the potential flow model swimmer and the ephyrae *Au-*

relia aurita.

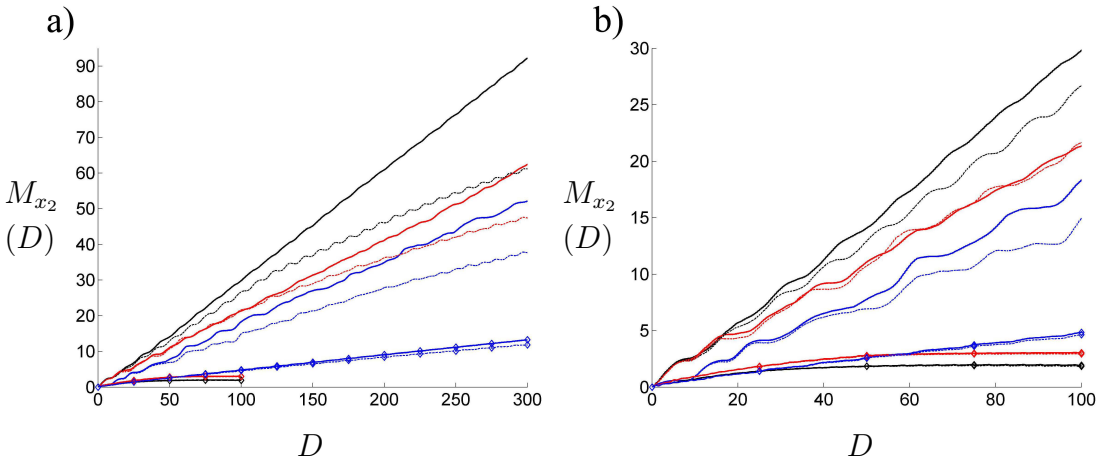

Figure 5.9: Mean vertical drift for different configurations in non-stratified and stratified fluid. The vertical displacement of the centroid of the particle batch is shown as a function of the distance travelled by the first swimmer (in body diameters D) in the aggregation for three different configurations: inline (black), two-column (red) and three-column staggered (blue), both in non-stratified (bold lines) and stratified fluid (solid lines). The results by [12] are reproduced for the same cases (lines with markers). Panel (b) zooms in on the first hundred diameters of travel from panel (a), which shows the full extent of the simulation.

As shown by recent numerical simulations of single swimmers using a similar method than the one presented in this chapter [35], animal morphology and therefore swimming mode has a direct impact on the geometry of the drift volume as well as on its temporal evolution. A swimmer modeled as a rigid sphere translating vertically in potential flow drags fluid with it as it moves forward due to the pressure field around it [37]. In the case of a real self-propelled swimmer, a drift volume is generated under the same principle, but it is also greatly influenced by the dynamics at its wake. In the case of the ephyrae *Aurelia aurita*, propulsion is acquired via the synchronous contraction of the body, which results in the generation of two vortex rings in its wake at each propulsive cycle (Figure 5.3). Fluid is then consequently drawn towards the bell and trapped in this region, before being advected in the same direction as the jellyfish. As a result, there is a high concentration of fluid particles close to the central axis of the swimmer, instead of by its sides, as is the case for the model swimmer in potential flow.

The distribution of the simulated row of fluid particles is shown as a series of snapshots at different time steps during the simulation in Figure 5.10. From these images, it can be seen that vertical fluid transport is maximized as the spread of the particle batch in the horizontal direction is minimized. As the migration progresses, fluid is drawn towards the central axis of the organism in contact with the particle batch during vertical advection, leaving a trail of particles close to this position. Thus, configurations with alternating organisms at different horizontal positions result in a more horizontally spread out particle distribution, with lesser total vertical advection. The cases with intermediate fluid stratification demonstrate the effect of buoyancy, which acts only in the vertical direction. Thus, the distribution of the particle batch in this case is analogous to the one in non-stratified fluid, but at a lower vertical position.

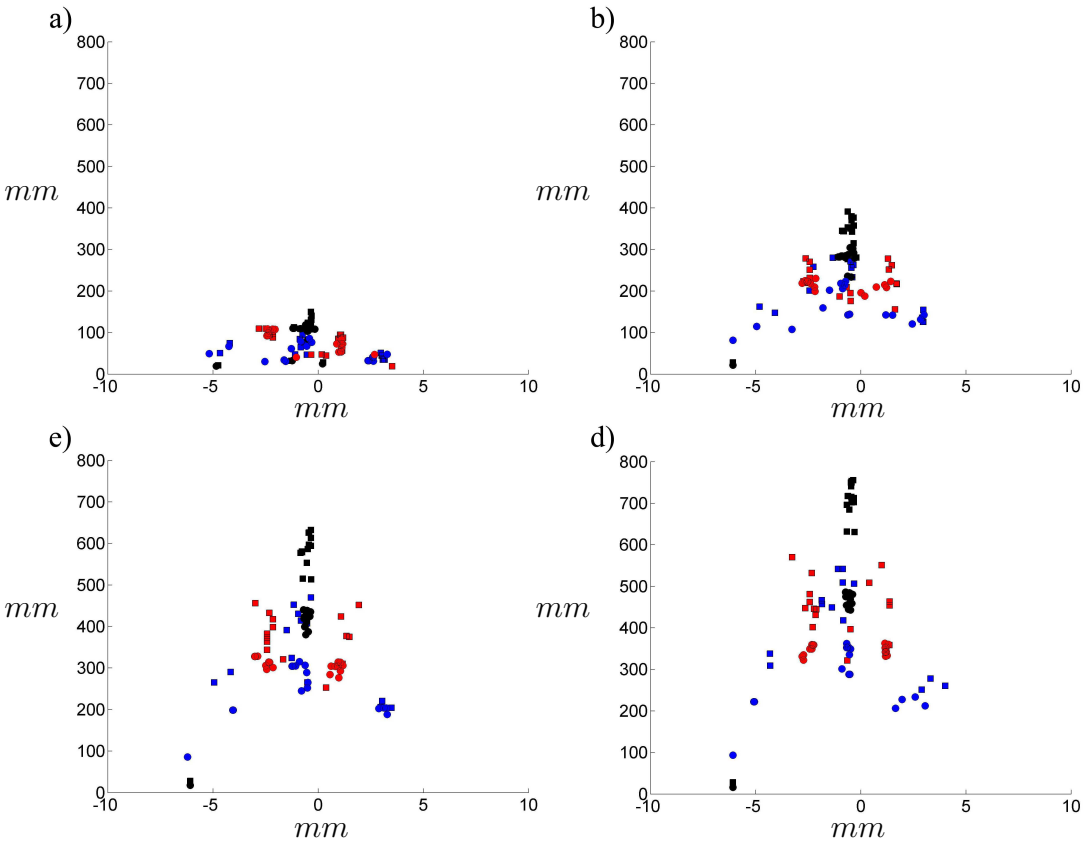

Figure 5.10: Particle distribution during vertical migration in non-stratified and stratified fluid. A series of snapshots showing the positions of the simulated fluid particle row is presented in panels (a) to (d) for times at which the first swimmer in the aggregation has travelled 50, 150, 250, and 300 body diameters, respectively, for an inline (black), two-column (red), and three-column (blue) staggered configurations in non-stratified (squares) and stratified fluid (circles).

The horizontal spread about the center of mass of the fluid particle batch at its equilibrium position was computed via the variance of the displacements in the horizontal direction over time [44]:

$$D_{x_1} = \frac{1}{N-1}\sum_{i=1}^{N}(x_{1_i}(t) - X_1 - M_{x_1}(t))^2 \ , \tag{5.7}$$

where X_1 is the position of the centroid of the fluid particle row at equilibrium, which is given by:

$$X_1 = \frac{1}{N}\sum_{i=1}^{N}(x_{1_i}(0)) \ , \tag{5.8}$$

and M_{x_1} is the mean horizontal drift of the particle batch from this position over time:

$$M_{x_1}(t) = \frac{1}{N}\sum_{i=1}^{N}(x_{1_i}(t) - X_1) \ . \tag{5.9}$$

The square root of this estimate is shown in Figure 5.11 for the three configurations studied in stratified and non-stratified fluid versus the distance travelled by the first swimmer in the aggregation. Particles outside the range $x_{1_i} \ \epsilon \ [-5, 5]$ were not taken into account in this calculation, in order to analyze the horizontal spread of the group of particles being advected with the organisms. Initially, the horizontal spread of the particle batch was set by the width of the particle row, which is the same for all animal configurations. As the migration progressed, however, the animal configuration that achieved the greatest vertical transport spread minimally in the horizontal direction, in agreement with the particle distributions presented in Figure 5.10. It is because of this horizontal spread that the two-column and three-column configurations did not achieve greater vertical fluid transport, in comparison with the inline configuration.

The effect of vertical inter-organism spacing on vertical fluid transport was tested for all animal configurations by reducing this distance from $8.5D$ to $4.25D$, while setting the number of organisms constant (see Table 5.1 for details). The mean vertical drift of the fluid particle batch in non-stratified fluid is shown for these

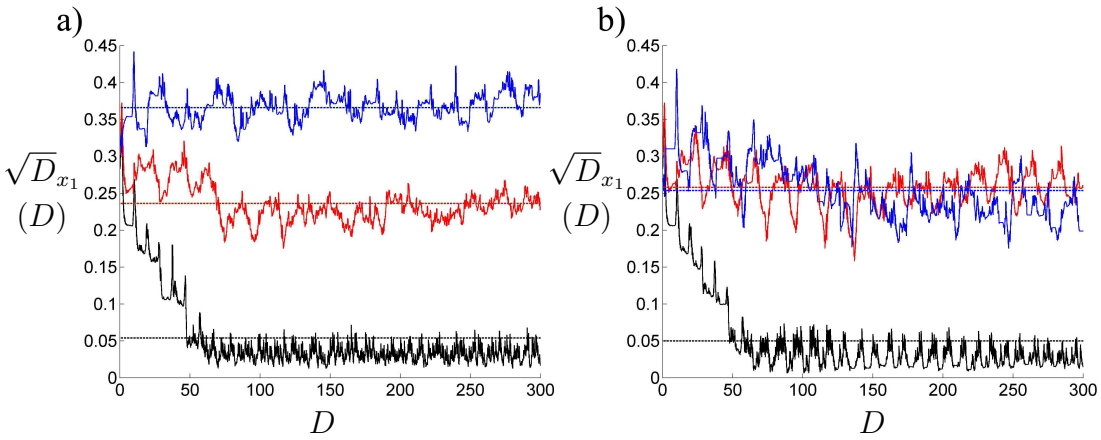

Figure 5.11: Horizontal spread of the particle batch in non-stratified and stratified fluid. The square root of the variance of the displacements with respect to the center of the particle batch at its equilibrium position (in body diameters) versus the body diameters travelled by the first swimmer in the aggregation is shown for non-stratified (a) and stratified fluid (b).

cases in Figure 5.12.

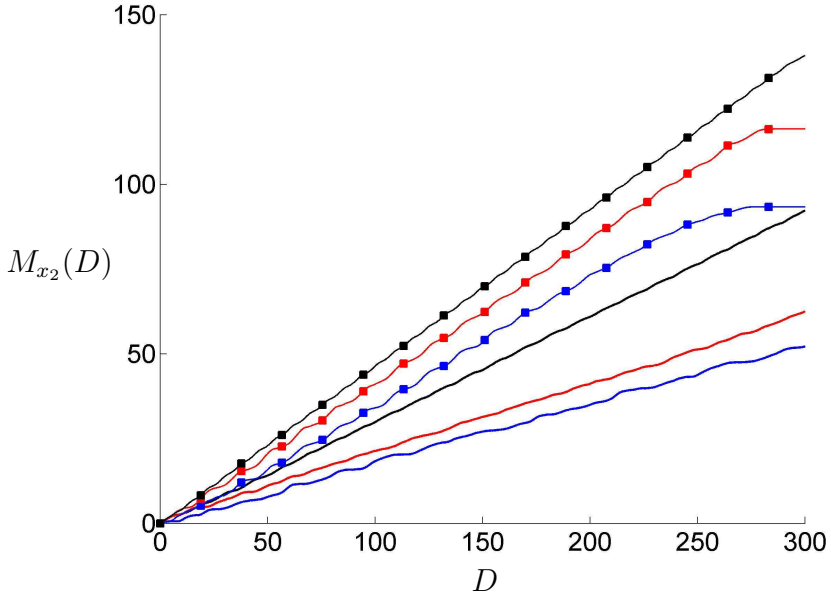

Figure 5.12: Mean vertical drift for all tested vertical inter-organism spacings in non-stratified fluid. The vertical displacement of the centroid of the particle batch (in body diameters) is shown with respect to the body diameters travelled by the first swimmer in the aggregation for a vertical inter-organism spacing of $8.5D$ (solid lines) and $4.25D$ (lines with markers) for aggregations with an inline (black), two-column (red), and three-column staggered (blue) configuration.

Overall, an increase in the mean vertical drift of the simulated fluid particles was

obtained when the vertical inter-organism spacing was reduced by 50%. This result is intuitive, since more organisms were allowed to interact with the particle batch over the same time interval. In this case, the two-column and three-column staggered configurations reached its maximum overturning length scale near the end of the simulation ($116D$ and $93.2D$, respectively).

A smaller vertical inter-organism spacing was also tested in stratified fluid. Additionally, the horizontal spacing between consecutive swimmers was also reduced by 50% from $1/2D$ to $1/4D$ for the aggregations with two-column and three-column staggered configurations. The results from all the experiments done considering a stratified fluid are presented in Figure 5.13. Similar to the results in non-stratified fluid, reducing the vertical spacing between successive swimmers resulted in greater vertical fluid transport. Furthermore, a reduction in the horizontal spacing between swimmers yielded even greater vertical transport, compared to cases with bigger spacings within the same time lapse.

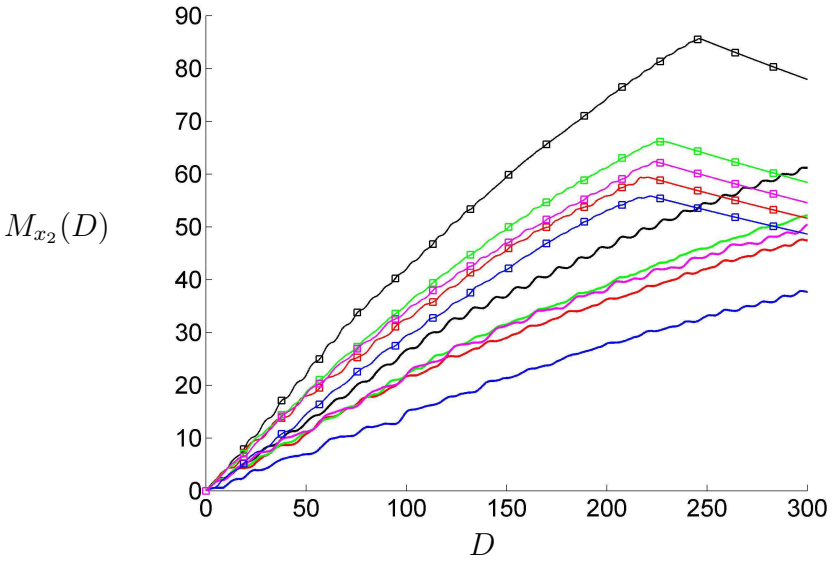

Figure 5.13: Mean vertical drift for all tested vertical inter-organism spacings in stratified fluid. The vertical displacement of the centroid of the particle batch (in body diameters) is shown with respect to the body diameters travelled by the first swimmer in the aggregation for a vertical inter-organism spacing of $8.5D$ (solid lines) and $4.25D$ (lines with markers) for the following configurations: inline (black), two-column staggered with horizontal inter-organism spacing of $1/2D$ (red) and $1/4D$ (green), three-column staggered with horizontal inter-organism spacing of $1/2D$ (blue) and $1/4D$ (magenta).

For the cases with reduced vertical distance between swimmers, maximum overturning length scales ranging from 56 up to 86 body diameters were reached within less than 300 body diameters of travel. After maximum vertical transport was achieved and no more organisms were left to interact with the batch, the fluid particles were dragged downwards due to restratification. In the case of aggregations with large vertical spacing between organisms, maximum fluid transport was not attained during the duration of the simulation.

The horizontal spread of the fluid particle batch for the cases in Figures 5.12 and 5.13 are shown in Figure 5.14, along with a series of snapshots showing the fluid particle positions at different time steps during vertical migration in Figures 5.15 and 5.16, for a vertical inter-organism spacing of $8.5D$ and $4.25D$, respectively.

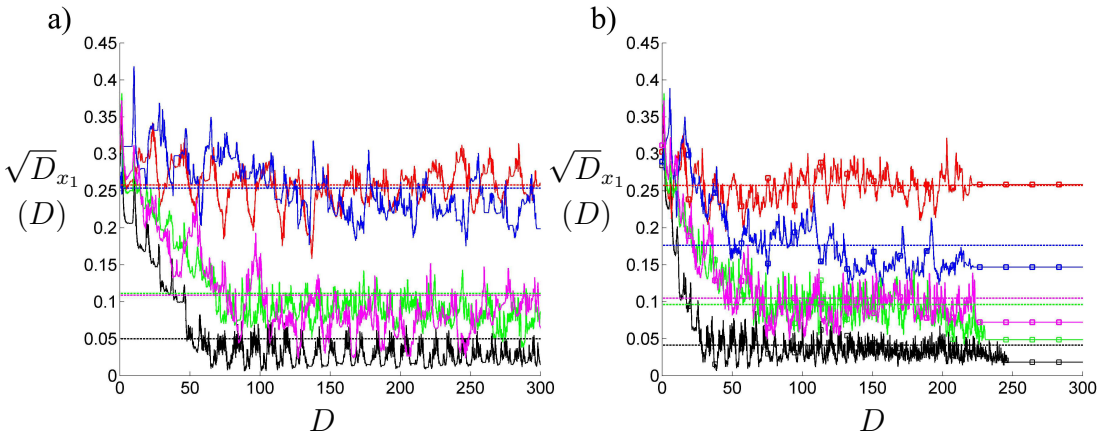

Figure 5.14: Horizontal spread of the particle batch in stratified fluid. The square root of the variance of the displacements with respect to the center of the particle batch at its equilibrium position (in body diameters) versus the body diameters travelled by the first swimmer in the aggregation is shown for aggregations with vertical spacing of $8.5D$ between swimmers (a) and $4.25D$ between swimmers (b).

As seen in Figure 5.14, reducing the vertical spacing between organisms did not have an important effect on the horizontal spread of the fluid particle batch. On the other hand, reducing the horizontal spacing between successive swimmers decreases the span of the advected particle row considerably, thereby increasing vertical fluid transport.

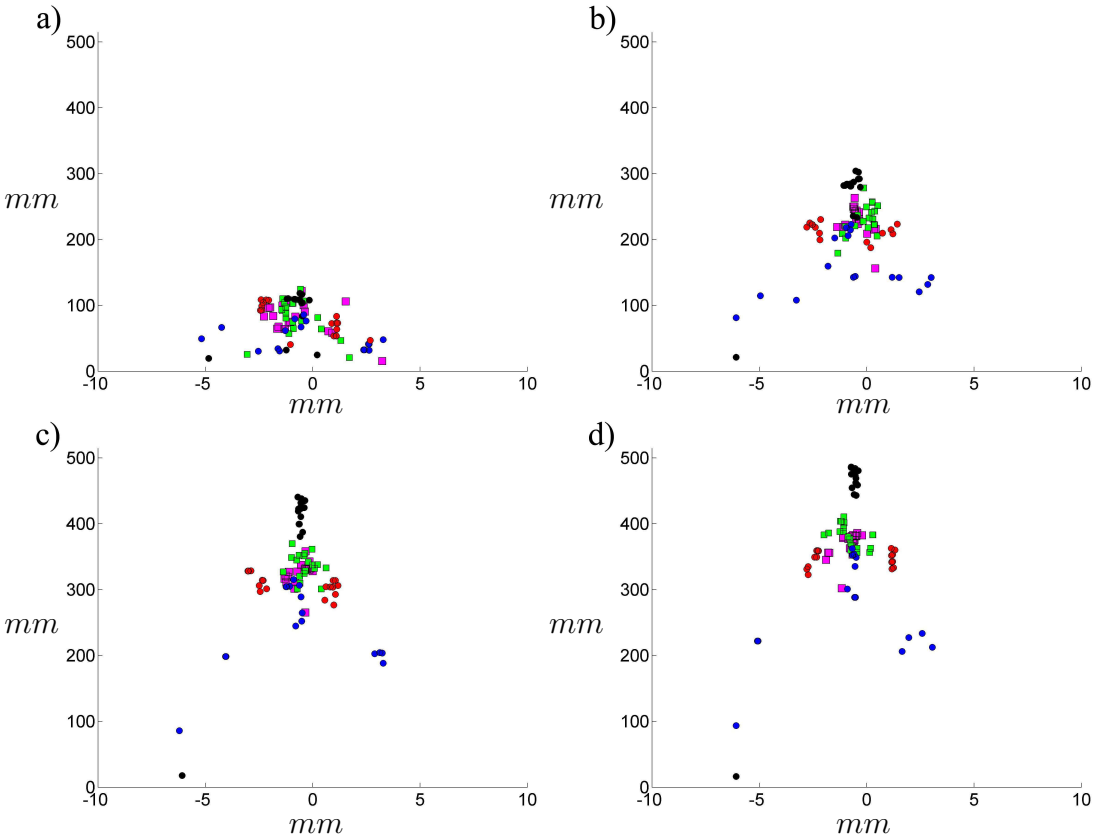

Figure 5.15: Particle distribution during vertical migration in stratified fluid for aggregations with vertical spacing of $8.5D$ between swimmers. Snapshots showing the positions of the particle batch is presented in panels (a) to (d) for 50, 150, 250, and 300 body diameters travelled, respectively, for the following configurations: inline (black), two-column staggered with horizontal spacing of $1/2D$ (red) and $1.4D$ (green) between swimmers, and three-column staggered with horizontal spacing of $1/2D$ (blue) and $1.4D$ (magenta) between swimmers.

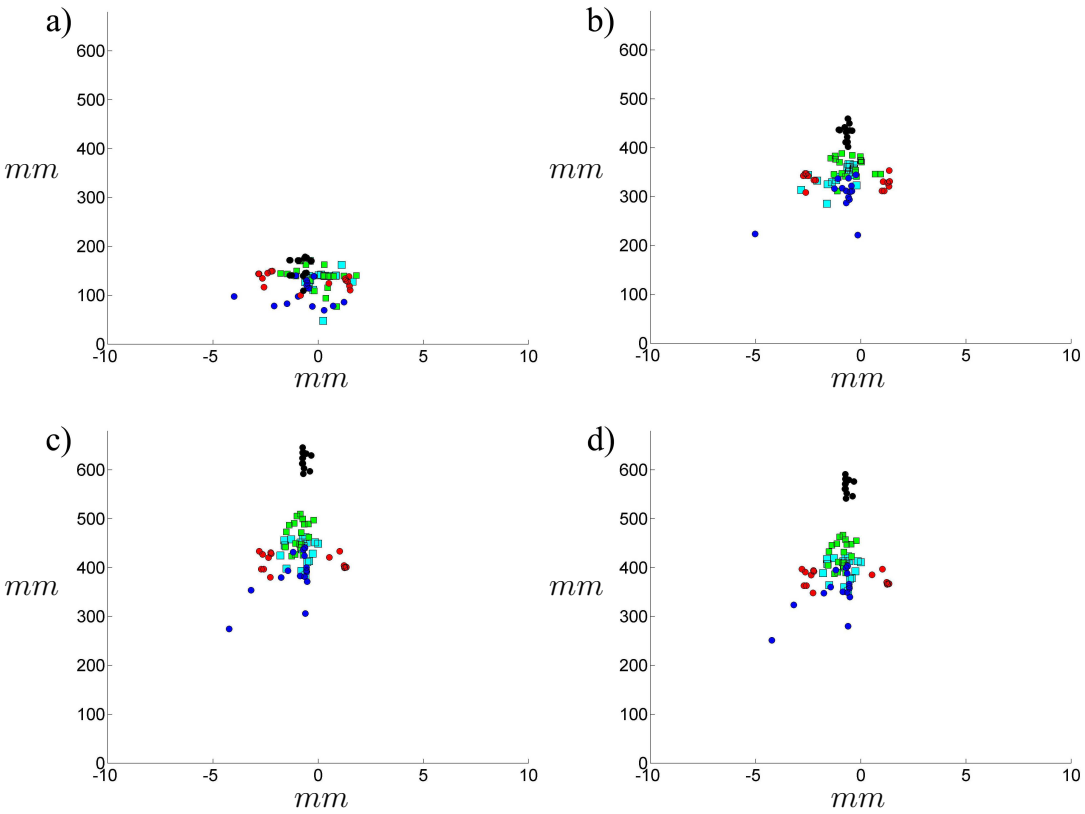

Figure 5.16: Particle distribution during vertical migration in stratified fluid for aggregations with vertical spacing of $4.25D$ between swimmers. Snapshots showing the positions of the particle batch is presented in panels (a) to (d) for 50, 150, 250, and 300 body diameters travelled, respectively, for the following configurations: inline (black), two-column staggered with horizontal spacing of $1/2D$ (red) and $1.4D$ (green) between swimmers, and three-column staggered with horizontal spacing of $1/2D$ (blue) and $1.4D$ (magenta) between swimmers.

Finally, the particle statistics derived above were extended to quantify mixing via the calculation of an absolute dispersion coefficient for the cases with fluid stratification, from which an effective vertical diffusivity K was estimated [44]:

$$D_{x_2} = \frac{1}{N-1}\sum_{i=1}^{N}(x_{2_i}(t) - x_{2_i}(0))^2 \quad , \tag{5.10}$$

This quantity was computed for all the tested configurations in stratified fluid (Figure 5.17). In all the cases, the absolute vertical dispersion was observed to have a parabolic behavior within the first 200 s, followed by a linear growth until maximum vertical fluid transport was reached.

By definition, the absolute diffusivity is given by half the time derivative of the absolute vertical dispersion [44]. Thus, an effective vertical diffusivity can be derived for each configuration by estimating the slope of the linear portion of each curve. The results are summarized in Table 5.3.

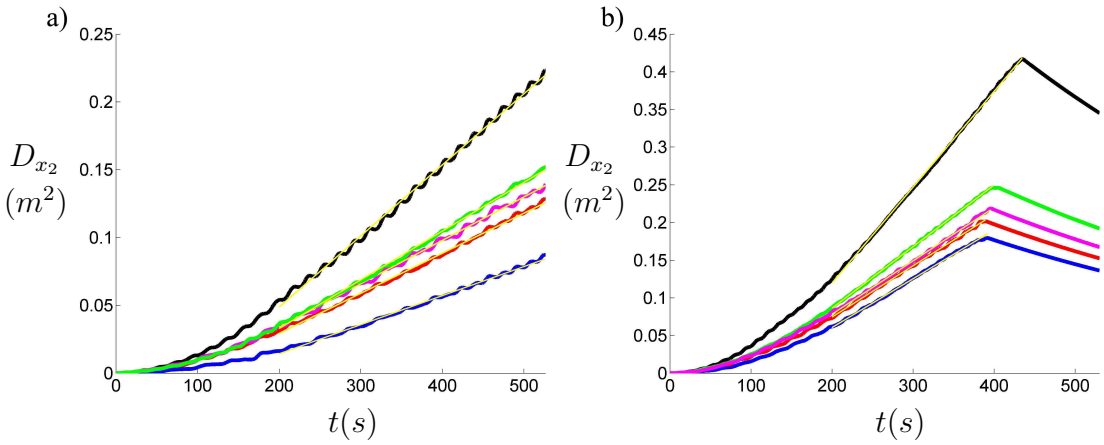

Figure 5.17: Absolute vertical dispersion for different configurations in stratified fluid. The absolute vertical dispersion is shown as a function of time for aggregations with a vertical inter-organism spacing of $8.5D$ (a) and $4.25D$ (b) in stratified fluid. The tested configurations are inline (black), two-column staggered with horizontal spacing of $1/2D$ (red) and $1.4D$ (green) between swimmers, and three-column staggered with horizontal spacing of $1/2D$ (blue) and $1.4D$ (magenta) between swimmers. The linear fit used to calculate the slope of each curve is shown as a yellow line.

Configuration	Horizontal inter-organism spacing	Vertical inter-organism spacing	Vertical Diffusivity (m^2/s)
Inline	-	$8.5D$	2.6×10^{-4}
Inline	-	$4.25D$	6.3×10^{-4}
Two-column staggered	$1/2D$	$8.5D$	1.5×10^{-4}
Two-column staggered	$1/2D$	$4.25D$	3.4×10^{-4}
Two-column staggered	$1/4D$	$8.5D$	1.8×10^{-4}
Two-column staggered	$1/4D$	$4.25D$	4.1×10^{-4}
Three-columnstaggered	$1/2D$	$8.5D$	1.1×10^{-4}
Three-columnstaggered	$1/2D$	$4.25D$	3.2×10^{-4}
Three-columnstaggered	$1/4D$	$8.5D$	1.6×10^{-4}
Three-columnstaggered	$1/4D$	$4.25D$	3.5×10^{-4}

Table 5.2: Vertical eddy diffusivities for migrations in stratified fluid.

The estimated vertical eddy diffusivity was in the order of $O(10^{-4})$ m^2s^{-1} for all the configurations analyzed in this chapter, which is three orders of magnitude greater than the thermal diffusivity coefficient and five orders of magnitude greater than the diffusivity of salt in seawater [93]. The effect of animal configuration has a noticeable effect on the magnitude of the diffusivity coefficient, with the highest value achieved by the inline configuration. Furthermore, reducing the inter-organism spacing vertically has a greater impact on vertical mixing than doing so horizontally. Nonetheless, the horizontal distance in between successive organisms does have an effect on the amount of fluid being drifted and mixed vertically.

The computed values of vertical diffusivity are in agreement with previous estimates based on in situ measurements of fluid transport by a single self-propelled jellyfish [37] and with predictions by Dabiri [12], based on earlier studies of fluid dispersion due to vortex trapping behind arrays of solid cylinders [103]. Moreover, they fall within the range of computed diffusivities for DVM of zooplankton aggregations (Chapter 4).

5.4 Discussion

The experimental study presented thus far was complemented with the development of a numerical method that provides a quick and inexpensive quantitative approach to pin down potential biomixers within the numerous oceanic species that undergo DVM. By implementing velocimetry data of single self-propelled swimmers, obtained either in situ or in the laboratory, fluid transport and vertical mixing can be assessed via Lagrangian statistics in the limit of dilute aggregations.

In the case study presented in this chapter, aggregations of the ephyrae *Aurelia aurita* were simulated under different configurations to test the effects of the structure of a migrating aggregation on vertical fluid transport and mixing. It was observed that both the vertical and horizontal inter-organism spacings influence the distribution of the fluid particles being drifted by the organism and thus affect

vertical fluid transport and the amount of mixing achieved by an aggregation. Comparison of the computed mean vertical fluid drift with that of previous fluid transport studies that modeled self-propelled swimmers as solid spheres in potential flow [12] highlighted the influence that the swimming mode and near-field flow have on vertical fluid transport.

The interaction between the fluid particles and the wake of the organism during vertical migration dictated the ideal configuration for maximum fluid transport. In the case of a vertically migrating array of solid spheres in potential flow, particles end up distributed far from the centroid of the migrating organisms. Hence, spreading the swimmers horizontally increases the amount of fluid transported upwards, as less particles are left behind. In the model presented here, however, it was observed that fluid particles are entrained within the bell of the ephyrae by the generated vortex rings and dragged upwards as the organism migrates. Thus, the particles end up being distributed about the centroid of the organism and a staggered configuration does not result in enhanced vertical fluid transport, compared to a simple inline formation.

Vertical mixing was estimated via a vertical effective diffusivity derived from absolute dispersion computations. All the tested configurations resulted in an effective diffusivity in the order of $O(10^{-4})$ m^2s^{-1}, which falls within the estimated range in Chapter 4 for vertically migrating organisms undergoing DVM in the ocean. This suggests that even in very dilute aggregations, where the velocity fields of neighboring organisms do not interact with each other, vertically migrating organisms have the potential to transport and mix fluid across isopycnals. The question is whether or not these results translate to other species of zooplankton that undergo DVM, such as krill and copepods.

Chapter 6

Conclusions and Outlook

The present investigation has focused on the study of animal-fluid interactions during vertical migration of zooplankton aggregations. The notion of biogenic mixing as a potential source for vertical ocean mixing is relatively new, and research in this field has followed a line of thought from the simple case of an individual swimmer to coordinated groups of organisms. Prior to the present research activity, the available fluid transport and mixing mechanisms for individual swimmers have already been well characterized, prompting the analysis of collective effects. The main results from Chapters 3, 4, and 5 are listed in the next section, the most important one being that hydrodynamic interactions between neighboring swimmers during vertical migration result in large energetic structures that can efficiently mix fluid across a strong stable stratification. Thus, our results support the hypothesis that biogenic mixing could have an important contribution to upper ocean dynamics as well as local transport. As part of a continuum, this study raises new issues and motivates further investigation of this process through the incorporation of new parameters. These details alongside recommendations for future endeavors in this area are given in this chapter.

6.1 Summary of Results

As outlined in Chapter 2, a new experimental system was developed to induce and control vertical migrations of aggregations of small swimming organisms in the laboratory while simultaneously measuring the resulting flow field via PIV. Collective animal motion was triggered by influencing the phototactic capabilities

of *A. salina*, which is a common trait in many species of zooplankton that undergo DVM in the ocean. Thus, we expect that this device will serve as a new tool to study fluid dynamic processes related to collective motion in the laboratory. Furthermore, we envision the use of laser control in future field studies to facilitate the location of organisms within the water column and prompt vertical migration at a specific location.

Biogenic mixing due to DVM was studied in increasingly complex scenarios. In Chapter 3, PIV measurements during vertical migration were done in non-stratified fluid to understand the effect of hydrodynamic interactions between neighboring swimmers during collective vertical motion on fluid transport. Additional control observations were done with a single organism as well, which confirmed the effect of swimming mode on Darwinian drift. It was found that near-field fluid transport during vertical propulsion of *A. salina* varied between its ventral and dorsal sides, which resulted in the development of a quasi-steady jet that propagated opposite to the direction of animal motion as well as a weak upward drift within the dorsal side of the organism. The interplay between these counteracting flows resulted in net downward fluid transport over the duration of an entire swimming cycle, which agrees with experimental observations of marine crustaceans that propel via metachronal swimming and undergo DVM.

During vertical collective motion, this feature dominated the generated flow field: the interaction between the hydrodynamic trails behind neighboring swimmers resulted in the development of a strong downward flow that diverged over time. Further analysis was achieved via a Reynolds decomposition of the measured velocity field. It was found that the fluctuating velocity component at any given position of the measurement field followed a bimodal distribution characterized by long tails, suggesting that the important interactions occurred between well-separated scales that enhance the formation of large scale structures, which in turn introduce intermittency into the flow. This result agreed with the shape of the vertical component of the measured velocity spectrum with respect to vertical wavenumber, which displayed a κ^{-1} power law. By neglecting the effect of non-

linear terms in the momentum equations, which are responsible for the transfer of energy between similar-sized scales down to the Kolmogorov scale, the observed relationship between kinetic energy and dissipation flux was found via dimensional analysis of the important flow parameters. As a result of the non-local nature of the flow, an inverse energetic pathway is established that transfers energy from the small scales at which each organism introduces kinetic energy into the flow to larger scales via the onset of a Kelvin-Helmholtz instability.

As described in Chapter 4, this shear-dominated energy transfer mechanism that involves large and small scales was also observed in the presence of a stable stratification. It was found that vertical fluid transport was hindered by the strength of the stratification; thus, attenuating the far-field flow of the vertically migrating aggregation with respect to the non-stratified case. However, the evolution of the flow exhibited the same dynamics: non-local interactions dominated over local ones and an inverse cascade was available to distribute energy within scales larger than the size of the organisms. Inspection of the raw PIV images showed that the size of the large scale features formed in stratified conditions are at least of the same order of magnitude as the corresponding Ozmidov scale. Therefore, the generated overturns are influenced by buoyancy effects and have the ability to irreversibly mix the vertical density structure of the water column.

Estimation of the mixing efficiency was done following an energy balance approach. Given that the same experimental conditions were tested in non-stratified as well as in stratified fluids, energy production and the buoyancy flux can be derived from the kinetic energy dissipation rate of the corresponding velocity spectra. Our results indicate that more than half of the kinetic energy introduced by the swimming organisms is converted to background potential energy. Based on our observations and the value of the efficiency, we hypothesize that the shear-dominated flow triggers a Rayleigh-Taylor instability through which density overturns are achieved in the regions adjacent to the migrating aggregation.

As mentioned at the beginning of Chapter 4, the strength of the stratification that

we were able to experimentally impose is at least an order of magnitude greater than the one corresponding to oceanic regions in which DVM occurs. Therefore, we expect that our observations mark a lower bound on fluid transport, and therefore mixing, in the ocean. Furthermore, we hypothesize that the described hydrodynamic processes that trigger the development of a Rayleigh-Taylor instability could account for the large-scale density overturns that have been reported near vertically migrating aggregations of krill in coastal regions [42].

In addition to the experimentally acquired estimates of vertical fluid transport and mixing due to DVM, a numerical method that incorporates experimental velocimetry data was devised to broaden the parameter range of the laboratory studies, as detailed in Chapter 5. The main advantage of this technique is that fluid transport and mixing due to DVM can be analyzed in weaker stratification levels than those achieved in the laboratory. Furthermore, it provides a simple and inexpensive scheme to assess the relevance of numerous species regarding biogenic induced mixing.

In Chapter 5, this numerical method was used to investigate the effect of animal configuration within a migrating aggregation on vertical fluid transport and mixing during DVM. Our results agree with previous numerical studies stressing out the need to include the near-field flow of the organisms to correctly estimate the relevance of biogenic mixing [12], [36], [35]. By using available laboratory data of the ephyrae *Aurelia aurita*, it was observed that even in the limit of dilute aggregations, vertically migrating organisms can transport fluid on length scales much greater than the body length of individual swimmers, resulting in high values of vertical diffusion coefficients. These estimates agree with in situ measurements of fluid transport by self-propelled jellyfish and proposed vertical eddy diffusivities [37].

6.2 Contribution to Ocean Processes

The results summarized in the last section support the hypothesis that collective vertical motion of small swimming organisms can induce efficient vertical mixing and nutrient transport in a stably stratified ocean. The ability of vertically migrating aggregations to generate large scale energetic structures, despite the stability of the density stratification, suggests that their contribution in locally redistributing properties and nutrients within their ecosystem is not negligible. Furthermore, DVM is a biological process that occurs regularly within a vast geographical domain spanning coastal as well as open ocean regions in the Pacific, Atlantic and Indian oceans [7], highlighting its potential to have a global impact on upper ocean dynamics as well as the carbon and nutrient ocean cycles.

As discussed in Chapter 1, the physical trigger for DVM is yet to be determined, however recent studies show a strong correlation between these events and oxygen concentration in the water column [7]. In fact, a two-decade-long compilation of acoustic measurements by Bianchi et al [7] suggests that organisms tend to migrate from well ventilated near-surface regions in the mixed layer down to oxygen minimum zones within the pycnocline at sunrise. This supports the hypothesis that organisms undergo DVM as a response against predators, which are normally larger organisms that cannot sustain prolonged swimming patterns in deeper ocean regions with low oxygen concentration. At sunset, once the risk of visual predation is low, organisms migrate to near-surface waters to feed and possibly fulfill their oxygen requirements.

By translating back and forth between regions where the stable vertical stratification impedes vertical transport and the near-surface mixed layer, DVM of small organisms not only have the potential to efficiently mix properties and nutrients across adjacent isopycnals, but also to transport oxygen, carbon and energy across these well separated regions.

The observed variability in the rate of kinetic energy dissipation and hence eddy diffusivities pertaining to biogenic mixing imposes the next challenge of mapping

its intensity to precisely account for the impact of vertical migrations on local and global ocean processes. Our study motivates further use of laser control and the present laboratory methodology to determine the efficiency of migrating aggregations under different fluid conditions, such as double diffusion and background turbulence, to better understand this biogenic process within different oceanic environments.

6.3 Guidelines for Future Work

During the course of this investigation, several questions arose that could have important implications on our findings. These are briefly mentioned here, with the hope that future investigations will undertake some of the analysis.

As mentioned in Chapter 2, the laser-guidance system can be modified to address the effect of additional experimental parameters, provided that any light signal that is introduced is properly tuned with respect to the phototactic behavior of the test organisms. Regarding measurement techniques to analyze fluid transport and mixing, PIV was found to be best integrated with the animal guidance system, given that it does not require the light source to be within a specific wavelength. Commonly used methods in the literature, such as laser-induced fluorescence (LIF) and molecular tagging velocimetry (MTV), were considered. However, the excitation and fluorescence range of the corresponding tracers as well as the adverse reaction of the organisms towards these chemicals posed a major challenge. Additional preliminary tests using a technique closely related to PIV, particle image thermometry/velocimetry (PIT/V) suggested that successful implementation of this method would allow simultaneous temperature and velocity measurements within the field of view of the camera. The difficulty in this case lies in synchronizing the white light source needed for PIT/V with the camera and the guidance system such that the organisms are not able to perceive it. Furthermore, for small temperature differences the color contrast of the particle tracers is low, which could potentially compromise the accuracy of the measurements in the absence of effective image post-processing routines.

6.3.1 Effect of Inter-organism Spacing and Swimming Mode on Fluid Transport

In Chapter 5, it was demonstrated that the structure of an aggregation during vertical migration does have an effect on fluid transport and mixing. The challenge in analyzing this further is that there is no available information on animal configuration during DVM in the ocean. Scarce photographic data as well as recent glider measurements suggest that vertically migrating organisms are not uniformly distributed and do not behave in a coordinated motion as a school of fish would, for example [27], [25].

Nonetheless, the methodologies developed in this work can be used to further analyze fluid transport and mixing during DVM of aggregations with different animal configurations both experimentally and numerically. This can be done experimentally in the laboratory setup by changing the optic in front of the green laser sheet at the top of the water column. Organisms tend to distribute themselves within regions of positive phototaxis. Therefore, expanding this region by generating a wider sheet would result in a greater inter-organism spacing if the number of organisms is kept constant. On the other hand, the numerical model can be modified to explore random horizontal and/or vertical inter-organism spacing within a given range, for example.

The effect of swimming mode can be further investigated by using other organism species. *Daphnia* and *copepod* species constitute ideal case studies due to their abundance in relevant ocean regions. Moreover, these species also exhibit a phototactic response to a similar wavelength and intensity range as *A. salina*. A last suggestion regarding the exploration of additional species is to mimic the behavior of zooplankton aggregations in the ocean by introducing different sized organisms. According to acoustic measurements of vertical migrations of krill aggregations, smaller organisms lead the migration followed by larger ones. It is hypothesized that the reason behind this is that smaller organisms are less visible to predators;

however, its implications regarding nutrient transport and mixing is unknown [42].

Finally, experimentally derived estimates can be extended by studying a large variety of species via the numerical method presented in Chapter 5. Extensive velocimetry data of zooplankton has been acquired during the past decade, and this technique provides a simple approach to estimate the capability of a given species to efficiently transport and mix fluid vertically during DVM.

6.3.2 Effect of Simulating a Complete Migrating Cycle

In the present work, vertical migrations were induced from the bottom of the water column to the top. However, the laser-guidance system can be easily inverted to analyze the case of animal migration from top to bottom. Furthermore, a complete cycle can be studied by setting up an additional light source at the bottom that generates a green laser sheet that guides the organisms to the bottom of the tank. The issue is that in this case the effect of the walls is not necessarily negligible. Overturning motions due to animal migration would eventually reach the boundaries of the tank and its effect on fluid transport would have to be considered. As a back-of-the-envelope calculation, assuming that the magnitude of the velocity of the fluid is within the observed limit (in the order of $v \approx 0.001$ m/s), then it would take $t \approx 1.5$ min for the center of an eddy that is rolling out of the migration region to reach the wall of the tank.

6.3.3 Effect of Background Turbulence on Fluid Transport and Mixing

Increasingly complex scenarios can be interrogated by introducing additional systems to simulate natural conditions. The major difference between laboratory studies of animal propulsion and in situ measurements is due to the effect of background non-quiescent flow. Similarly, zooplankton organisms often encounter turbulent motions which have been hypothesized to have an important effect on biogenic transport processes.

It is unknown whether background turbulent flow inhibits or enhances mixing during vertical migration. Based on our observations, we hypothesize that its effect will depend on the turbulence generation method that is used to address this issue due to the restriction of strong stratification in laboratory studies. If, for example, turbulence is generated via an oscillating grid at the top or bottom of the column, its effect will depend on the ability of turbulent motions to penetrate the strong stable stratification. If, on the other hand, turbulence is introduced within the region of interest, its effect could be simulated as in oceanic conditions.

6.3.4 Potential Applications to Study Additional Fluid Configurations

Finally, the effect of double diffusion poses an interesting case. Estimates derived from our study are only applicable in regions where the density stratification is dominated by temperature changes. However, DVM can also be encountered in regions prone to double diffusion. A linear salinity gradient can be superimposed on the linear temperature gradient to analyze biogenic transport and mixing within these regions.

Based on the present experiments, one can foresee the employment of laser control in the field to validate laboratory results. Vertical migrations of zooplankton species can be triggered on-site by using laser signals, thereby potentially facilitating the collection of in situ flow measurements and acoustic data. The use of ocean gliders to reconstruct a three-dimensional view of an animal group has been recently demonstrated [25]. Thus, by integrating this oceanographic instrument, animal abundance as well as organism configuration during a migration event can be determined.

Appendix A

Temperature Sensors Wiring Diagram

Figure A.1 shows the wiring diagram of the electronic circuit used to acquire data through the Arduino board. Temperature data was acquired from each sensor by using the code provided in $http://arduino-info.wikispaces.com/Brick-Temperature-DS18B20\#Read\%20individual$. Each sensor has a unique identification number, which needs to be specified in order to gather data through the same bus in the Arduino board. This can be done by wiring only one sensor according to the diagram shown in Figure A.1 and the code provided in the webpage mentioned above. The addresses for the sensors used in this study are provided in Table A.1. The application CoolTerm can be downloaded to save the temperature data directly to a text file.

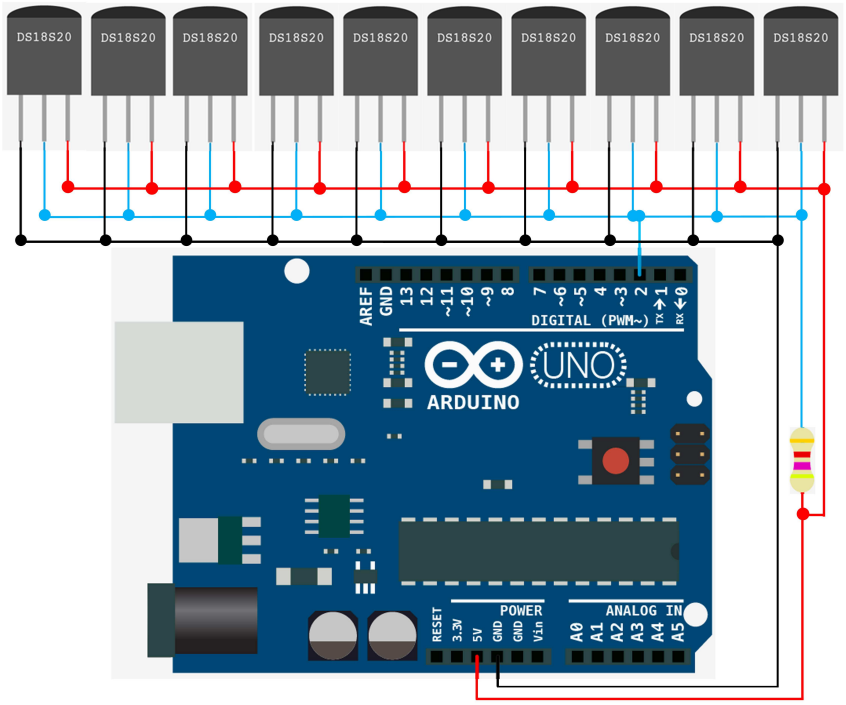

Figure A.1: Wiring diagram:DS18B20. The connections to plug 10 temperature sensors to the same data pin are shown in this diagram. This image was adapted from *bildr.org*.

Sensor Number	Device Address
1	0x28, 0xA2, 0x3B, 0x05, 0x06, 0x00, 0x00, 0x88
2	0x28, 0x45, 0x0A, 0x05, 0x06, 0x00, 0x00, 0x6D
3	0x28, 0xA7, 0x34, 0x06, 0x06, 0x00, 0x00, 0x84
4	0x28, 0x93, 0x13, 0x06, 0x06, 0x00, 0x00, 0x1C
5	0x28, 0x75, 0x17, 0x06, 0x06, 0x00, 0x00, 0x98
6	0x28, 0xFE, 0x28, 0x06, 0x06, 0x00, 0x00, 0x61
7	0x28, 0xFC, 0xF3, 0x05, 0x06, 0x00, 0x00, 0xA9
8	0x28, 0x4E, 0xDB, 0x05, 0x06, 0x00, 0x00, 0x06
9	0x28, 0xC8, 0x42, 0x06, 0x06, 0x00, 0x00, 0x92
10	0x28, 0x2F, 0x28, 0x06, 0x06, 0x00, 0x00, 0x92

Table A.1: Device addresses of DS18B20 temperature sensors.

Bibliography

[1] Th. J. Abatzopolous, J. A. Breadmore, J. S. Clegg, and P. Sorgeloos. *Artemia: Basic and applied biology*. Springer, 2002.

[2] R. J. Adrian and J. Westerweel. *Particle Image Velocimetry*. Cambridge University Press, 2011.

[3] S. Alben, K. Spears, S. Garth, D. Murphy, and J. Yen. Coordination of multiple appendages in drag-based swimming. *J R Soc Interface*, 7:1545–1557, 2010.

[4] A. M. Ardekani and R. Stocker. Stratlets: Low Reynolds number point-force solutions in a stratified fluid. *Phys Rev Lett*, 105:084502, 2010.

[5] G. K. Batchelor. Small-scale variation of convected quantities like temperature in a turbulent field. Part 1. General discussion and the case of small conductivity. *J Fluid Mech*, 5:113–133, 1959.

[6] P. Berge, M. Dubois, P. Manneville, and Y. Pomeau. Intermittency in Rayleigh-Benard convection. *J Physique*, 41:L–341–L–345, 1980.

[7] D. Bianchi, E. D. Galbraith, D. A. Carozza, K. A. S. Mislan, and C. A. Stock. Intensification of open-ocean oxygen depletion by vertically migrating animals. *Nature Geosci*, 6:545–548, 2013.

[8] I. A. Bolotnov, R. T. Lahey Jr., D. A. Drew, K. E. Jansen, and A. A. Oberai. Spectral analysis of turbulence based on the DNS of a channel flow. *Comput Fluids*, 39:640–655, 2010.

[9] D. L. Breitburg, B. C. Crump, J. O. Dabiri, and C. L. Gallegos. Ecosystem engineers in the pelagic realm: alteration of habitat by species ranging from microbes to jellyfish. *Int and Comp Biol*, 50(2):188–200, 2010.

[10] M. Calaf, M. Hultmark, H. J. Oldroyd, V. Simeonov, and M. B. Parlange. Coherent structures and the κ^{-1} spectral behaviour. *Phys Fluids*, 25:125107, 2013.

[11] J. H. Cohen and R. B. Forward Jr. Spectral sensitivity of vertically migrating marine copepods. *Biol Bull*, 203:307–314, 2002.

[12] J. O. Dabiri. Role of vertical migration in biogenic ocean mixing. *Geophys Res Lett*, 37(11):L11602, 2010.

[13] S. B. Dalziel, M. D. Patterson, C. P. Caulfield, and I. A. Coomaraswamy. Mixing efficiency in high-aspect-ratio Rayleigh-Taylor experiments. *Phys Fluids*, 20:065106, 2008.

[14] C. Darwin. Note on hydrodynamics. *Proc Camb Phil Soc*, 49:342–354, 1953.

[15] K. L. Denman and A. E. Gargett. Biological-physical interactions in the upper ocean: The role of vertical and small scale transport processes. *Ann Rev Fluid Mech*, 27:225–255, 1995.

[16] J. W. Dettman. *Introduction to Linear Algebra and Differential Equations*. Dover Publications, Inc., 1974.

[17] W. K. Dewar, R. J. Bingham, R. L. Iverson, D. P. Nowacek, L. C. St. Laurent, and P. H. Wiebe. Does the marine biosphere mix the ocean? *J Mar Res*, 64(4):541–561, 2006.

[18] I. Eames. The concept of drift and its application to multiphase and multi-body problems. *Phil Trans R Soc Lond A*, 361:2951–2965, 2003.

[19] I. Eames, S. E. Belcher, and J. C. R. Hunt. Drift, partial drift and Darwin's proposition. *J Fluid Mech*, 275:201–223, 1994.

[20] J. T. Enright and W. M. Hamner. Vertical diurnal migration and endogenous rhythmicity. *Science*, 157:937–941, 1967.

[21] FAO. Artemia spp, 2015.

[22] R. Ferrari. What goes down must come up. *Nature*, 513:179–180, 2014.

[23] G. H. Good and Z. Warhaft. On the probability distribution function of the velocity field and its derivative in mulit-scale turbulence. *Phys Fluids*, 23:095106, 2011.

[24] E. Van Gool and J. Rindelberg. What goes down must come up: symmetry in light-induced migration behaviour of *Daphnia*. *Hydrobiologia*, 491:301–307, 2003.

[25] D. Guihen, S. Fielding, E. J. Murphy, K. J. Heywood, and G. Griffiths. An assessment of the use of ocean gliders to undertake acoustic measurements of zooplankton: the distribution and density of Antarctic krill (*Euphausia superba*) in the Weddell Sea. *Limnol Oceanogr: Methods*, 12:373–389, 2014.

[26] J. Gulbrandsen. Artemia swarming – Mechanisms and suggested reasons. *J Plankton Res*, 23:659–669, 2001.

[27] W. M. Hamner and P. P. Hamner. Behavior of Antarctic krill (*Euphausia superba*): school, foraging, and antipredatory behavior. *Can J Fish Aquat Sci*, 57:192–202, 2000.

[28] F. Hersant, B. Dubrulle, and M. Wang. Non-locality of scale interactions in turbulent shear flows. *Proceedings of the 2000 Summer Program.*

[29] N. A. Hill and T. J. Pedley. Bioconvection. *Fluid Dyn Res*, 37:1–20, 2005.

[30] C. Ho and P. Huerre. Perturbed free shear layers. *Ann Rev Fluid Mech*, 16:365–424, 1984.

[31] M. E. Huntley and M. Zhou. Influence of animals on turbulence in the sea. *Mar Ecol Prog Ser*, 273:65–79, 2004.

[32] D. Ianson, G. Jackson, M. Angel, R. Lampitt, and A. Burd. Effect of net avoidance on estimates of diel vertical migration. *Limnol Oceaogr*, 49:2297–2303, 2004.

[33] Jayesh and Z. Warhaft. Probability distribution, conditional dissipation, and transport of passive temperature fluctuations in grid-generated turbulence. *Phys Fluids A*, 4:2292, 1992.

[34] J. Jimenez. The physics of wall turbulence. *Phys A*, 263:252–262, 1999.

[35] K. Katija. Morphology alters fluid transport and the ability of organisms to mix oceanic waters. *Integr Comp Biol*, 55:698–705.

[36] K. Katija. Biogenic inputs to ocean mixing. *J Exp Biol*, 215:1040–1049, 2012.

[37] K. Katija and J. O. Dabiri. A viscosity-enhanced mechanism for biogenic ocean mixing. *Nature*, 460(7255):624–626, 2009.

[38] P. Klein and G. Lapeyre. The oceanic vertical pump induced by mesoscale and submesoscale turbulence. *Annu Rev Mar Sci*, 1(1):351–375, 2009.

[39] D. L. Koch and G. Subramanian. Collective hydrodynamics of swimming microorganisms: Living fluids. *Ann. Rev. Fluid Mech.*, 43:637–659, 2011.

[40] P. K. Kundu and I. M. Cohen. *Fluid Mechanics*. Academic Press, 2008.

[41] E. Kunze. Fluid mixing by swimming organisms in the low-Reynolds-number limit. *J Mar Res*, 69:591–601, 2011.

[42] E. Kunze, J. F. Dower, I. Beveridge, R. Dewey, and K. P. Bartlett. Observations of biologically generated turbulence in a coastal inlet. *Science*, 313(5794):1768–1770, 2006.

[43] E. Kunze, J. F. Dower, R. Dewey, E. A. D'Asaro, and A. W. Visser. Mixing it up with krill (with response). *Science*, 318:1239, 2007.

[44] J. H. LaCasce. Statistics from Lagrangian observations. *Prog Oceanogr*, 77:1–29, 2008.

[45] C. Lalli and T. R. Parsons. *Biological Oceanography: An Introduction*. Elsevier, 1997.

[46] J.-P. Laval, B. Dubrulle, and S. Nazarenko. Nonlocality and intermittency in three-dimensional turbulence. *Phys Fluids*, 13:1070–6631, 2001.

[47] P. Lavens and P. Sorgeloos. Manual on the production and use of live food for aquaculture. Technical Report 361, Food and Agriculture Organization of the United Nations, 1996.

[48] A. G. W. Lawrie and S. B. Dalziel. Rayleigh-Taylor mixing in an otherwise stable stratification. *J Fluid Mech*, 688:507–527, 2011.

[49] J. R. Ledwell, A. J. Watson, and C. S. Law. Evidence for slow mixing across the pycnocline from an open-ocean tracer-release experiment. *Nature*, 364:701–703, 1993.

[50] A. M. Leshansky and L. M. Pismen. Do small swimmers mix the ocean? *Phys Rev E*, 82:1–5, 2010.

[51] M. Lesieur. *Turbulence in Fluids*. Kluwer Academic Publishers, 1990.

[52] A. R. Longhurst and W. G. Harrison. Vertical nitrogen flux from the oceanic photic zone by diel migrant zooplankton and nekton. *Deep-Sea Res*, 35:881–889, 1988.

[53] J. L. Lumley and A. M. Yaglom. *A Century of Turbulence*. Kluwer Academic Publishers, 2001.

[54] A. Mahadevan. Eddy effects on biogeochemistry. *Nature*, 506:168–169, 2014.

[55] P. Manneville. Intermittency, self-similarity and $1/f$ spectrum in dissipative dynamical systems. *J Physique*, 41:1235–1243, 1980.

[56] N. Mazellier and J. C. Vassilicos. Turbulence without Richardson-Kolmogorov cascade. *Phys Fluids*, 22:075101, 2010.

[57] W. N. McFarland. Light in the sea—correlations with behaviors of fishes and invertebrates. *Amer Zool*, 26:389–401, 1986.

[58] C. M. Moore, M. M. Mills, K. R. Arrigo, I. Berman-Frank, L. Bopp, P. W. Boyd, E. D. Galbraith, R. J. Geider, C. Guieu, S. L. Jaccard, T. D. Jickells, J. La Roche, T. M. Lenton, N. M. Mahowald, E. Marañón, I. Marinov, J. K. Moore, T. Nakatsuka, A. Oschlies, M. A. Saito, T. F. Thingstad, A. Tsuda,

and O. Ulloa. Processes and patterns of oceanic nutrient limitation. *Nature Geo*, 6:701–710, 2013.

[59] W. Munk and C. Wunsch. Abyssal recipes II: Energetics of tidal and wind mixing. *Deep Sea Res I*, 45:1977–2010, 1998.

[60] W. H. Munk. Abyssal recipes. *Deep Sea Res*, 13:707–730, 1966.

[61] D. W. Murphy, D. R. Webster, and S. Kawaguchi. Metachronal swimming in Antarctic Krill: gait kinematics and system design. *Mar Biol*, 158:2541–2554, 2011.

[62] J. C. Nawroth, , and J. O. Dabiri. Induced drift by a self-propelled swimmer at intermediate Reynolds numbers. *Phys of Fluids*, 26:091108, 2014.

[63] J. C. Nawroth, H. Lee, A. W. Feinberg, C. M. Ripplinger, M. L. McCain, A. Grosberg, J. O. Dabiri, and K. K. Parker. A tissue-engineered jellyfish with biomimetic propulsion. *Nature Biotechnology*, 30:792–797, 2012.

[64] S. Nazarenko and J.-P. Laval. Non-local two-dimensional turbulence and Batchelor's regime for passive scalars. *J Fluid Mech*, 408:301–321, 2000.

[65] M. Nikurashin and R. Ferrari. Global energy conversion from geostrophic flow into internal lee waves in the deep ocean. *Geophys Res Lett*, 38:L08610, 2011.

[66] C. Noss and A. Lorke. Zooplankton induced currents and fluxes in stratified waters. *Water Qual Res J Can*, 47:276–286, 2012.

[67] C. Noss and A. Lorke. Direct observation of biomixing by vertically migrating zooplankton. *Limnol Oceanogr*, 59:724–732, 2014.

[68] N. S. Oakey. Determination of the rate of dissipation of turbulent energy from simultaneous temperature and velocity shear microstructure measurements. *J Phys Oceanogr*, 12:256–271, 1982.

[69] T. R. Osborn. Estimates of the local rate of vertical diffusion from dissipation measurements. *J Phys Oceanogr*, 10:83–89, 1980.

[70] C. M. Owens. Behavioral assay to determine photosensitivity of early-stage nauplii of the brine shrimp *Artemia franciscana*. Master's thesis, Wagner College, 2002.

[71] A. E. Perry, S. Henbest, and M. S. Chong. A theoretical and experimental study of wall turbulence. *J Fluid Mech*, 165:163–199, 1986.

[72] R. T. Pierrehumbert. Spectra of local and non-local two-dimensional turbulence. *Chaos*, 4:1111–1116, 1994.

[73] J. Piquet. *Turbulent Flows: Models and Physics*. Springer, 1999.

[74] K. L. Polzin, J. M. Toole, J. R. Ledwell, and R. W. Schmitt. Spatial variability of turbulent mixing in the abyssal ocean. *Science*, 276:93–96, 1997.

[75] Y. Pomeau and P. Manneville. Intermittent transition to turbulence in dissipative dynamical systems. *Commun Math Phys*, 23:189–197, 1980.

[76] S. B. Pope. *Turbulent Flows*. Cambridge University Press, 2000.

[77] D. O. Pushkin, H. Shum, and J. M. Yeomans. Fluid transport by individual microswimmers. *J Fluid Mech*, 726:5–25, 2013.

[78] J. Ringelberg. Changes in light intensity and Diel Vertical Migration: A comparison of marine and freshwater environments. *J Mar Biol Ass UK*, 75:15–25, 1995.

[79] J. Ringelberg. *Diel Vertical Migration of Zooplankton in Lakes and Oceans*. Springer, 2010.

[80] S. Rousseau, E. Kunze, R. Dewey, K. Bartlett, and J. Dower. On turbulence production by swimming marine organisms in the open ocean and coastal waters. *J Phys Oceanogr*, 40(9):2107–2121, 2010.

[81] V. A. Sandborn. Measurements of intermittency of turbulent motion in a boundary layer. *J Fluid Mech*, 4:221–240, 1958.

[82] R. K. Scott. Local and nonlocal advection of a passive scalar. *Phys Fluids*, 18:116601, 2006.

[83] R. C. Smith and K. S. Baker. Optical properties of the clearest natural waters (200-800 nm). *Applied Optics*, 20:177–184, 1981.

[84] W. D. Smyth and K. B. Winters. Turbulence and mixing in Holmboe waves. *J Phys Oceanogr*, 33:694–711, 2003.

[85] K. R. Sreenivasan and R. Ramshankar. Transition intermittency in open flows, and intermittency routes to chaos. *Physica 23D*, 23:246–258, 1986.

[86] G. Subramanian. Viscosity-enhanced bio-mixing of the oceans. *Curr Sci*, 98:1103–1108, 2010.

[87] R. Tailleux. On the energetics of stratified turbulent mixing, irreversible thermodynamics, Boussinesq models and the ocean heat engine controversy. *J Fluid Mech*, 638:339–382, 2009.

[88] T. Tanaka and J. K. Eaton. A correction method for measuring turbulence kinetic energy dissipation rate by PIV. *Exp Fluids*, 42:893–902, 2007.

[89] C. M. Tchen. On the spectrum of energy in turbulent shear flow. *J Res Nat Bur Stand*, 50:51–62, 1953.

[90] H. Tennekes and J. L. Lumley. *A First Course in Turbulence*. The MIT Press, 1972.

[91] J.L. Thiffeault and S. Childress. Stirring by swimming bodies. *Phys Lett A*, 374:3487–3490, 2010.

[92] J. M. T. Thompson and H. B. Stewart. *Nonlinear Dynamics and Chaos*. Wiley, 2002.

[93] S. A. Thorpe. *The Turbulent Ocean*. Cambridge University Press, 2005.

[94] D. J. Tritton. *Physical Fluid Dynamics*. Oxford Science Publications, 1988.

[95] A. Tsinober. *An Informal Introduction to Turbulence*. Kluwer Academic Publishers, 2001.

[96] A. Tsinober. *An Informal Conceptual Introduction to Turbulence*. Springer, 2009.

[97] U Utah. The brine shrimp life cycle, 2015.

[98] G. K. Vallis. *Atmospheric and Oceanic Fluid Dynamics*. Cambridge University Press, 2006.

[99] H. van Haren. Monthly periodicity in acoustic reflections and vertical motions in the deep ocean. *Geophys Res Letters*, 34:L12603, 2007.

[100] A. W. Visser. Biomixing of the oceans? *Science*, 316(5826):838–839, 2007.

[101] G. L. Wagner, W. R. Young, and E. Lauga. Mixing by microorganisms in stratified fluids. *J Mar Res*, 72:47–72, 2014.

[102] Z. Warhaft. Passive scalars in turbulent flows. *Annu Rev Fluid Mech*, 32:203–240, 2000.

[103] B. White and H. M. Nepf. Scalar transport in random cylinder arrays at moderate Reynolds number. *J Fluid Mech*, 487:43–79, 2003.

[104] L. N. Wickramarathna, C. Noss, and A. Lorke. Hydrodynamic trails produced by *Daphnia*: Size and energetics. *PloS one*, 9:e92383, 2014.

[105] P. Wiebe, L. Madin, L. Haury, G. Harbison, and L. Philbin. Does the marine biosphere mix the ocean? *Mar Biol*, 53:249–255, 1979.

[106] C. Wunsch and R. Ferrari. Vertical mixing, energy, and the general circulation of the oceans. *Annu Rev Fluid Mech*, 36:291–314, 2004.

[107] M. S. Davies Wykes and S. B. Dalziel. Efficient mixing in stratified flows: experimental study of a Rayleigh-Taylor unstable interface within an otherwise stable stratification. *J Fluid Mech*, 756:1027–1057, 2014.

[108] J. Yen, J. Brown, and D. R. Webster. Analysis of the flow field of the krill, *Euphausia Pacifica*. *Mar Freshwater Behav Physiol*, 36(4):307–319, 2003.